SEARCH FOR HIGGS BOSON PAIR PRODUCTION IN THE MULTIPLE LEPTON FINAL STATE USING PROTON-PROTON COLLISION DATA AT $\sqrt{S} = 13$ TEV FROM THE ATLAS DETECTOR

Approved by:

Dr. Allison Deiana
Assistant Professor

Dr. Fredrick Olness
Professor

Dr. Jingbo Ye
Professor

Dr. Suyog Shrestha
Assistant Professor, Washington College

# SEARCH FOR HIGGS BOSON PAIR PRODUCTION IN THE MULTIPLE LEPTON FINAL STATE USING PROTON-PROTON COLLISION DATA AT $\sqrt{S} = 13$ TEV FROM THE ATLAS DETECTOR

A Dissertation Presented to the Graduate Faculty of the

Dedman College

Southern Methodist University

in

Partial Fulfillment of the Requirements

for the degree of

Doctor of Philosophy

with a

Major in Physics

by

Santosh Parajuli

B.S., Physics, Tribhuvan University, Nepal
M.S., Physics, University of Texas at Dallas

July 31, 2023

## Acknowledgments

I want to express my sincere gratitude to Dr. Allison Deiana, my advisor, for her exceptional guidance, expertise, and support throughout my entire PhD thesis. Dr. Deiana's extensive knowledge, dedication, and valuable feedback have played a crucial role in shaping and refining this research. I am genuinely thankful for her invaluable mentorship and the opportunity to learn under her guidance.

Additionally, I extend my heartfelt appreciation to Dr. Rohin Narayan, a postdoctoral researcher in our research group, for his invaluable contributions to this thesis. Dr. Narayan's expertise, enthusiasm, and willingness to assist have significantly enhanced the quality of this research. His insightful discussions, technical guidance, and collaborative approach have been indispensable assets throughout this project.

I deeply appreciate the invaluable input, thoughtful suggestions, and meticulous review provided by my thesis committee members: Dr. Fredrick Olness, Dr. Jingbo Ye, and Dr. Suyog Shrestha. Their profound expertise and scholarly contributions have greatly enriched the depth and quality of this study.

Furthermore, I would like to acknowledge the ATLAS Collaboration for generously granting access to the data used in this analysis and for their diligent efforts in maintaining and operating the ATLAS detector at the LHC. The collective endeavors of this collaboration have been crucial in making this research endeavor possible.

I am truly grateful to my parents, whose unwavering love, support, and countless sacrifices have enabled me to pursue my education. Their consistent encouragement, guidance, and unwavering belief in my abilities have been fundamental in shaping my academic journey.

I would like to give special thanks to my dear wife, Supriya Dhakal, for her constant love, understanding, and support throughout my academic pursuit. Her patience and encouragement have consistently been a driving force for me.

Lastly, I am profoundly grateful to my family and friends for their support, encouragement, and deep understanding throughout my academic journey. Their enduring love and confidence in my abilities have been an everlasting source of motivation.

Parajuli, Santosh

B.S., Physics, Tribhuvan University, Nepal
M.S., Physics, University of Texas at Dallas

Search for Higgs Boson Pair Production in the Multiple Lepton Final State Using Proton-Proton Collision Data at $\sqrt{s} = 13$ TeV from the ATLAS Detector

Advisor: Dr. Allison Deiana
Doctor of Philosophy degree conferred July 31, 2023
Dissertation completed June 23, 2023

In this thesis, a search is presented for the production of Higgs boson pairs in final states containing three light leptons ($e/\mu$). The analysis utilizes data collected by the ATLAS detector at the Large Hadron Collider from proton-proton ($pp$) collisions at a center-of-mass energy of $\sqrt{s} = 13$ TeV, corresponding to an integrated luminosity of 140 $fb^{-1}$. The investigation aims to identify any significant deviations from the expected background levels defined by the Standard Model. The Higgs boson, as the cornerstone of the electroweak symmetry breaking mechanism, plays a crucial role in our understanding of particle physics. Studying the production of Higgs boson pairs is of particular interest as it provides insight into the self-interactions of this fundamental particle.

After an extensive study, no significant excess above the anticipated background expectations was observed in the analyzed dataset. However, upper limits on the signal strength of the Higgs boson pair production process was established at a confidence level of 95%. The observed (expected) limit on the signal strength was found to be 20 (28) times the Standard Model cross section.

TABLE OF CONTENTS

# LIST OF FIGURES

# LIST OF TABLES

To My Parents

# Chapter 1

## Introduction

People have been asking fundamental questions about how the world was created and how it operates for a long time. What is the universe made of? How did the universe begin? What is the nature of dark matter and dark energy? What is the ultimate fate of the universe? These are just a few examples of the fundamental questions about the universe that scientists and philosophers are grappling with. Ancient Indian and Greek philosophers were among the first to attempt to answer these questions, and they contributed greatly on establishing the fundamental principles that are still in use today, such as the conservation of matter and the atomic theory. The exploration of the basic elements and structure of matter has captured the attention of mankind for millennia. In the 6th century BCE, ancient Indian thinkers suggested that the things we encounter in our everyday existence consist of minuscule particles that are invisible to the naked eye. The notion of these unbreakable units of the natural world was similarly put forth by Greek scholars like Democritus and Leucippus, who called them 'atoms'.

However, it wasn't until the 19th century that John Dalton created a scientific model of atomic theory [1], which marked the beginning of our understanding of the nature of atoms and their substructure. This paved the way for significant progress in the field over the next several centuries, with scientists like Thomson and Rutherford making fundamental advancements. These researchers established a solid foundation for future investigations into the topic.

In the latter half of the 20th century, significant advancements in particle theory, including the proposal of the quark model by Gell-Mann and Zweig in 1964 [2], and the formulation

of the electroweak theory by Glashow, Weinberg, and Salam in the 1970s, laid the groundwork for the development of the Standard Model (SM) of particle physics. The quark model helped organize particles into a coherent framework, while the electroweak theory presented a model for vector bosons and made predictions about the masses of the $W^{\pm}$ and Z bosons. These predictions were later confirmed at CERN in 1983 [3].

The Standard Model (SM) of particle physics is a comprehensive and widely accepted framework that is considered the best model for explaining the behavior of fundamental particles and their interactions. It has accurately predicted the existence of particles such as the top quark [4] and Higgs boson [5], which were later confirmed through experiments. The SM's precise and reliable predictions have made it a vital foundation of modern physics research. However, despite its achievements, the SM is an incomplete theory, and there are still many unanswered questions in particle physics.

### 1.1. The Standard Model

The goal of physics is to provide a complete explanation and prediction of natural phenomena using a minimal set of fundamental laws and theories. At the microscopic level, the behavior of all matter is explained by three fundamental interactions; electromagnetism, weak, and strong forces, encompassing molecular, atomic, nuclear, and subnuclear physics. While at the macroscopic level, the fourth force, gravitational interaction, plays a significant role but is not considered at the microscopic level. A fundamental particle is a type of particle that is not made up of any other particles and does not have any internal structure. The fundamental particles in the Standard Model is summarized as illustrated in Figure 1.1.

The fundamental particles can be divided into two categories, **fermions** and **bosons**. Fermions make up the matter that we see around us, while bosons are responsible for mediating the fundamental forces that govern the behavior of matter. Fermions have half-integer spin and can be further subdivided into **quarks** and **leptons**. Quarks carry a fractional

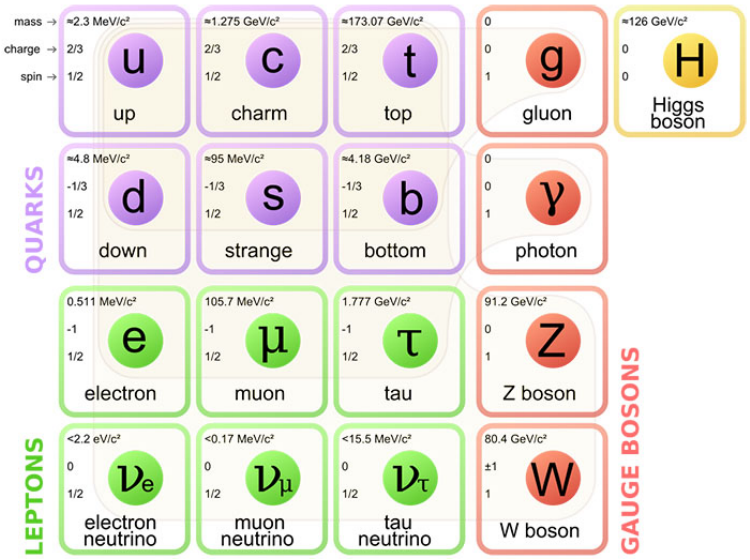


Figure 1.1: The particle content of the Standard Model of particle physics.

electric charge and a color charge, which allows them to interact through the strong, electromagnetic, and weak forces. Up-type quarks have a charge of $+2/3$, and down-type quarks have a charge of $-1/3$. Leptons, on the other hand, have an integer electric charge and no color charge, and therefore only interact via the electromagnetic and weak forces, not the strong force. Charged leptons, such as electrons, muons, and tau leptons, have a charge of $-1$, and each of them is paired with a neutrino of the same flavor. Neutrinos, as their name suggests, are electrically neutral.

There exist three distinct generations of fermions in which each successive generation is more massive than the previous one as shown in Figure 1.1. The first generation of fermions comprises the u, d, e, and $\nu_e$ particles. The second generation consists of the c, s, $\mu$, and $\nu_\mu$ particles. The third and final group is composed of the t, b, $\tau$, and $\nu_\tau$ particles. Despite significant differences in their masses, all three generations of fermions share comparable properties. As heavier particles decay into lighter ones, all of the matter that we observe consists of the first generation of fermions. Protons and neutrons are constructed of up and down quarks, while atoms are composed of electrons, protons, and neutrons.

Bosons have a spin value that is an integer. There are different spin-1 bosons that are associated with different forces. The photon is responsible for the electromagnetic force, the W & Z bosons are responsible for the weak force, and the gluon is responsible for the strong force. The electroweak force, which is a combination of the electromagnetic and weak forces, is explained by electroweak symmetry breaking. This process involves the Higgs boson, which is the only known spin-0 particle in the Standard Model. The Higgs boson's mass is not predetermined, but it is a free parameter in the SM. The most recent combined results from ATLAS and CMS measure the mass of the Higgs boson to be $125.09 \pm 0.24$ GeV [5, 6]. In addition to the fundamental particles, there are corresponding antiparticles for each particle in the Standard Model. Antiparticles have the same mass but opposite electric charge and other quantum numbers compared to their corresponding particles.

### 1.2. Symmetries of the Standard Model

The Standard Model (SM) is a gauge theory that is based on the Yang-Mills theory [7]. Gauge theories are field theories where the Lagrangian remains unchanged under local transformations, also known as gauge invariance. The symmetry group of the theory represents these transformations. In addition, Yang-Mills theories are non-abelian gauge theories, meaning their symmetry group is non-commutative. According to Noether's theorem [8], every natural symmetry corresponds to a conservation law. In the context of the Standard Model, this symmetry is intimately connected to the conservation of fundamental quantities such as electric charge, color charge, etc. The way particles within the Standard Model interact can be described by a quantum field theory with the following gauge symmetry:

$$SU_C(3) \times SU_L(2) \times U_Y(1) \tag{1.1}$$

The $SU_C(3)$ subgroup is related to the strong interaction between particles that have different colors, and it is characterized by 8 $(n^2-1)$ generators represented by the Gell-Mann matrices.

The $SU_L(2)$ and $U_Y(1)$ subgroups are associated with the electroweak interaction and they have four generators that give rise to the $W^{\pm}$, $Z$, and $\gamma$ bosons. The $SU_L(2)$ symmetry only couples with left-handed particles. $U(1)$ symmetry conserves hypercharge, which is determined by charge and the third component of isospin. The Standard Model Lagrangian can compactly be written as:

$$L = -\frac{1}{4}F^a_{\mu\nu}F^{\mu\nu}_a + i\bar{\psi}\gamma^\mu D_\mu\psi + (D_\mu\phi)^\dagger(D^\mu\phi) - V(\phi) + (y_{ij}\bar{\psi}_i\bar{\psi}_j + \text{h.c.}) \tag{1.2}$$

where $F^a_{\mu\nu}$ is the field strength tensor for the $A_\mu$ gauge fields, $F^a_{\mu\nu} = \partial_\mu A^a_\nu - \partial_\nu A^a_\mu + g f^{abc} A^b_\mu A^c_\nu$, $\psi$ represents the fermion fields, $\phi$ is the Higgs field, $V(\phi)$ is the Higgs potential. $D_\mu$ is a gauge covariant derivative. There are no explicit mass terms in the SM Lagrangian. This is a problem as we know that fermions have mass, and massive bosons such as the W and Z exist. To solve this problem, the Brout-Englert-Higgs [9] mechanism was proposed as a solution. This mechanism introduces a self-interacting complex scalar field i.e the Higgs field, which spontaneously breaks the $SU_L(2) \times U_Y(1)$ symmetry.

### 1.3. Electroweak Symmetry Breaking

Consider the U(1) gauge theory with a single gauge field (the photon). The Lagrangian is,

$$L = -\frac{1}{4}F_{\mu\nu}F^{\mu\nu} \tag{1.3}$$

Where $F_{\mu\nu} = \partial_\mu A_\nu - \partial_\nu A_\mu$ is the electromagnetic field tensor. Adding a massive term to this equation would violate the established local gauge invariance, as the U(1) invariance requires the photon to be massless. Extending this by adding a complex scalar doublet,

$$\phi = \begin{pmatrix} \phi^+ \\ \\ \phi^0 \end{pmatrix} = \frac{1}{\sqrt{2}} \begin{pmatrix} \phi_1 + i\phi_2 \\ \\ \phi_3 + i\phi_4 \end{pmatrix} \tag{1.4}$$

Where $\phi^+$ is a positively charged field and $\phi^0$ is a neutral field. Then the Lagrangian and gauge-invariant potential become:

$$L = -\frac{1}{4}F_{\mu\nu}F^{\mu\nu} + (D_\mu\phi)^\dagger (D^\mu\phi) - V(\phi) \tag{1.5}$$

the first term is the kinetic term, where $D_\mu$ is the covariant derivative $D_\mu = \partial_\mu + igT \cdot W_\mu + ig'\frac{Y}{2}B_\mu$. Where g is the SU(2) gauge coupling, g' is the U(1) gauge coupling, and Y is the U(1) hypercharge. $V(\phi)$ is the Higgs potential,

$$V(\phi) = \mu^2\phi^\dagger\phi + \lambda(\phi^\dagger\phi)^2 \tag{1.6}$$

The first term in the equation 1.6 is related to the mass of the field, while the second term describes the self-interaction of the scalar field in a quadratic manner. To achieve a potential with finite minima, the value of the parameter $\lambda$ must be positive, while the value of $\mu$ can be chosen freely. If $\mu^2 > 0$, the potential has a sole minimum value at zero, the vacuum expectation value of the Higgs field would be zero, and the symmetry is maintained. If $\mu^2 < 0$, the potential has an infinite set of minima $v$ given by:

$$\phi_0 = \langle\phi^+\phi\rangle = \frac{v^2}{2} = -\frac{\mu^2}{2\lambda} \tag{1.7}$$

A potential is shown in Figure 1.2. By convention, $v$ is selected to be real, making $\phi_1 = \phi_2 = \phi_3 = 0$, and $\phi_4 = v$. In making this selection, electroweak symmetry is spontaneously broken. Unitarity gauge is given by expanding about this minima, making this field:

$$\phi(x) = \frac{1}{\sqrt{2}}\begin{pmatrix} 0 \\ \\ v + h(x) \end{pmatrix} \tag{1.8}$$

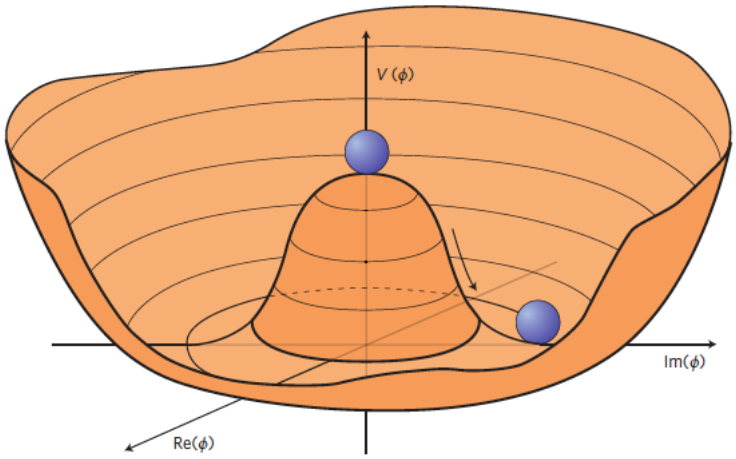


Figure 1.2: Shape of the Higgs potential for $\mu^2 < 0$.

Where $h(x)$ represents the Higgs field linked to a new massive particle: the Higgs boson, and $v$ is known as the vacuum expectation value, where $v = \sqrt{\frac{-\mu^2}{\lambda}} = \frac{2m_W}{g} = 246$ GeV. As we know, the portion of the SM Lagrangian associated with the Higgs field is:

$$L = (D_\mu \phi)^\dagger (D^\mu \phi) - V(\phi) \tag{1.9}$$

We can substitute Equation 1.8 here, we get:

$$L = \frac{1}{2}(\partial_\mu h)(\partial^\mu h) + \frac{1}{4}g^2 W_\mu W^\mu (v+h)^2 + \frac{1}{4}(g^2+g'^2) Z_\mu Z^\mu (v+h)^2 + \frac{\mu^2}{2}(v+h)^2 - \frac{\lambda}{4}(v+h)^4 \tag{1.10}$$

In this expansion, the $W$, $Z$, and Higgs bosons have subsequently acquired masses corresponding to the quadratic terms associated with their respective gauge fields:

$$m_W^2 = \frac{g^2 v^2}{4}, m_Z^2 = \frac{(g^2+g'^2)v^2}{4}, m_H^2 = 2\mu^2 \tag{1.11}$$

## 1.4. Higgs Self-Coupling

From Equation 1.6 we can write the Higgs potential as

$$V(\phi) = \mu^2\phi^2 + \lambda\phi^4 \tag{1.12}$$

Which is symmetric in $\phi$. In unitarity gauge, the Higgs potential takes the form:

$$V(h) = \lambda v^2 h^2 + \lambda v h^3 + \frac{\lambda}{4}h^4 \tag{1.13}$$

The first term corresponds to the mass term of the Higgs field and gives the Higgs boson mass $m_H = \sqrt{2\lambda\nu^2}$. The second term gives rise to the trilinear coupling, while the third indicates the Higgs quartic coupling. In the SM, the Higgs self-coupling at the minimum of the Higgs potential is expected to be:

$$\lambda_{SM} = \frac{m_h^2}{2v^2} = 0.129 \tag{1.14}$$

The ratio of the measured Higgs self-coupling to its expected Standard Model value can be defined as:

$$k_\lambda = \frac{\lambda}{\lambda_{SM}} \tag{1.15}$$

Where $\lambda$ is the measured Higgs self-coupling in this case. For SM, $k_\lambda$ =1. The production of HH and single Higgs particles can be used to measure variations in $k_\lambda$. However, measuring $k_\lambda$ is challenging due to the low production rate of HH particles and the small effects of $k_\lambda$ on single Higgs processes. Measuring $k_\lambda$ is important to test our understanding of electroweak symmetry breaking and to probe the shape of the Higgs potential in a new way. Measuring $k_\lambda$ will also help us understand the Higgs interactions with itself. Deviations in $k_\lambda$ could indicate new physics beyond the Standard Model. Due to its extremely low rate of occurrence, the HHH process cannot be effectively measured at the Large Hadron Collider (LHC).

## 1.5. Higgs Boson at LHC

The LHC mainly produces Higgs through several processes such as gluon-gluon fusion(ggF), vector boson fusion(VBF), Higgs-strahlung with W or Z bosons (VH), and the associated production with a pair of top quarks known as $t\bar{t}H$. The leading order Feynman diagrams for each of these processes is shown in Figure 1.3.

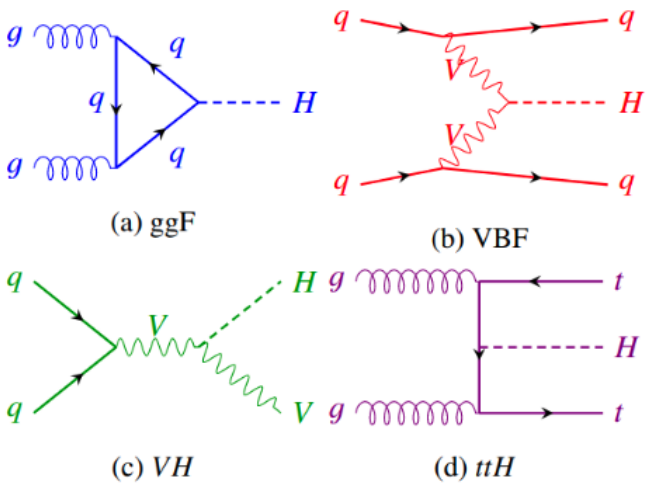


Figure 1.3: Leading order Feynman diagrams for the dominant production modes of Higgs boson.

The primary method of producing Higgs boson at the LHC is through ggF, which accounts for 87% of all Higgs boson events at the 13 TeV [10] center of mass energy for the 2015-2018 data-taking period (Run 2). This mode involves the production of Higgs boson by two gluons in the initial state through a heavy quark loop. The second most prevalent mode of Higgs boson production at the LHC is through VBF, accounting for 6.8% of all Higgs boson events. During VBF production, the incoming quarks emit vector bosons that interact to generate the Higgs boson. The quarks that radiate the vector bosons are present in the final state, and they produce a unique signature of being predominantly forward in direction. The SM Higgs boson production cross-section for the various production modes depends on the Higgs boson mass and the centre-of-mass energy, as shown in Figure 1.4.

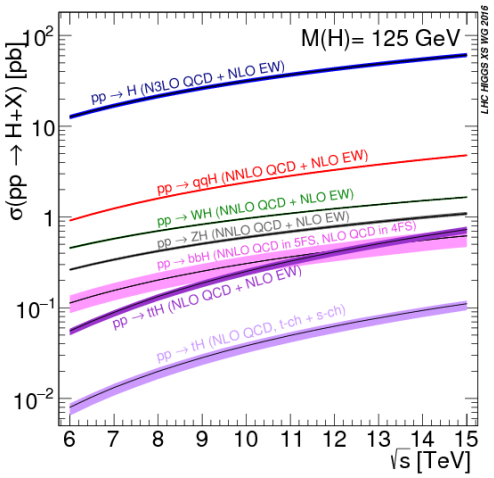


Figure 1.4: The cross-section(pb) of various Higgs boson production modes for a SM Higgs boson with $m_H = 125$ GeV as a function of the center-of-mass energy [11].

The Higgs boson is an unstable particle. Because the Higgs boson has a brief lifespan, its decay products are studied. The Higgs interacts with all massive particles and can decay into any such particles as long as conservation laws are observed. It can also decay into massless particles through virtual loops, but these branching ratios are relatively minor as shown in Figure 1.5.

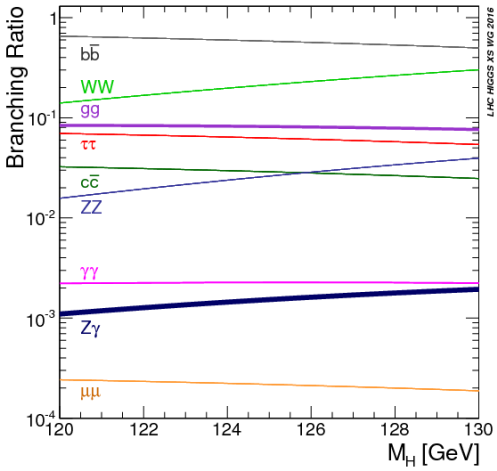


Figure 1.5: Higgs boson branching ratio of the possible Higgs boson decay channels as a function of the Higgs boson mass [11].

### 1.6. Single Higgs Sensitivity to $k_\lambda$

Even though single Higgs boson production do not provide significant information about the Higgs self-coupling at the leading order, the self-coupling does play a role in the electroweak corrections at the next to leading order. Figure 1.6 displays the Feynman diagrams depicting the contribution of the self-coupling to the Higgs self-energy and other corrections. Modifying the value of $k_\lambda$ can affect the Higgs cross-sections, branching ratios, and overall kinematics, as shown in Figure 1.7 . These effects are relatively minor when compared to the effects observed in HH production, but it is possible to limit $k_\lambda$ by comparing precise measurements of single Higgs measurements to predictions that incorporate these corrections [12].

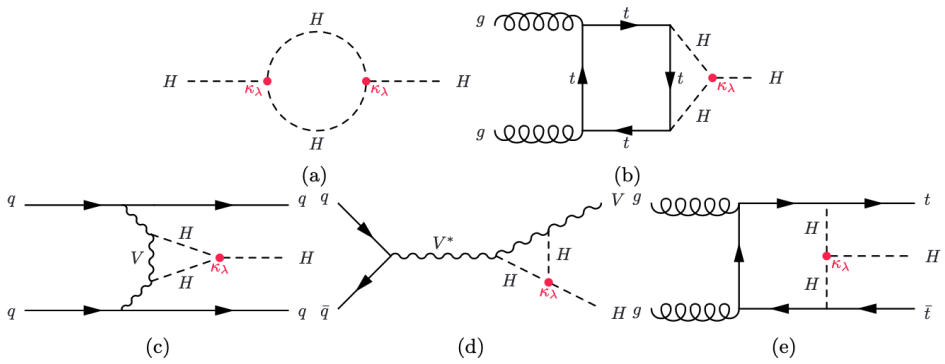


Figure 1.6: Examples of one-loop dependent single Higgs diagrams for the Higgs boson self-energy, and for single Higgs production in different modes [13].

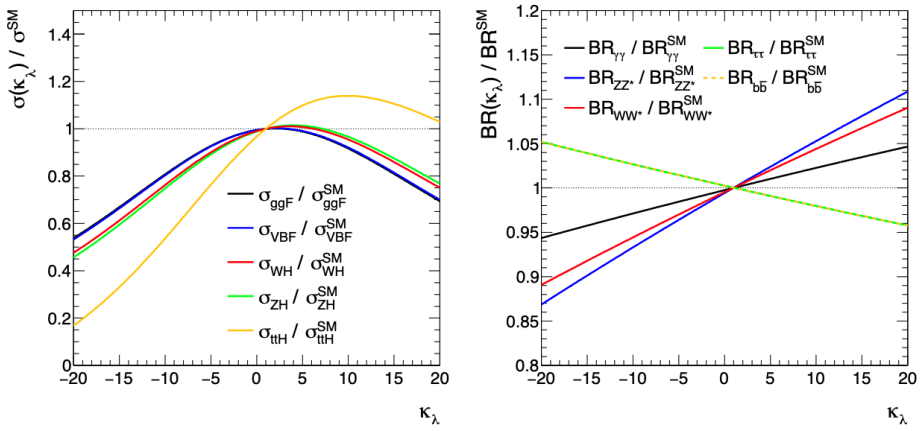


(a) (b)

Figure 1.7: Changes to the single Higgs (a) cross-sections and (b) branching ratios as a function of $k_\lambda$ [13].

## 1.7. Di-Higgs Boson Production

Studying processes involving two Higgs bosons at the LHC is a primary way to constrain the Higgs self-coupling. In Standard Model, there are various ways to produce pairs of Higgs bosons. The most dominant mode is ggF, which accounts for more than 90% of di-Higgs (HH) production. The second most significant mode is VBF, which is responsible for just over 5% of HH production. The remaining modes, VHH, ttHH, and tjHH, together make up less than 5% of HH production and their cross-section is too small to expect to be measured at the LHC.

The production rates of Higgs boson pairs depend on the strength of the Higgs self-coupling [14]. Figure 1.8 illustrates the predicted cross-sections as a function of the Higgs self-coupling parameter. In all production modes, the cross-section for Higgs boson pairs changes as the self-coupling parameter deviates significantly from the standard model value.

In 13 TeV pp collisions, where the Higgs boson mass is $m_H = 125.09$ GeV, the cross-section for ggF production of Higgs boson pairs is $\sigma_{HH}(ggF) =$

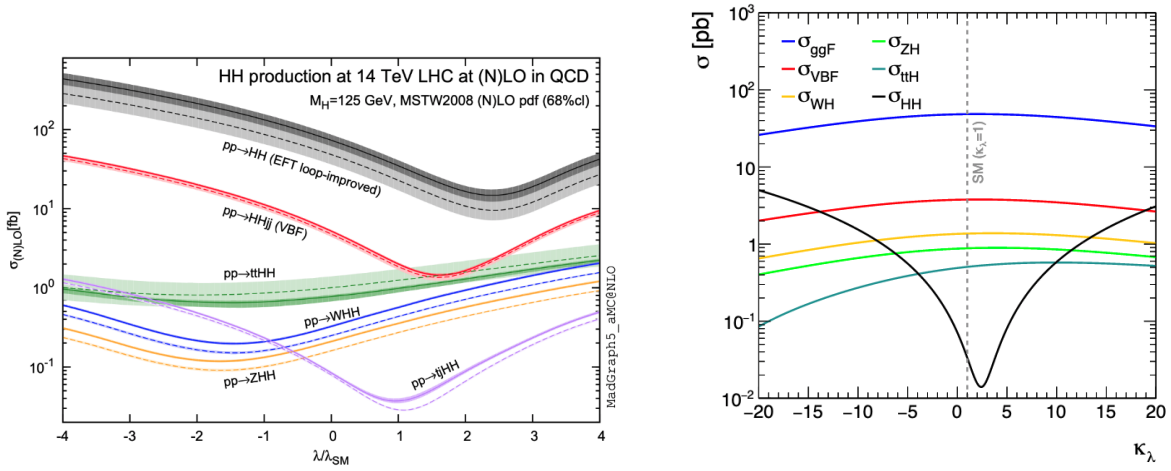


Figure 1.8: Predicted HH cross-sections(fb) as a function of $k_\lambda$ [14] (left). Predicted HH cross-sections(pb) as a function of $k_\lambda$ relative to single Higgs processes [13] (right).

$31.02^{+2.2\%}_{-5.0\%}(\text{Scale})^{+4\%}_{-18\%}(\text{m}_{top}) \pm 3.0\%(\alpha_s + \text{PDF})$ fb [15] in SM. This cross-section has been calculated with next-to-next-to-leading-order (NNLO) accuracy in the finite top-quark mass approximation (FTapprox).

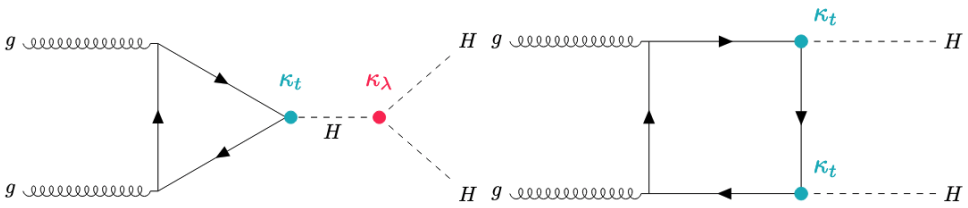


(a) Triangle diagram (b) Box diagram

Figure 1.9: Examples of tree level Feynman diagrams for non-resonant ggF HH production.

The ggF production of HH at leading order can be described using the box and triangle Feynman diagrams shown in Figure 1.9. The triple Higgs vertex present in the triangle diagram makes it sensitive to the Higgs self-coupling ($k_\lambda$), while the box diagram lacks this vertex and is hence insensitive to $k_\lambda$ at leading order. Apart from $k_\lambda$, both the triangle and box diagrams respond to the top-quark Yukawa coupling ($k_t$). The value of $k_t$ is maintained at its SM value of 1.

At leading order, the two ggF production of HH diagrams interfere with each other destructively, resulting in a small cross-section [16]. This destructive interference makes the cross-section highly sensitive to the Higgs self-coupling ($k_\lambda$). Figure 1.8 illustrates the cross-sections of HH and single Higgs as a function of $k_\lambda$. While the HH production cross-section is negligible near the SM value of $k_\lambda$, it rapidly increases for larger absolute values of $k_\lambda$.

The VBF mode is the second most important way in which HH is produced. This mode involves the scattering of two quarks through the exchange of a virtual vector boson, $W^\pm$ or Z, from which a HH system is created. This process is described by three Feynman diagrams at the tree level, as shown in Figure 1.10. At a center-of-mass energy of 13 TeV, the cross-section for VBF production is $1.73^{+0.03\%}_{-0.04\%} \pm 2.1\%$ fb [15] in SM. The VBF production mode offers additional sensitivity to the Higgs trilinear coupling. In addition to being sensitive to $k_\lambda$, VBF di-Higgs production is also sensitive to $k_{2V}$ and $k_V$.

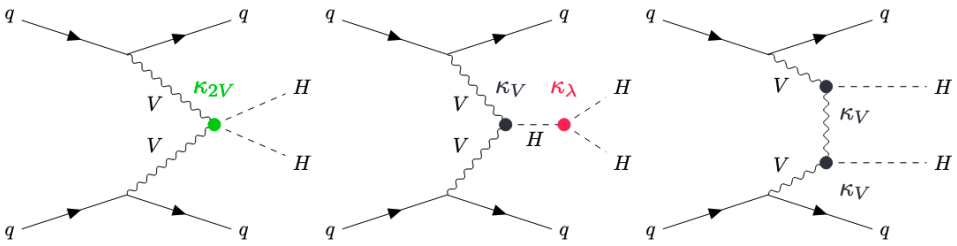


Figure 1.10: Examples of tree level Feynman diagrams for VBF HH production.

## 1.8. Di-Higgs Boson Decays

When searching for di-Higgs, it is important to take into account the characteristics of both Higgs decays. Figure 1.11 displays the branching ratios for different combinations of HH decays. The $\bar{b}b\bar{b}b$ decay channel has the highest possible branching ratio at 33.9%, but it poses significant challenges related to triggering and the presence of a large QCD background.

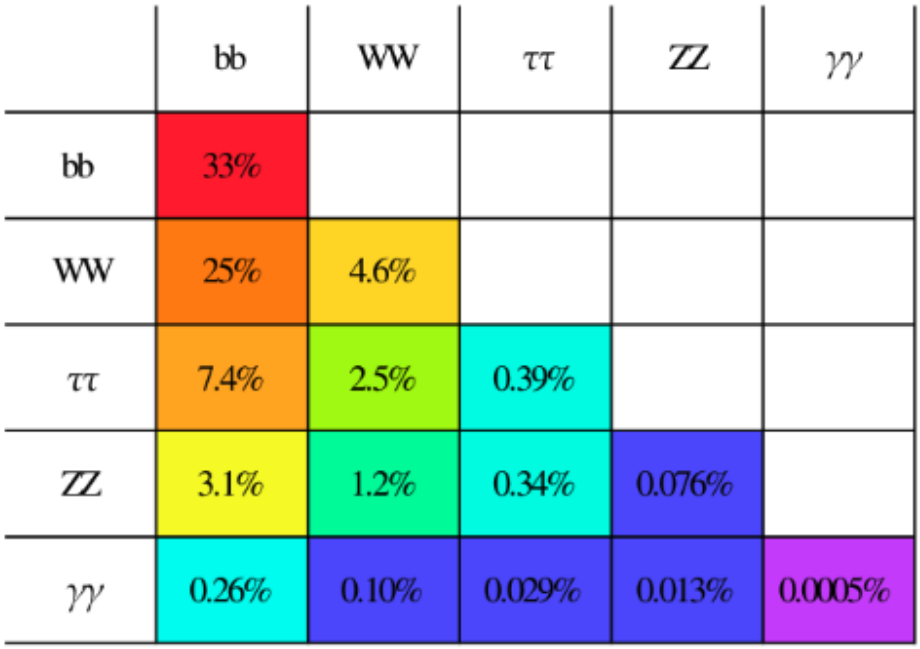


Figure 1.11: Di-Higgs boson system decay branching ratios [17].

Searches for non-resonant Higgs pair production have been performed in a number of final states, $\bar{b}b\bar{b}b$ [18], $\bar{b}b\tau^+\tau^-$ [19], $\bar{b}b\gamma\gamma$ [20], $W^+W^-\gamma\gamma$ [21], $\bar{b}bVV$ [22] and $W^+W^-W^+W^-$ [23] at $\sqrt{s} = 8$ TeV and $\sqrt{s} = 13$ TeV by ATLAS and CMS collaborations including the combination of multiple final states. The di-Higgs boson analyses in the $\bar{b}b\bar{b}b$, $\bar{b}b\tau^+\tau^-$ and $\bar{b}b\gamma\gamma$ decay channels are combined in order to extract constraints on the production cross-section and on the Higgs-boson self-coupling [24]. The result is shown in Figure 1.12.

In this thesis, the search for the non-resonant HH production in multilepton final states is described. Specifically, the final state of three light leptons (electrons or muons), which predominantly originate from the decay modes of $W^+W^-W^+W^-$ and $W^+W^-\tau\tau$ (with $\tau$ decaying leptonically) are considered.

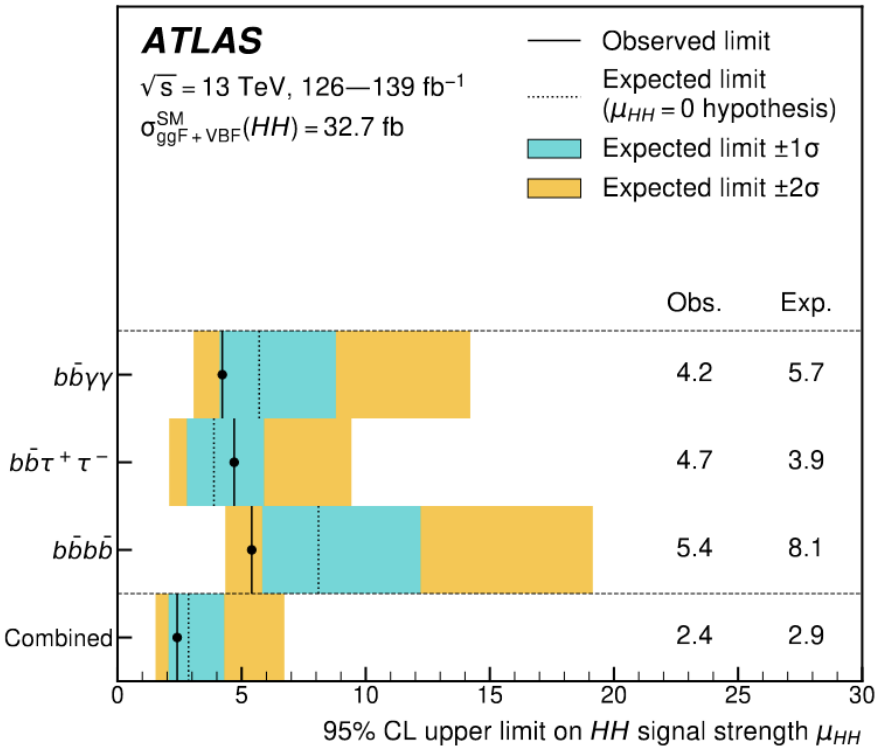


Figure 1.12: Observed and expected 95% CL upper limits on the signal strength for double-Higgs production from the $\bar{b}b\bar{b}b$, $\bar{b}b\tau^+\tau^-$ and $\bar{b}b\gamma\gamma$ decay channels, and their statistical combination. The expected limit and the corresponding error bands are derived assuming the absence of the HH process with all nuisance parameters profiled to the observed data. [24]

# Chapter 2

## Large Hadron Collider and ATLAS Experiment

### 2.1. Large Hadron Collider

The Large Hadron Collider (LHC) [25] is a circular accelerator and collider built and operated by the European Organization for Nuclear Research (CERN) that spans 27 km in circumference and is located on the border of France and Switzerland. Its main function is to collide high-energy beams of protons at a high rate and center-of-mass energy. Between 2015 and 2018, Run 2 saw the laboratory frame's center-of-mass energy at 13 TeV, and bunch crossings occurred every 25 nanoseconds, with each bunch containing about $10^{11}$ [26] protons. The source of the protons used in the LHC is hydrogen atoms [27], from which the protons are freed using an electric field. The protons then undergo acceleration in several RF cavities across multiple accelerators until they achieve their final energy level.

The proton acceleration process in the LHC is complex and involves linear and several circular accelerators, starting with the Linear Accelerator (Linac), which accelerates the proton bunches to 50 MeV. Subsequently, the Proton Synchrotron Booster raises the energy to 1.4 GeV, followed by the Proton Synchrotron, which boosts the bunches to 26 GeV. Lastly, the Super Proton Synchrotron (SPS) ramps up the proton energy to 450 GeV before delivering them to the LHC. The proton bunches at the LHC are accelerated to their final energy of center-of-mass collision, which is $\sqrt{s} = 13$ TeV as illustrated in Figure 2.1.

The LHC has four interaction points where collisions occur, and each point houses a detector designed to study specific types of physics. The LHCb experiment is a forward physics experiment specifically designed to study B physics [28], while the ALICE detector

studies nuclear physics. The ATLAS and Compact Muon Solenoid (CMS) [29] experiments are general-purpose detectors designed to study a broad range of physics phenomena. This analysis is performed using the Run 2 data collected by ATLAS detector.

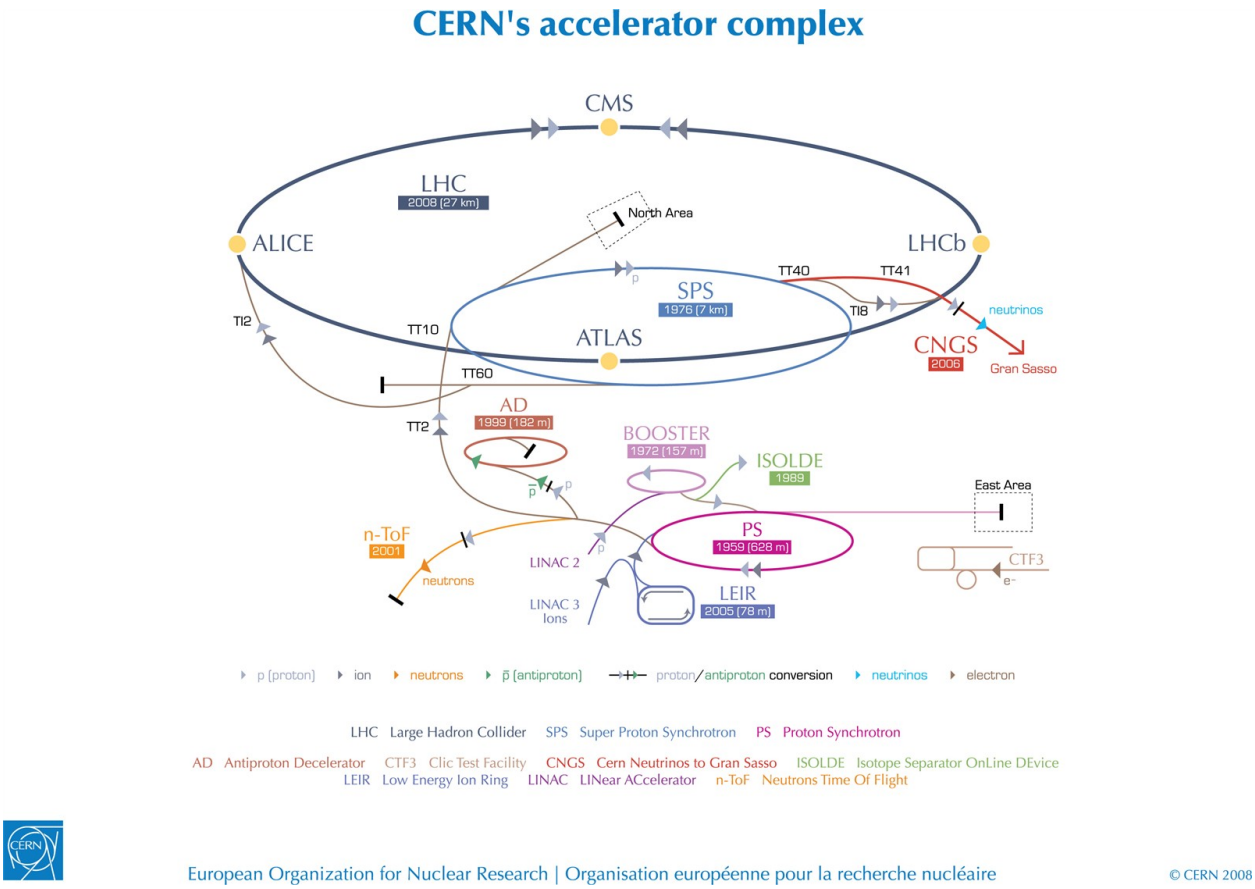


Figure 2.1: A schematic of the LHC with the various interaction points indicated [26].

## 2.2. ATLAS Detector

A Toroidal LHC ApparatuS (ATLAS) [30] is a general-purpose detector that is designed to reconstruct hadron collisions at the LHC. The detector has a cylindrical geometry that is symmetric along the forward-backward axis and encompasses a solid angle of almost $4\pi$, with respect to the interaction point. The ATLAS detector is massive, weighing over 7,000 tons, and it has a length of 44 meters and a diameter of 25 meters. It is situated 100 meters underground.

ATLAS detector is composed of multiple subsystems, which are arranged cylindrically. The subsystem closest to the interaction point is the inner detector, which measures the trajectory of charged particles as they bend through a 2T magnetic field generated by a solenoid that surrounds the inner detector. The inner detector is made up of three parts: the silicon Pixel Detector, the SemiConductor Tracker (SCT), and the Transition Radiation Tracker (TRT). The calorimeters, which are located outside of the inner detector, consist of two components. The first is the Liquid Argon (LAr) calorimeter, which measures electromagnetic radiation, while the second is the scintillating tile calorimeter, which measures hadronic radiation. Beyond the calorimeters, there is a 4T toroidal magnetic field, and the Muon Spectrometer to tracks muon trajectories. A schematic of the ATLAS detector is shown in Figure 2.2.

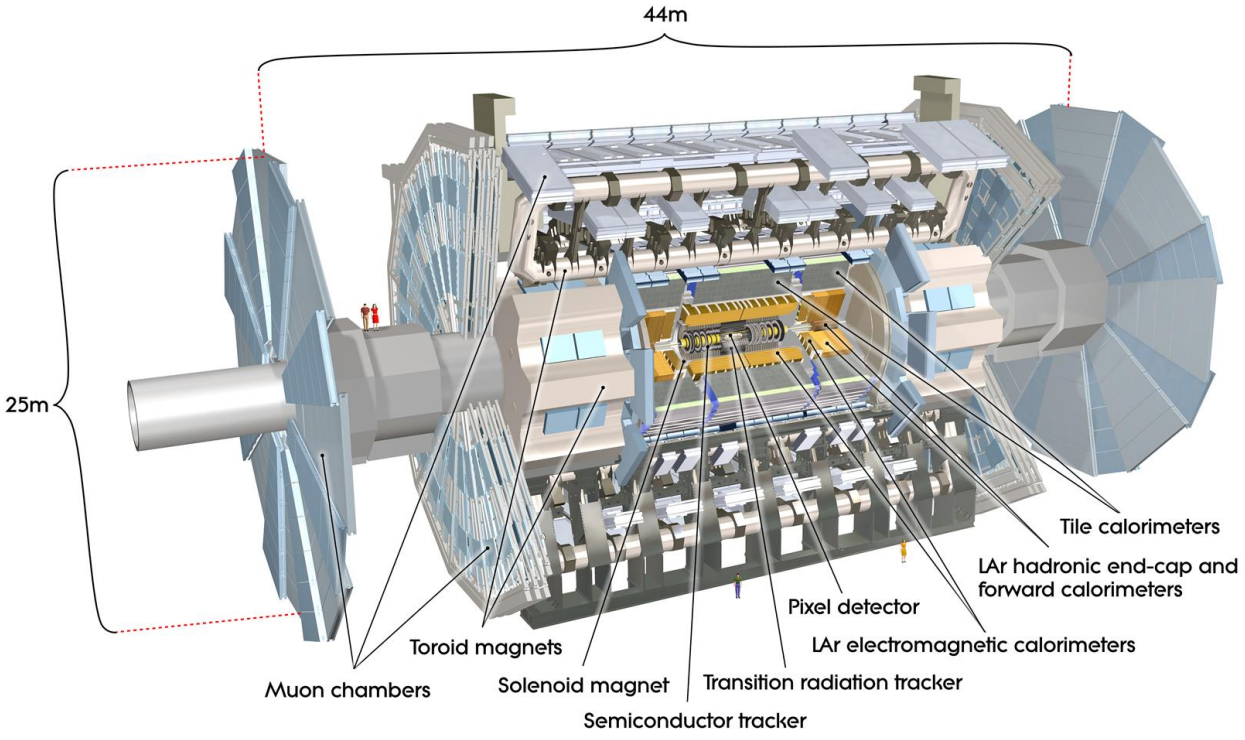


Figure 2.2: A schematic of the ATLAS detector [31].

ATLAS uses a two-stage triggering system to identify and record interactions that contain interesting physics. The first stage is hardware-based, while the second is software-based. The triggering system sends the identified interactions to the Data Acquisition (DAQ) system.

### 2.2.1. The ATLAS Coordinate System

In order to describe the position of particles within the ATLAS detector, a right-handed coordinate system is employed. The $z$-axis is aligned along the beamline, the $x$-axis points towards the center of the LHC, and the $y$-axis points upwards towards the Earth's surface. Transverse quantities such as transverse momentum, $p_T$, and transverse energy, $E_T$, are calculated within the x-y plane. The detector is divided into two halves: the 'A-side' which is pointed towards the Saleve and has positive $z$ coordinates, and the 'C-side' which is pointed towards the Jura and has negative $z$ coordinates.

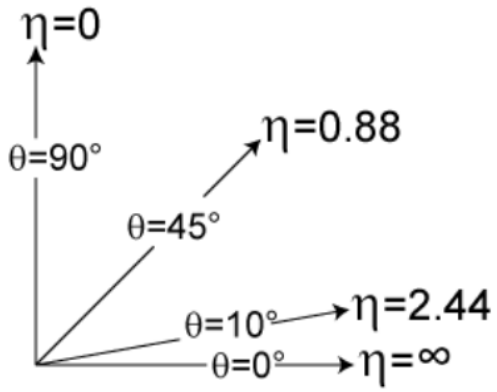


Figure 2.3: Pseudorapidity distribution shown on a polar grid.

The cylindrical coordinate system is also useful for describing the position of particles within the ATLAS detector due to its shape. The azimuthal angle, $\phi$, is measured around the beam axis with $\phi = 0$ being located along the positive x-axis. The polar angle, $\theta$, is measured from the beam axis, where $\theta = 0$ is parallel to the beampipe. The position of particles can

also be defined using pseudorapidity, which is a commonly used coordinate in high-energy physics. Pseudorapidity is defined in terms of the polar angle, $\theta$, as $\eta = -\ln[\tan(\theta/2)]$ as shown in Figure 2.3. This definition is used because it is invariant under boosts in the beam axis direction, and particle production is expected to be constant as a function of pseudorapidity for certain types of collisions. Therefore, pseudorapidity is a useful quantity for understanding the properties of the events reconstructed within the ATLAS detector. To describe distance between particles, the angle space in pseudorapidity and azimuth is commonly used. It is also Lorentz invariant under longitudinal boosts and defined as,

$$\Delta R = \sqrt{(\Delta\eta)^2 + (\Delta\phi)^2} \tag{2.1}$$

### 2.2.2. Magnet Systems

To obtain information about the charge and momentum of particles in the detector, a magnetic field is utilized. The curvature of a charged particle while traveling through a magnetic field can be used to determine the charge-to-mass ratio. The direction of the bend in the track indicates the polarity of the charge. The ATLAS magnet system is composed of four superconducting magnets, namely a central solenoid, a barrel toroid, and two end-cap toroids. The barrel toroids determine the size of the ATLAS detector, which spans 26 m along the beam axis and has an outer diameter of 22 m. Figure 2.4 displays a diagram of the magnet system's components.

The central solenoid [32] is located between the inner detector and the Electromagnetic (EM) calorimeter and generates a 2T magnetic field that is axially symmetric. This magnetic field causes charged particles to curve as they pass through the inner detector. To reduce the amount of material before the calorimeters, the solenoid was designed to be thin, with

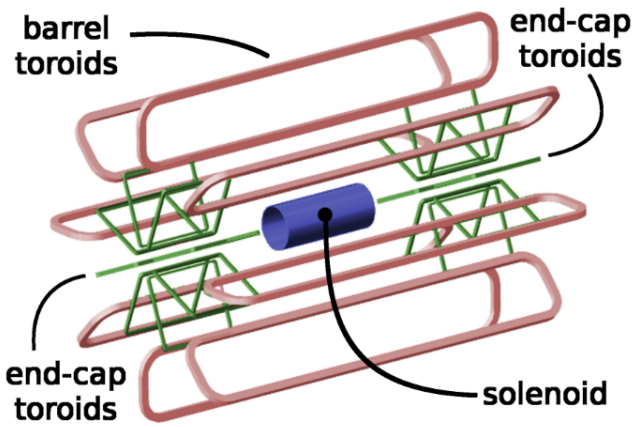


Figure 2.4: A schematic of the components of the magnet system in the ATLAS detector [32].

a single-layer coil consisting of 1173 turns of Al-stabilized $Nb/Ti$ conductor. It spans 5.3 m along the beam axis and has an outer diameter of 2.63 m.

The barrel toroid consists of eight coils in a flat racetrack shape that generate a symmetric radial magnetic field towards the beam axis with a peak field of 3.9 T [33]. The two end-cap toroids also consist of eight coils, are 5 m in length, have an outer diameter of 10.7 m, an inner bore of 1.65 m, and generate a peak field of 4.1 T. The end-cap toroids are inserted into the barrel toroid and aligned with the central solenoid. The three-toroid design was chosen over a single toroid to facilitate access to the core of the detector. The toroids work together to generate a magnetic field, which causes the muon trajectory to curve, for the muon system.

### 2.2.3. Inner Detector

The purpose of the inner detector [34] is to accurately determine the interaction point and trajectory of charged particles. The inner detector is divided into barrel and end-cap sections along the beam axis, with the barrel extending 1.6 meters and covering $|\eta| < 1$, while the end-cap sections cover the remaining 7 meters. With this configuration, the inner detector

can provide precise tracking up to $|\eta| < 2.5$. The inner detector comprises three subsystems: the Pixel Detector, the SemiConductor Tracker (SCT), and the Transition Radiation Tracker (TRT).

The Pixel Detector is located closest to the interaction point and offers high-precision measurements that aid in determining impact parameters. Pixel sensors are created by an n+ implant on an n-doped silicon substrate with dimensions $50\mu m \times 400\mu m$ and a depth of 250 $\mu m$. The detector consists of 1,744 modules, each with 46,080 readout channels, resulting in over 80 million pixels. The innermost layer, the Insertable B-Layer (IBL) [35], was installed between Run 1 and Run 2 and has smaller modules for finer granularity at $50\mu m \times 250\mu m$. The IBL is closer to the interaction point, located at a distance of R = 33.25 mm, compared to the previous first layer at R = 50.5 mm, aiding in the identification of displaced vertices from b-jets and photons that convert into an $e^+e^-$ pair.

The SCT provides measurements at intermediate range from the interaction point, which are essential for momentum, impact parameter, and vertex position measurements. The SCT is made up of a barrel region and two end-caps and covers the distance R = 300 mm to R = 520 mm from the IP. SCT modules are composed of four strip sensors, with two on each side, positioned at an angle of 40 mrad from each other. The sensors are single-sided p-in-n microstrip detectors on silicon wafers. The barrel consists of 2112 modules in four equally spaced layers, and each end-cap comprises 988 modules over nine disks, resulting in about 6 million silicon strips collectively.

The TRT serves as the outermost component of the inner detector, and covers a distance range of R = 554 mm to R = 1082 mm from the IP, with a pseudorapidity range of $|\eta| < 2.0$. Its role is to assist with pattern recognition for tracking, aid in momentum measurement, and provide discrimination between electrons and hadrons. It is made up of 372,032 proportional drift tubes, or straws, each with a 4 mm inner diameter. The straws are filled with a gaseous mixture composed of 70% Xe, 27% $CO_2$, and 3% $O_2$.

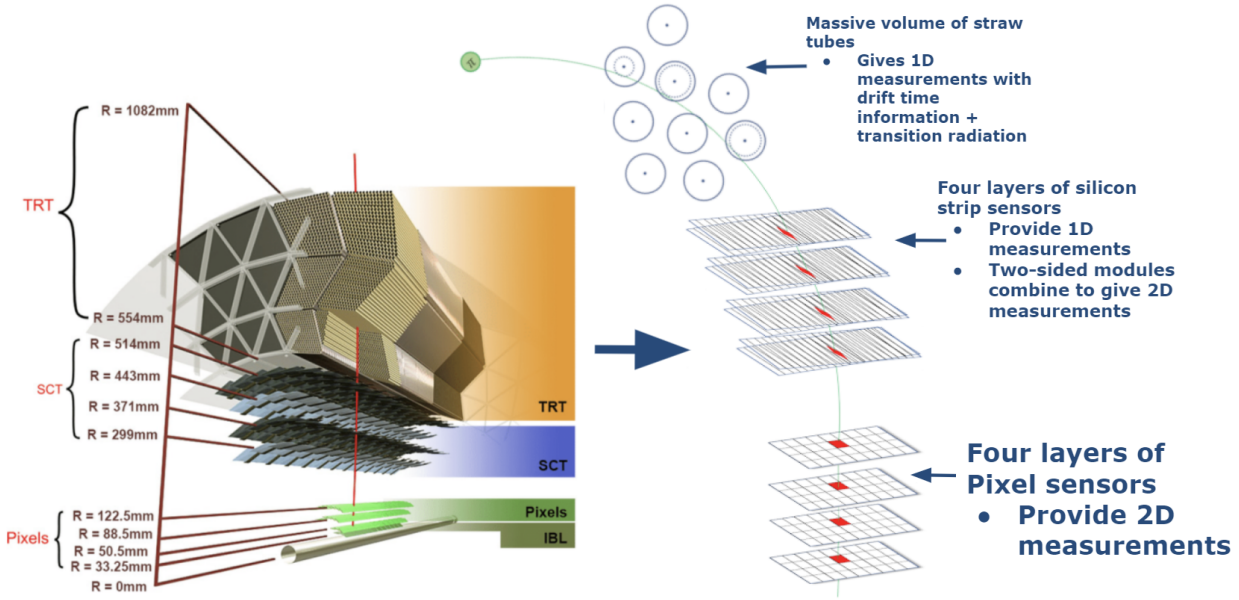


Figure 2.5: Schematic of the components of the ATLAS Inner detector [34].

As a charged particle travels through the straw, it deposits energy into the gas, creating electron-ion pairs. The electrons drift towards the center wire, while the ions drift towards the inner wall of the straw, producing an electrical signal that is compared to a low and high threshold. The low threshold measures drift time to derive the position of incidence, while the high threshold identifies large energy deposits from transition radiation X-rays, useful for distinguishing charged pions from electrons.

For momentum measurement, the TRT provides a precision equivalent to a single point with 50 µm precision, and for tracking, it provides approximately 36 hits per track. For electron-hadron discrimination, it has a pion rejection factor between 15 and 200 (depending on $\eta$) for pions with $p_T > 20$ GeV, with an electron efficiency of 90%.

### 2.2.4. Calorimeters

The primary purpose of the calorimeter system in ATLAS is to determine the energy of particles that are absorbed by its active material. Different types of particle showering are

targeted by ATLAS calorimeters. The Liquid Argon (LAr) electromagnetic (EM) calorimeter is designed to detect electromagnetic showers from photons and electrons, while the hadronic Tile calorimeter is intended for detecting hadronic showers. The EM calorimeter is located outside the inner detector and central solenoid, while the hadronic calorimeter is positioned outside of the EM calorimeter. A diagram of the calorimeter is shown in Figure 2.6.

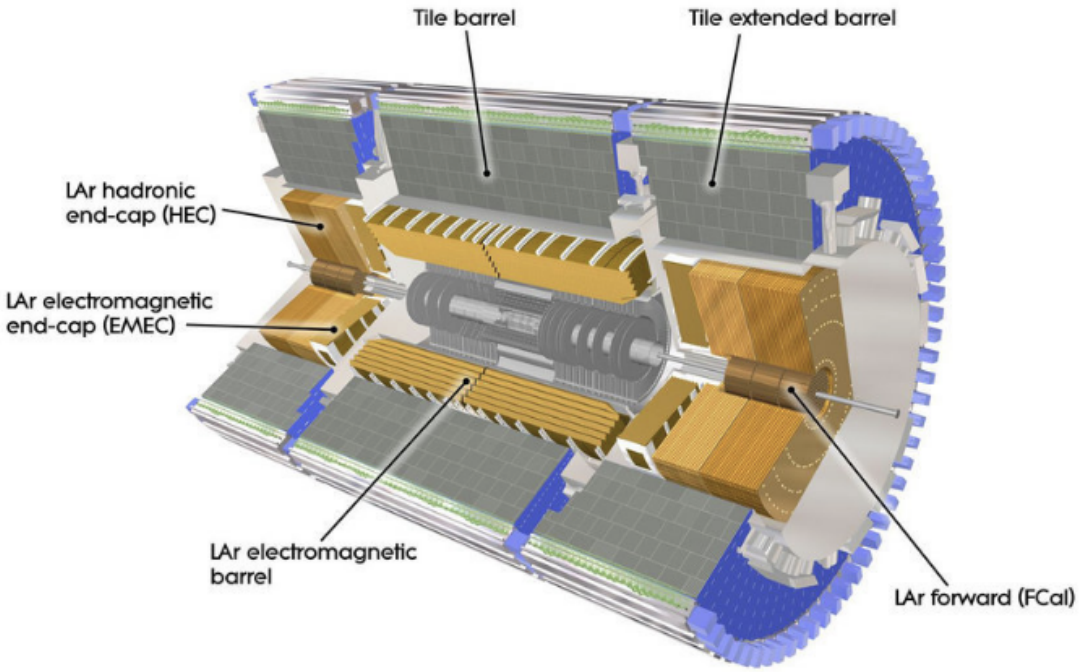


Figure 2.6: A schematic of the calorimeters in the ATLAS detector [30].

The electromagnetic calorimeter in the ATLAS detector is a sampling calorimeter that uses liquid argon (LAr) as the active material. Photons interacting with the LAr material primarily create $e^+e^-$ pairs when their energy is above 5 MeV. For lower energy photons, interaction occurs through either the photoelectric or Compton effect. Electrons interact through bremsstrahlung when their energy is above 1 MeV, which causes them to emit photons and lose energy. This process continues for the subsequent daughter particles, resulting in a showering effect within the calorimeter [36].

The LAr electromagnetic calorimeter is composed of absorbers with an accordion-style geometry and read-out electrodes, providing gapless azimuthal ($\phi$) symmetry. It is divided into three regions, the Electromagnetic Barrel (EMB) and two Electromagnetic End-Caps (EMEC), each with their own cryostat. A sketch of the composition of the EM calorimeter can be found in Figure 2.7.

The passive material used by the EMB is lead-stainless steel converters, with a coverage limit of $|\eta|< 1.5$. The detector is made up of two half-barrels, with 1024 converters and electrodes each, that come together at $|\eta|= 0$. The EMB is split into three layers longitudinally. The first layer is highly segmented in $\eta$, with granularity of $0.003 \times 0.1$ in $\Delta\eta \times \Delta\phi$, providing precise position information. The second layer has wider segmentation of $0.025 \times 0.025$ and absorbs most of the EM shower, while the last layer has lower granularity in $\eta$ of $0.05 \times 0.025$ and is used to pick up EM shower tails. In total, these layers cover more than 22 radiation lengths ($X_0$) and consist of a total of 101,760 channels.

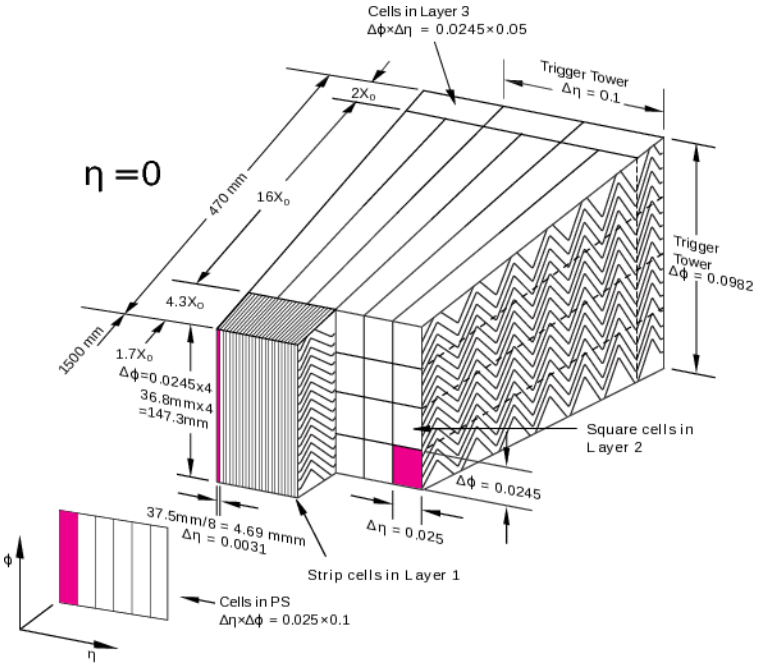


Figure 2.7: A schematic of the LAr EM calorimeter in the ATLAS detector [37].

The EMEC component of the ATLAS calorimeter system is also constructed using a combination of lead and stainless steel as the passive material. It is composed of two wheels, with the inner wheel covering the region $1.4 < |\eta| < 2.5$ and the outer wheel covering the region $2.5 < |\eta| < 3.2$. The EMEC provides coverage for more than 24 $X_0$. A transition region between the EMB and EMEC spans the range $1.37 < |\eta| < 1.52$, and it is used for detector servicing.

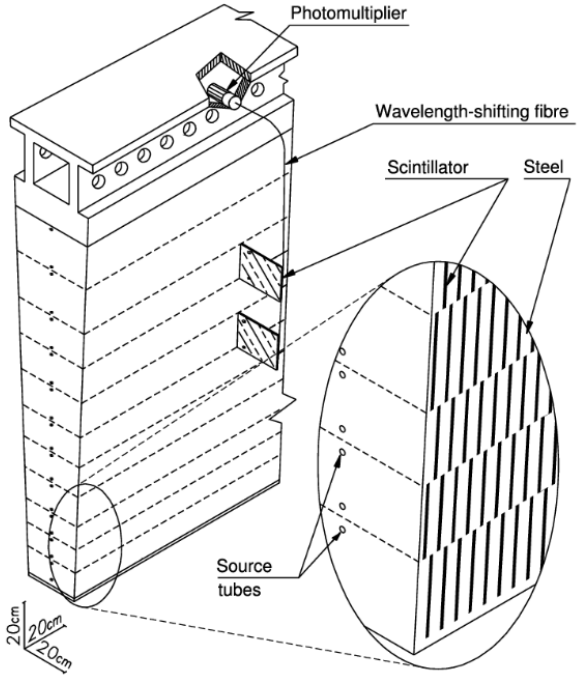


Figure 2.8: Schematic of the Tile Calorimeter [38].

The scattering of hadrons in matter results in the production of secondary hadrons, protons, and neutrons, which decay to create a cascade of particles known as a hadronic shower. This cascade continues until the energy of the decay products is low enough to be stopped by ionization energy loss or nuclear absorption. To measure the energy of these particles, the Hadronic Tile Calorimeter is used, which employs steel as the absorber and scintillating tiles as the active material. The scintillators transmit light through fiber optics to photomultiplier tubes. The Hadronic Calorimeter is made up of three regions, with each region having 64 azimuthal modules and three layers longitudinally. The first two layers have

a granularity of $0.1 \times 0.1$ in $\Delta\eta \times \Delta\phi$, while the third layer is $0.2 \times 0.1$. The thickness of the calorimeter is more than 9.7 interaction lengths ($\lambda$). A schematic of the Tile Calorimeter can be seen in Figure 2.8. In addition, the Hadronic End-Cap (HEC) also detects hadronic decays, covering a pseudorapidity range of $1.4 < |\eta| < 3.2$. The HEC uses LAr as the active material and copper plates as the passive material. Each end-cap consists of 32 wedge-shaped modules and two segments in depth, resulting in four samplings per end-cap, and is located behind the EMECs, sharing their cryostats.

The Forward Calorimeter (FCal) is responsible for detecting particles in the forward regions where $3.1 < |\eta| < 4.9$. To withstand the radiation damage that is expected at high values of $\eta$, the FCal also employs liquid argon as the active material and a combination of copper and tungsten as the absorber.

### 2.2.5. Muon Spectrometer

The Muon Spectrometer (MS) [39] is located on the outermost layer of the ATLAS detector and its main purpose is to track muons via independent triggering (for $|\eta| < 2.4$) and momentum measurement (for $|\eta| < 2.7$). The final trigger decision is made by combining triggers based on the MS with information from the inner detector, making good timing resolution imperative. Timing information is collected in the Resistive Plate Chambers (RPC) and Thin Gap Chambers (TGCs), which both have a timing resolution better than 4.5 ns. The RPCs cover the barrel region ($|\eta| < 1.05$), while the TGCs cover the end-cap region ($1.0 < |\eta| < 2.4$). Momentum information is provided through Monitored Drift Tube Chambers (MDTs), which consist of Al tubes that are 30 mm in diameter and filled with a 0.05 mm gold-plated tungsten wire in the center. Three layers of MDTs cover the central region of the MS at $|\eta| < 2.7$. In the forward region ($2.0 < |\eta| < 2.7$), the first layer of MDTs is replaced by Cathode Strip Chambers (CSCs), which are multi-wire proportional chambers with precision cathode strips. A schematic of the MS can be found in Figure 2.9.

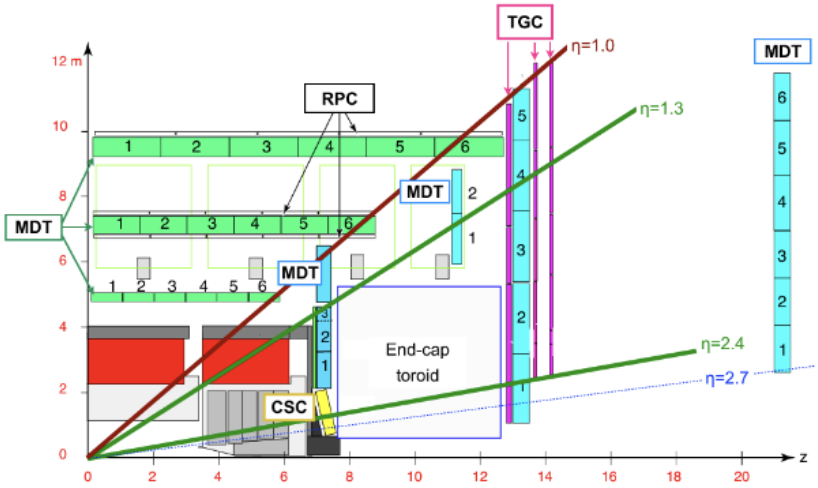


Figure 2.9: A schematic of a quarter of the Muon Spectrometer [39].

### 2.2.6. Trigger and Data-Acquisition

The ATLAS detector observes collisions happening at a rate of 40 MHz, with over 100 million channels for readout and an average event size of 1.6 MB. This results in a data flow of 1 TB/s which is challenging to store, so the ATLAS trigger system follows a tiered approach to reduce the data flow to about 1 kHz for permanent storage. The system includes two stages: the level 1 (L1) trigger which is hardware-based, and the software-based High Level Trigger (HLT) [40]. The L1 trigger uses rough measurements of various objects such as leptons, photons, and jets to select interesting events. Jet triggers use calorimeter towers with a $0.1 \times 0.1$ segmentation in the $\eta$-$\phi$ plane, whereas muon triggers detect coincidences in the muon spectrometer trigger chambers which have low resolution but high readout rate. The L1 trigger accepts events at a rate of 100 kHz. On the other hand, HLT accepts events at a rate of approximately 1 kHz. A schematic of the pipeline for trigger decisions in conjunction with the DAQ system is shown in Figure 2.10.

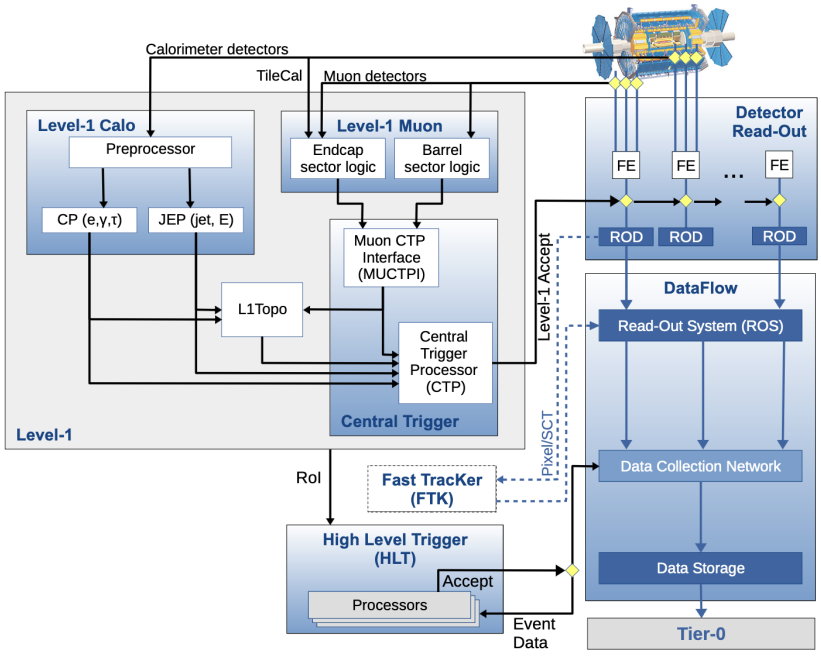


Figure 2.10: The ATLAS Trigger and DAQ systems during the Run 2 data taking period [41].

# Chapter 3

## Object Reconstruction

In order to accurately understand and interpret results, it is crucial to compare them with theoretical predictions, especially in the case of particle colliders where an understanding of the underlying mechanism and detector effects is necessary. ATLAS employs Monte Carlo (MC) simulation to achieve this, which involves randomly sampling the probability distribution of a process using a probability distribution function. The ATLAS simulation chain progresses through a series of MC integration steps, with each step being Markovian, meaning that the process depends solely on the previous step and sampling is performed on the posterior distribution. Markov Chain MC (MCMC) is utilized to generate MC from a series of Markovian processes, making it useful for simulating complex processes such as particle collisions. The ATLAS simulation structure follows sequential steps of event generation, parton showering, hadronization, detector simulation, and reconstruction of physics objects to generate MCMC.

The initial stage of the ATLAS simulation involves creating the hard-scatter process, which is done using parton distribution functions when simulating collisions. A parton is a type of strongly interacting particle, such as a quark or gluon, that makes up protons. In proton-proton collisions, it is these partons that interact with one another, and distribution functions are used to model this interaction. These functions provide information on the likelihood of finding a parton carrying a specific fraction of the proton's momentum.

The matrix element (ME) generators, such as MadGraph [42], Sherpa [43], or Powheg [44], calculate the matrix elements for the specific scattering processes of interest. These matrix elements describe the probabilities and kinematics of the particle interactions at the fundamental level. They take into account the underlying physics and fundamental interactions, including the electroweak and strong interactions.

The output of the matrix element generators provides information on the kinematics of the particles produced in the hard scattering process, such as their momenta, flavors, and quantum numbers. This information serves as input to the subsequent parton showering process. Following the interaction, the simulation needs to model parton showering. QCD bremsstrahlung radiation in the form of gluons is emitted during the hard scatter processes. These emitted gluons carry color charge and can undergo further radiation, which is referred to as parton showering. Generators use a sequence of one-to-two parton branching to approximate these higher-order QCD corrections. This process is iteratively performed until it reaches the non-perturbative regime, which is around 1 GeV. Three event generators in the ATLAS software have parton showering built in: Pythia [45], Herwig [46] and Sherpa [43].

The conversion of partons into hadrons occurs when the former have reduced energy levels. This process is referred to as hadronization (details on Section 3.7). Since it is non-perturbative, it relies on phenomenological models tuned on data.

After the hadronization process, the model represents a complete description of the process, independent of the detector. The next step is to simulate how particles will interact with the ATLAS detector. To accomplish this, a component-level model of the ATLAS detector is implemented in Geant4 [47], and particles are propagated through this model. Stochastic calculations are performed to determine the energy deposition in each detector

component, resulting in a collection of hits. The electrical response for these hits in each detector component is simulated, and output in a format that matches that of actual data collection. This information is used to reconstruct physics objects in the same way as real data.

## 3.1. Object Reconstruction

Once particles have left their traces in the various layers of the ATLAS detector, reconstruction algorithms are employed to connect the signatures across subsystems and interpret them as 'physics objects'. This process involves identifying the low-level objects such as tracks and topoclusters that represent the trajectory of charged particles and single-particle energy deposits within the calorimeters, respectively. These primary inputs are then combined to identify the primary vertex and various signatures in each event. Specifically, this chapter will focus on low-level objects i.e, tracks, topoclusters and physics objects i.e, jets, electrons , muons which are objects used in this analysis.

## 3.2. Tracks

Charged particles passing through the layers of the inner tracker create signals called hits, which provide information on their path through the sensors. These hits are combined to reconstruct the helical trajectory of the charged particles, which are called tracks. ATLAS defines a track using five global track parameters, as shown in Figure 3.1. $d_0$ refers to the perpendicular distance between the primary vertex and the point of closest approach in the transverse plane, while $z_0$ is the longitudinal distance along the z-axis at the point of closest approach in the transverse plane. $d_0$ and $z_0$ are called transverse impact parameter and longitudinal impact parameter respectively. $\phi$ and $\theta$ indicate the track angle relative to

the x-axis and z-axis respectively at the point of closest approach. The ratio of charge to momentum (q/p) is calculated based on the track's curvature in the magnetic field.

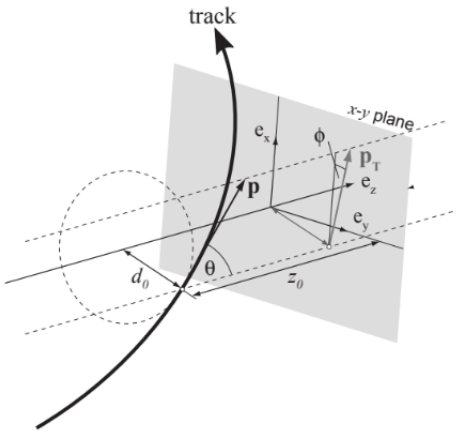


Figure 3.1: Global Track Parameters [48].

In ATLAS, tracks must pass quality requirements to eliminate tracks from low-energy particles and fake tracks resulting from noise and combinations. The 'loose' tracks must have $p_T$ greater than 500 MeV, $|\eta|$ less than 2.5, a minimum of 7 silicon hits, no shared hits, 2 or fewer 'holes' in the pixel and semiconductor tracker, and 1 or fewer pixel 'holes'. 'Holes' are layers of the tracker that the track passes through without registering any hits. The 'tight' tracks must fulfill additional requirements, including having 9 or more silicon hits if $|\eta|$ is less than 1.65 (barrel region) or 11 or more hits if $|\eta|$ is greater than 1.65 (endcap region), at least one hit in one of the two innermost pixel layers, and no holes in the pixel detector [49].

### 3.3. Primary Vertex

The primary goal of primary vertex reconstruction is to identify the specific proton-proton interaction that resulted in a hard-scatter event. To begin the process of vertex reconstruction, 'tight' tracks are utilized. A candidate vertex is considered when at least two 'tight' tracks intersect. The accuracy of the longitudinal and transverse resolution for vertex reconstruction along the beamline is about $30\mu m$ and $10-12\mu m$, respectively. In cases

where multiple proton-proton collisions occur in the same bunch crossing (refer as pile-up), numerous candidate vertices may exist. Therefore, the primary vertex is typically determined by selecting the vertex with the highest squared transverse momentum of associated tracks. All physics objects are then derived with reference to the selected primary vertex.

### 3.4. Topological Clusters

Topological clusters also known as topocluster are entities that represent the energy deposited by individual particles in the calorimeters. These clusters are created by combining signals across multiple calorimeter cells. When a particle interacts with the calorimeters, it deposits energy across multiple cells, and topoclusters are introduced to merge this energy into a single object [50]. To initiate a topocluster, the energy deposited must exceed the local cell-level thresholds for electronic noise and pile-up by 4 standard deviations. The expected values of electronic noise and pile-up vary depending on the size of the cell and its location within the detector. Once a topocluster is seeded, adjacent cells are added to the topocluster if the energy exceeds two standard deviations of the expected noise. If the topocluster has two distinct maxima, it is split in two. An event-by-event origin correction is then applied to every topocluster based on its depth within the calorimeter and $\eta$. Finally, topoclusters are calibrated to provide a consistent response for electromagnetic showers from electrons or photons.

### 3.5. Electrons

Electron reconstruction involves using the energy deposits measured within the electromagnetic calorimeter ($|\eta| < 2.47$) in combination with tracks from the inner detector [51]. The process for identifying electrons relies on analyzing the shower shapes in the EM calorimeter to ensure that they correspond to those expected from an electron. Furthermore, track-cluster matching is utilized to verify whether an electron track can be linked to the shower.

### 3.6. Muons

To begin the reconstruction of muons, high-quality tracks found in the muon spectrometer are utilized. The muon track candidates are then combined with tracks in the inner detector through a global fit. Muons can be accurately identified and measured over a wide range of $p_T$ values [52].

### 3.7. Jets

Color confinement is a phenomenon that prevents strongly interacting particles from existing independently, which means that partons produced in pp collisions cannot exist alone. Instead, they undergo a process called showering, which leads to the creation of additional strongly interacting particles through splitting and radiation. As a result, a large number of subsequent partons are produced, which are almost collinear. These partons eventually reach a low enough energy level, around 1 GeV, and hadronize to form a colorless state, such as mesons or baryons, that deposit energy into the calorimeters. This group of interactions, all occurring in the same general direction as the initial parton, is referred to as a 'jet'.

The objective of reconstructing jets is to recognize the groups of particles that are produced by quarks and gluons during hadronization. To form jets, a mixture of topoclusters and tracks known as 'particle flow objects' are clustered together. These particle flow objects use charged particle energy resolution measured by the inner detector and energies measured in the topoclusters. The inner detector provides better energy resolution for lower energy charged particles, while the calorimeter provides better energy resolution for neutral particles and high energy (>100 GeV) particles. In order to generate particle flow objects, topoclusters are paired with individual tracks in the calorimeter. If the track's $p_T$ exceeds a threshold set by a parameter, the track's $p_T$ is subtracted from the topocluster energy. If the track's $p_T$ is greater than the topocluster energy, the topocluster is entirely removed.

However, if it is less than the topocluster energy, the energy is subtracted cell-by-cell [50].

The clustering of jets using particle flow objects involves applying the anti-$k_t$ algorithm [53] and measuring the distance between two input objects. This algorithm looks for the combination of topoclusters that minimizes the distance measure until all particles have been used. The algorithm favors the smallest distance between two input objects to cluster high $p_T$ objects that are close together first, with R determining the angular scale of the clustering. This results in two common jet definitions in ATLAS: small and large radius jets. Once the jets have been clustered, they must be calibrated using a multi-step process that combines simulation and data-driven techniques. The calibration accounts for factors that affect the jet response, such as pile-up, biases introduced by the jet clustering algorithm, detector geometry effects, and differences between data and simulation. The Jet Energy Scale (JES) is the average of the ratio between the reconstructed jet energy and the true jet energy, while the Jet Energy Resolution (JER) is the width of the fitted jet response distribution, and it is ideal for this width to be as small as possible [54].

### 3.8. Impact Parameter (IP) Resolution

For the analysis presented in this thesis, jets initiated by b-quark i.e. b-jets are vetoed. The b-tagging relies on the fact that the average lifetime for hadrons containing b quarks is longer than that of a hadron that involves lighter quarks. Thus, b-hadrons typically travel a longer distance in the inner detector, producing a displaced secondary vertex. The impact parameter resolution is crucial in the reconstruction of secondary vertices which eventually used in b-jet identification and vetoing it. This section focus on work that I perform for my ATLAS authorship qualification task where I study of impact parameter resolution in di-jets events. This study was done for 2017 and 2018 data and IP resolution uncertainties were provided for release21 [55]. Figure 3.2 shows the intrinsic impact parameter resolution of tracks within jets in the transverse, $\sigma_{d_0}$, and longitudinal, $\sigma_{z_0}$,directions measured in the

di-jet triggered pp collisions data taken in 2017 and 2018 [55]. The tracks are associated to jets via by the ghost-association technique [56]. Only tracks that pass the TightPrimary selection are considered for the measurement.The intrinsic impact parameter resolution is extracted in bins of $p_T$ and $\eta$ of the tracks using an iterative Gaussian fit procedure and primary vertex position resolution is deconvoluted from the measured total resolution using an iterative unfolding method [57].

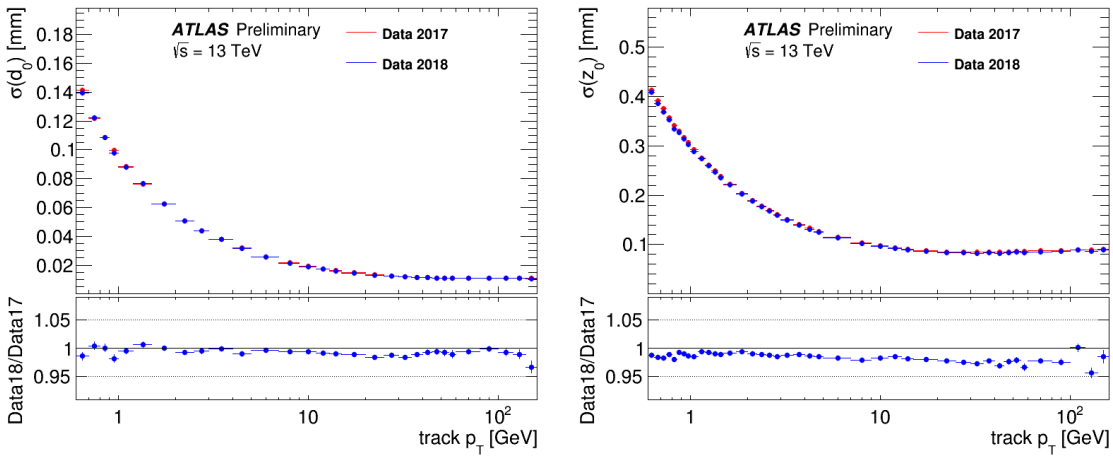


Figure 3.2: The intrinsic transverse impact parameter resolution $\sigma_{d_0}$(left) and longitudinal impact parameter resolution $\sigma_{z_0}$(right) for TightPrimary tracks associated to jets with $p_T > 20$ GeV measured in di-jet triggered pp collisions data collected in 2017 (Red) and 2018 (Blue) [55].

### 3.9. Missing Transverse Energy

The concept of missing transverse energy is based on the assumption that the momentum in the transverse plane is negligible before a collision takes place. It is used to determine the amount of energy that has evaded the detector by calculating the negative vector sum of all reconstructed objects.

# Chapter 4

## Search for Di-Higgs in Multi-Lepton Channel

This study aims to detect the production of two Higgs bosons, decaying through different channels with the final state which include three light leptons (electrons or muons) plus jets in non-resonant processes. Typically, the decay modes of HH to $W^+W^-W^+W^-$ and $W^+W^-\tau^+\tau^-$ ($\tau$ decaying leptonically) contribute significantly in final state., i.e $HH \rightarrow 3\ell 0\tau_h$ + jets, where $\tau_h$ is $\tau$ decaying hadronically. There are many different ways that a Higgs boson pair can decay, but some of these have a low probability of occurring as shown in Figure 1.11. Furthermore, the process of fully reconstructing the Higgs boson pair is difficult due to the complicated combinatorial issues. However, this analysis takes a different approach by focusing on final states without emphasizing any specific decay mode. The decay channel in $3\ell 0\tau_h$ is attractive for investigation due to its clean lepton signature and small backgrounds. The dominant background process for this analysis is the decay of $WZ$. This analysis is performed utilizing full Run 2 data from 2015 to 2018 (140 fb$^{-1}$) at $\sqrt{s}$ = 13 TeV. The analysis uses a multivariate approach (boosted decision trees) to separate the HH signal from the background processes. The analysis did not find any evidence of HH production, but it was able to set tight limits on the production of standard model HH and it is one of the strongest of multi-lepton channels.

### 4.1. Derivation and Analysis Framework

The initial data files obtained from ATLAS are extremely large. To overcome this challenge, a preselection procedure is employed to decrease the data volume by applying specific criteria and cuts prior to analysis. Initially, the data is formatted in the eXtensible Analysis Object Data (xAOD) format, which facilitates efficient access and analysis. To investigate

signal events featuring multilepton in the final states, a derivation framework is utilized to further convert the xAOD data into the Derived eXtensible Analysis Object Data (DxAOD) format. This framework incorporates additional techniques for reducing the data and selecting relevant information tailored to the desired physics processes. The resulting DxAOD format contains a subset of the original data, optimized for quicker and more targeted analysis, thereby enabling efficient exploration of multilepton signal events. This process is implemented for both the collision dataset and Monte Carlo (MC) samples.

## 4.2. Data and Monte Carlo Samples

In this study, data from proton-proton collisions at a center-of-mass energy of 13 TeV collected by the ATLAS experiment between 2015 and 2018 was used. The dataset used in the analysis was subject to quality requirements and had an integrated luminosity of 140.0fb$^{-1}$. On average, there were 34.2 inelastic proton-proton interactions per bunch crossing.

Monte Carlo (MC) simulations are used to model the HH signal and background processes. There are three MC campaigns used for each simulated process, mc16a, mc16d and mc16e, which correspond to different assumptions on the distribution of the number of interactions per bunch crossing in 2015-2016, 2017 and 2018 periods, respectively. To ensure consistency with the number of interactions observed in the data, the MC samples are reweighted. This procedure adjusts the simulated samples to match the observed distribution of interactions. Furthermore, the simulated samples are normalized to their respective cross sections, providing a reliable basis for comparison with the experimental data.

### 4.2.1. Signal Samples

- Nominal ggF signal samples:

  The event generation is performed at the next leading-order (NLO) accuracy with Powheg-Box-V2 [44] for matrix element calculation. Parton showering and hadroniza-

tion are simulated using the PYTHIA8 generator with the set of tuned parameters (A14 tune) [58] and using the NNPDF 2.3 LO PDF set [59]. The NNPDF2.3LO PDF is a specific set of Parton Distribution Functions (PDF). PDF describe the probability distributions of the momentum and energy carried by the partons (quarks and gluons) inside a proton or other hadrons. Detector effects are simulated using AltFastII(AF2) [60], with a fast simulation of the calorimeter response. The Higgs are allowed to decay to WW/ZZ/$\tau\tau$. A lepton filter is applied for multilepton channel targeting final states of $3\ell 0\tau$ . In addition, a specific selection criterion for leptons is considered to limit the lepton kinematic at $p_{\mathrm{T}} > 7$ GeV and $|\eta| < 3$.

- Alternative ggF signal samples:

  The alternative signal samples are produced by Powheg-Box-V2 interface to Herwig7, using PDF4LHC15 PDF set to study the parton shower uncertainties. The filtering strategy is in line with baseline samples.

- Nominal VBF signal samples:

  The event generation is performed at the leading-order (LO) accuracy with MADGRAPH5_aMC@NLO 2.2.X or 2.3.X [42] for matrix element calculation. Parton showering and hadronization are simulated using the PYTHIA8 generator with the A14 tune [58] and using the NNPDF 2.3 LO PDF set [59]. Detector effects are simulated using AltFastII(AF2) [60], which is a fast simulation of the calorimeter response.

  – The branching ratios of the intermediate particles are set to BR($H \to W^+W^-$) = 0.706, BR($H \to Z^0Z^0$) = 0.087 and BR($H \to \tau^+\tau^-$) = 0.207 to be consistent with the ggF values. In addition, a specific selection criterion for leptons is considered to limit the lepton kinematic at $p_{\mathrm{T}} > 7$ GeV and $|\eta| < 3$.

- Alternative VBF signal samples:

  The alternative signal samples are produced by MadGraph5_aMC@NLO 2.2.X or 2.3.X [42] interfaced to Herwig7, using PDF4LHC15 PDF set to study the parton shower uncertainties. The filtering strategy is in line with baseline samples.

#### 4.2.2. Background Samples

Table 4.1 displays the configurations used to generate Monte Carlo simulation samples for various signal and background processes. The samples used to estimate systematic uncertainties are indicated in parentheses. Pile-up events were modeled using minimum-bias interaction events generated with Pythia8.186 [61] and the NNPDF2.3LO PDF set, along with the A3 set of tuned parameters [62]. The pile-up events were then overlaid onto the simulated hard-scatter events based on the luminosity profile of the recorded data.

The generated events were processed through a simulation of the ATLAS detector geometry and response [63] using Geant4 [64]. The same reconstruction software used for the data was then applied to the simulated events. Corrections were made to ensure that the particle candidates' selection efficiencies, energy scales, and energy resolutions matched those determined from data control samples. The simulated samples were normalized to their cross sections and calculated to the highest available order in perturbation theory as summarized in table 4.2.

Table 4.1: The configurations used for event generation of different background processes.

| Process | Generator | ME order | Parton shower | PDF | Tune |
|---|---|---|---|---|---|
| $t\bar{t}W$ | Sherpa 2.2.10 | NLO | Sherpa | NNPDF3.0 NNLO | Sherpa default |
| | (MG5_aMC) | (NLO) | (Pythia 8) | (NNPDF3.0 NLO) | (A14) |
| $t\bar{t}t\bar{t}$ | MG5_aMC | NLO | Pythia 8 | NNPDF3.1 NLO | A14 |
| | (Sherpa 2.2.10) | (NLO) | (Sherpa) | (NNPDF3.0 NNLO) | (Sherpa default) |
| $t\bar{t}H$ | Powheg-BOX [65] | NLO | Pythia 8 | NNPDF3.0 NLO [59] | A14 |
| | (Powheg-BOX) | (NLO) | (Herwig7) | (NNPDF3.0 NLO) | (H7-UE-MMHT) |
| | (MG5_aMC) | (NLO) | (Pythia 8) | (NNPDF3.0 NLO) | (A14) |
| $t\bar{t}(Z/\gamma^* \to l^+l^-)$ | Sherpa 2.2.11 | NLO | Sherpa | NNPDF3.0 NNLO | Sherpa default |
| | (MG5_aMC) | (NLO) | (Pythia 8) | (NNPDF3.0 NLO) | (A14) |
| $t\bar{t} \to W^+bW^-\bar{b}l^+l^-$ | MG5_aMC | LO | Pythia 8 | NNPDF3.0 LO | A14 |
| $t(Z/\gamma^*)$ | MG5_aMC | NLO | Pythia 8 | NNPDF2.3 LO | A14 |
| $tW(Z/\gamma^*)$ | MG5_aMC | NLO | Pythia 8 | NNPDF2.3 LO | A14 |
| $t\bar{t}W^+W^-$ | MG5_aMC | LO | Pythia 8 | NNPDF2.3 LO | A14 |
| $t\bar{t}$ | Powheg-BOX | NLO | Pythia 8 | NNPDF3.0 NLO | A14 |
| | (Powheg-BOX) | NLO | (Herwig7.1.3) | (NNPDF3.0 NLO) | (H7-UE-MMHT) |
| $t\bar{t}t$ | MG5_aMC | LO | Pythia 8 | NNPDF2.3 LO | A14 |
| $s$-, $t$-channel, $Wt$ single top | Powheg-BOX [66] | NLO | Pythia 8 | NNPDF3.0 NLO | A14 |
| $VV$, $qqVV$, $low m_{\ell\ell}$, $VVV$ | Sherpa 2.2.2 | NLO | Sherpa | NNPDF3.0 NNLO | Sherpa default |
| $Z \to l^+l^-$ | Sherpa 2.2.1 | NLO | Sherpa | NNPDF3.0 NLO | Sherpa default |
| $Z \to l^+l^-$ (matCO) | Powheg-BOX | NLO | Pythia 8 | CTEQ6L1 NLO | A14 |
| $Z \to l^+l^-$+($\gamma$*) | Powheg-BOX | NLO | Pythia 8 | CTEQ6L1 NLO | A14 |
| $W$+jets | Sherpa 2.2.1 | NLO | Sherpa | NNPDF3.0 NLO | Sherpa default |
| $VH$ | Powheg-BOX | NLO | Pythia 8 | NNPDF3.0 NLO | A14 |
| $t\bar{t}ZZ$ | Madgraph | LO | Pythia 8 | NNPDF2.3 LO | A14 |
| $t\bar{t}HH$ | Madgraph | LO | Pythia 8 | NNPDF2.3 LO | A14 |
| $t\bar{t}WH$ | Madgraph | LO | Pythia 8 | NNPDF2.3 LO | A14 |

In Table 4.1, the samples used to estimate the systematic uncertainties are indicated in between parentheses. $V$ refers to the production of an electroweak boson ($W$ or $Z/\gamma^*$). The PDF shown in the table is the one used for the matrix element (ME). If only one PDF is

Table 4.2: The background sample normalizations and their uncertainties.

| Process | Precision order | Cross section central value | Cross section uncertainty | Modelling uncertainty | Normalized to data |
|---|---|---|---|---|---|
| MC samples contributing to fake lepton templates | | | | | |
| $t\bar{t}$ | NNLO+NNLL | 832 pb | - | alternative MC | Yes |
| $s$-, $t$-channel single top | NLO | 227 pb | - | - | Yes |
| $Wt$ single top | NNLO approx | 71.7 pb | - | - | Yes |
| $Z \to l^+l^-$ | NNLO | 0.9751×Sherpa | - | - | Yes |
| MC samples of irreducible background processes | | | | | |
| $t\bar{t}W$ | NLO | 601 fb | - | alternative MC<br>scale variations | Yes |
| $t\bar{t}t\bar{t}$ | NLO | 12 fb | 20% | alternative MC | No |
| $t\bar{t}(Z/\gamma^* \to l^+l^-)$ | NLO | 839 fb | - | alternative MC<br>scale variations | Yes |
| $t\bar{t}H$ | NLO | 507 fb | 11% | alternative MC<br>scale variations | No |
| $VV$, $qqVV$ | NLO | Sherpa | - | 10% (+LF jets),<br>scale variations | Yes (+HF jets) |
| $t(Z/\gamma^*)$ | LO | 240 fb | 5% | - | No |
| $t\bar{t}t$ | LO | 1.6 fb | 50% | - | No |
| $tW(Z/\gamma^*)$ | NLO | 16 fb | 50% | - | No |
| $t\bar{t}W^+W^-$ | NLO | 9.9 fb | 50% | - | No |
| $VVV$ | NLO | Sherpa | 50% | - | No |

shown, the same one is used for both the matrix element and parton shower generators; if two are shown, the first is used for the matrix element calculation and the second for the parton shower. Tune refers to the set of tuned parameters used for the underlying event. MG5_aMC refers to MadGraph5_aMC@NLO 2.2.X or 2.3.X [42]; Pythia 6 refers to version 6.427 [67]; Pythia 8 refers to version 8.2 [68]; Herwig++ refers to version 2.7 [46]; Herwig7 refers to version 7.0.4 [69]; MePs@Nlo refers to the method used in Sherpa [70–73] to match the matrix element to the parton shower. Samples using Pythia 6 or Pythia 8 have heavy flavour hadron decays modelled by EvtGen 1.2.0 [74]. All samples include leading-logarithm photon emission, either modelled by the parton shower

generator or by PHOTOS [75]. The masses of the top quark and SM Higgs boson are set to 172.5 GeV and 125 GeV, respectively.

## 4.3. Object Selection

### 4.3.1. Primary vertices

The primary vertex in an event is chosen as the vertex with the highest $\sum p_{\mathrm{T}}^2$ of associated tracks [76].

### 4.3.2. Trigger

The single-lepton triggers and di-lepton triggers used in this analysis for 2015 - 2018 data are listed in Table 4.3. These trigger names specify the criteria that lepton candidates must satisfy in order for an event to be selected. For example, 'HLT_mu20_iloose_L1MU15' requires the presence of a muon with $p_T$ greater than or equal to 20 GeV, passing a loose isolation, and also passing the Level-1 trigger requirement of $p_T$ greater than or equal to 15 GeV. The trigger strategy is similar to the one described in the $ttH$ multilepton $80 fb^{-1}$ study [77]. A logical OR between di-lepton (DL) and single-lepton (SL) triggers are applied in this analysis. The trigger efficiencies in the simulated samples are corrected to match the measured efficiencies in the data. These corrections are applied on an event-by-event basis and depend on variables such as transverse momentum [78].

| | |
|---|---|
| | Single lepton triggers (2015) |
| $\mu$ | HLT_mu20_iloose_L1MU15, HLT_mu50 |
| $e$ | HLT_e24_lhmedium_L1EM20VH, HLT_e60_lhmedium, HLT_e120_lhloose |
| | Dilepton triggers (2015) |
| $\mu\mu$ (asymm.) | HLT_mu18_mu8noL1 |
| $ee$ (symm.) | HLT_2e12_lhloose_L12EM10VH |
| $e\mu, \mu e$ ($\sim$symm.) | HLT_e17_lhloose_mu14 |
| | Single lepton triggers (2016) |
| $\mu$ | HLT_mu26_ivarmedium, HLT_mu50 |
| $e$ | HLT_e26_lhtight_nod0_ivarloose, HLT_e60_lhmedium_nod0, HLT_e140_lhloose_nod0 |
| | Dilepton triggers (2016) |
| $\mu\mu$ (asymm.) | HLT_mu22_mu8noL1 |
| $ee$ (symm.) | HLT_2e17_lhvloose_nod0 |
| $e\mu, \mu e$ ($\sim$symm.) | HLT_e17_lhloose_nod0_mu14 |
| | Single lepton triggers (2017 / 2018) |
| $\mu$ | HLT_mu26_ivarmedium, HLT_mu50 |
| $e$ | HLT_e26_lhtight_nod0_ivarloose, HLT_e60_lhmedium_nod0, HLT_e140_lhloose_nod0 |
| | Dilepton triggers (2017 / 2018) |
| $\mu\mu$ (asymm.) | HLT_mu22_mu8noL1 |
| $ee$ (symm.) | HLT_2e24_lhvloose_nod0 |
| $e\mu, \mu e$ ($\sim$symm.) | HLT_e17_lhloose_nod0_mu14 |

Table 4.3: List of lowest $p_T$-threshold, single lepton and di-lepton triggers used for 2015-2018 data taking.

### 4.3.3. Leptons

Two sets of light lepton requirements are defined for final state, namely as 'Loose' (L) and 'Tight' (T) as shown in Table 4.4. These requirements help to select and classify leptons

based on their properties, such as the quality of their reconstruction, energy deposits, and isolation. The Loose and Tight criteria are commonly used to define different levels of lepton identification efficiency and purity, with Tight being a stricter selection compared to Loose. Loose selection aim to achieve a higher efficiency in identifying leptons, allowing for a larger number of leptons to be included in the analysis and have looser requirements on variables such as track quality, energy deposits in the calorimeters, and isolation from other particles. Tight selection aims to ensure a higher level of confidence in the identification of leptons, at the cost of a lower efficiency compared to the Loose selection. The meaning of the different cuts in the Table 4.4 will be described in the next sections.

| | $e$ | | $\mu$ | |
|---|---|---|---|---|
| | L | T | L | T |
| Isolation | PLVLoose | PLVTight | PLVLoose | PLVTight |
| Identification | LooseLH | TightLH | Loose | Medium |
| Charge MisID BDT | Yes | | N/A | |
| Ambiguity type | Yes | | N/A | |
| $\lvert d_0\rvert/\sigma_{d_0}$ | $< 5$ | | $< 3$ | |
| $\lvert z_0 \sin\theta\rvert$ | $< 0.5$ mm | | | |

Table 4.4: Loose and Tight definitions of light leptons.

#### *4.3.3.1. Electrons*

Electrons are reconstructed by matching the energy deposits from the EM calorimeter to the track in the inner detector. They are required to have $p_T > 4.5$ GeV and $|\eta| < 2.5$, the electron within the transition region between barrel and end cap electromagnetic calorimeter, $1.37 < |\eta| < 1.52$ are vetoed. To reduce the non-prompt electron contribution, cuts on the $d_0$ and $z_0$ are applied to ensure that the electron originates from a primary vertex. A likelihood-based identification at the 'Loose' operation point is used for Loose electrons and

'Tight' operation point is used for Tight electrons.

They are required to be isolated from other objects in the event by passing the lepton isolation PromptLeptonVeto working point (PLVLoose) [79] for Loose electrons and PLVTight for Tight electrons. In addition, electrons candidates should pass a charge misidentification BDT working point to reduce charge flip background contribution(QmisID). This analysis takes into account the contribution from photon conversion background, which can arise from photons being misidentified as electrons. To suppress this background, electron candidates are required to fulfill an ambiguity bit selection. The ambiguity bit is a binary variable that indicates whether an electron candidate is associated with any additional tracks besides the primary track. In the case of a photon conversion background, the ambiguity bit is expected to be non-zero since it represents the presence of multiple tracks associated with a single electromagnetic cluster. To suppress this background, the ambiguity bit selection requires the ambiguity bit to be only 0 [77].

#### *4.3.3.2. Muons*

Muons are reconstructed by using the information of Muon spectrometer and the Inner detector. Muon candidates are selected with $p_T > 3$ GeV and $|\eta| < 2.5$. They are required to pass the Loose and Medium identification working point for Loose muons and Tight muons respectively. The impact parameter cut remains the same as the electron but transverse impact parameter significance requires less than 3 . The Loose muons have to satisfy PLVLoose and Tight muons must be selected from PLVTight.

#### 4.3.4. Hadronically Decaying Taus

Hadronically decaying tau lepton candidates ($\tau_{\text{had}}$) are reconstructed from clusters in the calorimeters and associated inner detector tracks. The candidates are required to have either one or three associated tracks, with a total charge of $\pm 1$. Candidates with $p_{\text{T}} > 20$ GeV and $|\eta| < 2.5$, excluding the electromagnetic calorimeter transition region, are considered. A RNN discriminant using calorimeter and tracking-based variables is used to identify $\tau_{\text{had}}$ candidates and reject generic jet backgrounds. The chosen working point used in this analysis has an efficiency of 75% (60%) for one (three) prong $\tau_{\text{had}}$ decays. In order to ensure that this channel is orthogonal to other, events with $\tau_{\text{had}}$ candidates are rejected.

#### 4.3.5. Jets and b-jets

The jets used in this analysis are reconstructed by the anti-$k_{\text{T}}$ algorithm with radius parameter $R = 0.4$ from the particle-flow (PFlow) objects. The particle-flow algorithm provides a list of tracks and a list of topoclusters containing both the unmodified topoclusters and a set of new topoclusters resulting from the energy subtraction procedure. The algorithm attempts to match each track to a single topocluster in the calorimeter. The expected energy deposited in the calorimeter (based on topocluster position and the track momentum) is subtracted cell by cell from the set of matched topoclusters. If the remaining energy is consistent with the expected shower fluctuations of a single particle's signal, the topocluster remnants are removed [80].

Events are required to pass the LooseBad working point recommended by Jet-$E_T^{miss}$ group for jet cleaning. Jet cleaning is a procedure applied to identify and remove jets that may be contaminated by non-collision backgrounds or instrumental noise. The Jet Vertex Tagger (JVT) is applied to reduce the effect of pileup background with $p_T < 60$ GeV and

$|\eta < 2.4|$ jet. The chosen working point(WP) for the JVT is Tight, its associated scale factor is applied to MC event weight. The jet selection used for this analysis is:

- $p_{\mathrm{T}} > 25$ GeV.
- anti-kt R = 0.4.
- $|\eta| < 2.5$.
- JVT WP: Tight
- Jet cleaning WP: LooseBad

The flavor tagging algorithm used to determine the flavor of the jet is a high level algorithm based on a deep neural network(DL1r) that uses the output of 'recurrent neural network impact parameter' (RNNIP) as input. DL1r output has three different probabilities ($p_b$, $p_c$ and $p_u$) that are combined to define a final discriminant. DL1r algorithm has been re-optimized in 2019 in order to maximize the performance on the jet collections recommended for use in ATLAS, and to extend the algorithm performance to very high jet $p_{\mathrm{T}}$ [81], [82]. The $b$-tagging working point with a 77% efficiency is chosen, in order to keep orthogonality to other diHiggs analyses. Such efficiency is measured from $t\bar{t}$ MC samples and dedicated $t\bar{t}$ data. The associated SFs are taken into account in MC weight calculation. In order to ensure that this channel is orthogonal to others, events with b-jets candidates are rejected.

#### 4.3.6. Missing Energy

Missing transverse momentum $E_T^{miss}$ is used to define certain additional selections for validation of background modeling. The missing transverse momentum vector is defined as minus the vector sum of the transverse momenta of all reconstructed and calibrated physics

objects and remaining unclustered energy, the latter of which is estimated from low $p_{\mathrm{T}}$ tracks associated with the primary vertex but not assigned to a hard object [83]. The value of $E_T^{miss}$ for an event is the magnitude of this vector.

#### 4.3.7. Overlap Removal

Since objects are reconstructed with different algorithms in parallel, i.e. no check to see if the same set of clusters or tracks are used for reconstructing two different objects, one needs to implement a set of rules to remove objects close to each other to avoid double counting. The overlap removal procedure is applied when the analysis data (DxAOD) is produced. The optimal overlap removal procedure is detailed below:

- Any Loose muon found to share a track with a Loose electron is removed.
- Any Loose electron found to share a track with a Loose muon is removed.
- Any jet found within a $\Delta$R of 0.2 of a Loose electron is removed.
- Any Loose electron subsequently found within $\Delta$R of of 0.4 of a jet is removed.
- Any jet with less than 3 tracks associated to it found within $\Delta$R of 0.2 of a Loose muon is removed.
- Any Loose muon subsequently found within $\Delta$R of 0.4 of a jet is removed.

### 4.4. Event Selection

To target $3\ell 0\tau_h$ final state, events are required to pass the following common selection:

- **Trigger**:
  - Global Trigger Decision [78].
  - Single lepton triggers or di-lepton triggers.
- **Lepton Multiplicity**:
  - Exactly three leptons with a total electric charge of $\pm 1$.
  - Events are classified by their lepton flavour/charge composition as $l_0$, $l_1$ and $l_2$, where the lepton with opposite charge with respect to the other two is noted as lepton index 0 ($l_0$). The remaining lepton that is nearest to $l_0$ in $\Delta R$ is given the index $1(l_1)$ and the final lepton is noted as lepton $2(l_2)$.
  - $p_T^0 > 10\ GeV$ and $p_T^{1,2} > 15\ GeV$.
  - $l_0$ is required to pass the loose selection while $l_1$ and $l_2$ are required to pass the tight selection. The definition of loose and tight selection are shown in Table 4.4.
- **Hadronic Tau Veto**: Events with at least one hadronic tau are vetoed.
- **Jet Multiplicity**: Events with at least one jet are selected: $N_{jet} \geq 1$.
- **b-jet Veto**: Events with any $b$-tagged jets are vetoed.
- **Low Mass Veto**:
  - To remove leptons from quarkonium decays, events with at least one same-flavour opposite-sign (SFOS) lepton pair with an invariant mass less than 12 GeV are vetoed.
- **$Z$-Mass Veto**:
  - Events with SFOS lepton pair with an invariant mass within $\pm 10$ GeV window around $m_Z$ (91.2 GeV) are vetoed. This requirement helps to reduce di-boson background.

– To remove potential backgrounds with Z decays to $ll\gamma^* \to lll'l'$ where one lepton has very low momentum and is not reconstructed, invariant mass of the tri-lepton within ±10 GeV window around $m_Z$ are vetoed: $|m_{lll} - m_Z|$> 10 GeV

### 4.5. Background Estimation

After pre-selection, the background sources can be classified into two categories, irreducible background and reducible background. Irreducible backgrounds are events with the same number of prompt leptons as HH signal. The reducible background contains events where at least one of the candidate leptons is not prompt (including QmisID leptons and the objects which are incorrectly identified as leptons i.e fake leptons). In the irreducible background category, the prompt leptons are mainly from WZ, VV (di-boson backgrounds other than WZ), VVV, tV, ttV, VH, $t\bar{t}$H, $t\bar{t}t\bar{t}$, $t\bar{t}$WW, $t\bar{t}$t and WtZ where V stands for W or Z bosons. The prompt processes are predicted by MC simulation and dedicated control region for WZ is created to check the modeling of the MC simulation and find the normalization. The reducible backgrounds mainly come from $t\bar{t}$, V+jets and $V\gamma$ production. Reducible background processes are not modeled well in simulation and dedicated data-driven techniques are used as described in section 4.8. The method relies on defining several control regions enriched in particular sources of fake leptons: internal conversion, material conversion electrons and heavy flavor leptons (B or C decay). The method uses a template fit to determine the normalization of each source of background.

Figure 4.1 shows the plot of invariant mass of $l_0l_1l_2$ after preselection. The blue dotted line represents the HH signal, which is normalized to the total area of background. In the plot, 'Other' represent the collection of all prompt backgrounds except WZ.

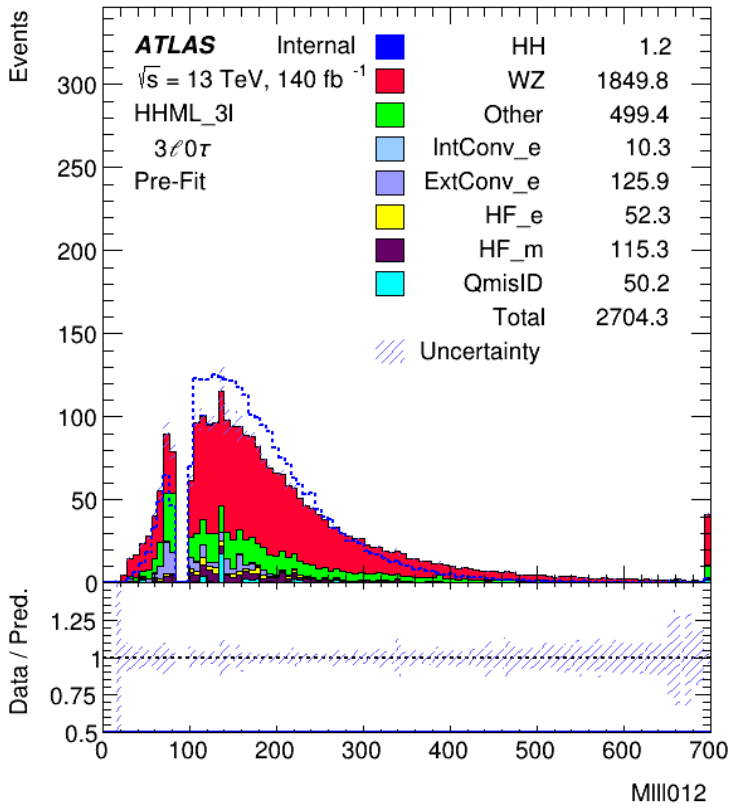


Figure 4.1: Invariant Mass of $l_0 l_1 l_2$ after preselection. The blue dotted line represents the HH signal, which is normalized to the total area of background.

A high energy photon can convert to the pair of electron-positron and sometime those electron/positron can be selected as an electron/positron of the event. 'IntConv_e' represents electrons originating from internal conversions, which are primarily a result of quantum electrodynamics (QED) processes. In this case, a high-energy photon interacts with the electromagnetic field of an atomic nucleus or an atomic electron, leading to the production of an electron-positron pair. 'ExtConv_e' on the other hand, represents electrons originating from external conversions, which occur when a high-energy photon interacts with the material of the detector itself. The photon may undergo scattering or interactions with the detector material, resulting in the production of an electron-positron pair. Events with 'IntConv_e' electrons have a very small contribution to the signal region and a dedicated control region

is not defined for this source of background.

'HF_e' and 'HF_m' are the backgrounds containing electrons and muons respectively coming from heavy flavor hadron decay. 'QmisID' represents the events with at-least one charge mis-identified electron. Events with 'QmisID' electrons have a very small contribution to the signal region and a dedicated control region is not defined for this source of background. The signal events are very small therefore this analysis is statistically limited.

### 4.6. Control Regions

In order to correctly estimate the non-prompt backgrounds and the dominant WZ background, four dedicated control regions (CR) have been chosen. All control regions are orthogonal to each other and also orthogonal to signal region. All four control regions are required to pass the following basic selections:

- Global Trigger Decision [78].
- Single lepton triggers or di-lepton triggers.
- Exactly 3 leptons with a total electric charge of $\pm 1$.
- $p_T^{l_0} > 10$ GeV and $p_T^{l_1,l_2} > 15$ GeV.
- Events with at least one hadronic tau are vetoed.
- Events with at least one SFOS lepton pair with an invariant mass less than 12 GeV are vetoed.

After these basic selections, other different selection are applied as follows:

#### 4.6.1. WZ Control Region

- Loose Isolation for $l_0$ and Tight Isolation for $l_1/l_2$.
- Veto events if they contain any b-tagged jets.
- $N_{jet} \geq 1$.
- Events with at least one SFOS lepton pair with an invariant mass within a $\pm 10$ GeV window around $m_Z$ are chosen. This cut guarantees orthogonality with the signal region.
- $|m_{l_0 l_1 l_2} - m_Z| > 10$ GeV
- $MET > 30$ GeV

#### 4.6.2. HF_e/HF_m Control Region

Electrons and Muons coming from heavy flavor decay basically originate from $t\bar{t}$ events in this analysis.

- $N_{jet} \geq 1$.
- $N_{bjet} \geq 1$. This cut guarantees orthogonality with the signal region.
- Events with at least one SFOS lepton pair with an invariant mass within a $\pm 10$ GeV window around $m_Z$ are vetoed.
- $|m_{l_0 l_1 l_2} - m_Z| > 10$ GeV.
- $l_1$ and $l_2$ must be electron for HF_e control region.
- $l_1$ and $l_2$ must be muon for HF_m control region.

#### 4.6.3. ExtConv_e Control Region

Material Conversion basically originate from $V\gamma$ and Z+jets events.

- $N_{jet} \geq 1$.
- Loose Isolation for $l_0$ and Tight Isolation for $l_1/l_2$.
- Veto events if they contain any b-tagged jets.
- $|m_{l_0 l_1 l_2} - 91.2| < 10$ GeV. This cut guarantees orthogonality with the signal region.
- For $l_1/l_2$: a conversion vertex (CV) is found with radius $r > 20$mm, and the mass of the vertex is $0 <$ m(trk-trk) at CV $< 100$MeV.

Where m(trk-trk) is the invariant mass of the track associated to the electron and its closest track (originating from the conversion) calculated at conversion vertex.

### 4.7. Estimation of WZ Using Fitting Function

WZ is considered to be one of the most important prompt backgrounds in this analysis. There is a mis-modelling issue of WZ sample with high jet multiplicities as shown in Figure 4.2. A dedicated control region as described in 4.6.1 has been setup to derive a correction for the number of jets distribution for this process. In the WZ control region, the ratio of the WZ contribution to the data (subtracted by the non-WZ backgrounds) is fitted with a polynomial [84] of the form:

$$f(x) = \frac{b \times 2^c - a}{2^c - 1} + \frac{(b-a) \times 2^c}{(2^c - 1)x^c} \tag{4.1}$$

Where x represents the jet multiplicity. A least chi squared fit to the polynomial gives the parameters:

- $a = -0.706 \pm 0.018$
- $b = -0.553 \pm 0.017$
- $c = 0.279 \pm 0.026$

While in the fitting, events with number of jets (nJets) $> 4$ have been treated as nJets $= 4$ events. The nJets distribution plots before and after fit are in Figure 4.2.

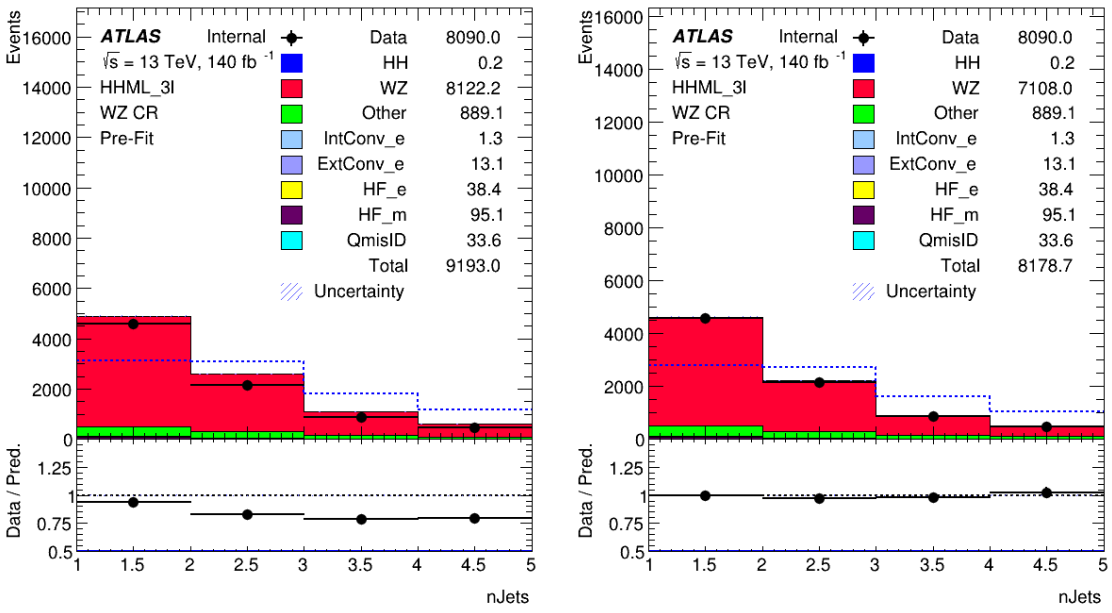


Figure 4.2: The pre-fit (let) and post-fit (right) nJets distribution plots of the WZ control regions, using fitting function of Equation 4.1.

## 4.8. Template Fit Method

Since the non-prompt light lepton backgrounds is a mixture of leptons from semi-leptonic heavy-flavor (HF) decays and photon conversions as shown in Figure 4.3, a template method has been developed to estimate these backgrounds.

Within the template fit method, the normalization of the different 'fakes' contribution templates, as given by the MC of all processes contributing to non-prompt lepton back-

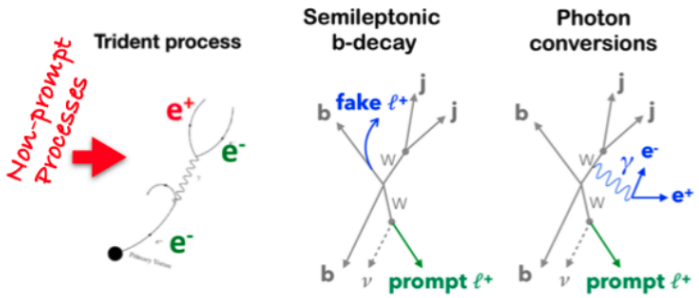


Figure 4.3: Leptons from semi-leptonic heavy-flavor (HF) decays and photon conversions.

ground, are left free-floating in a fit to data, and these normalization factors(NFs) are used to correct the fakes MC estimates. The template fit method is a semi-data-driven method, i.e. it relies on the truth information from $t\bar{t}$, $Z+jets$, $W+jets$, $V\gamma$ and single top MC simulation to define different types of fake/non-prompt leptons, and on the general description of fakes kinematics by MC.

The main contribution to non-prompt lepton background comes from $t\bar{t}$, $V\gamma$ and $V+jets$. Based on the truth classification of events containing a non-prompt lepton, following main contributions are distinguished, and free-floating normalization factor is assigned to each of them:

- $NF_e^{HF}$: normalization factor applied to events with one non-prompt electron from B decay, C decay or light hadron (dominated by B decay).
- $NF_\mu^{HF}$: normalization factor applied to events with one non-prompt muon from B decay, C decay or light hadron (dominated by B decay).
- $NF_e^{ExtConv}$: normalization factor applied to events with one fake electron from photon conversion due to interactions with detector material (Material Conversion).

The classification of MC samples in the aforementioned categories is based on their truth origin.

MC events containing a charge-flip electron are vetoed, since they are grouped as separate QmisID background. The vetoed events are those containing either a charge flipped isolated electron, or a background electron with opposite charge compared to the prompt mother electron.

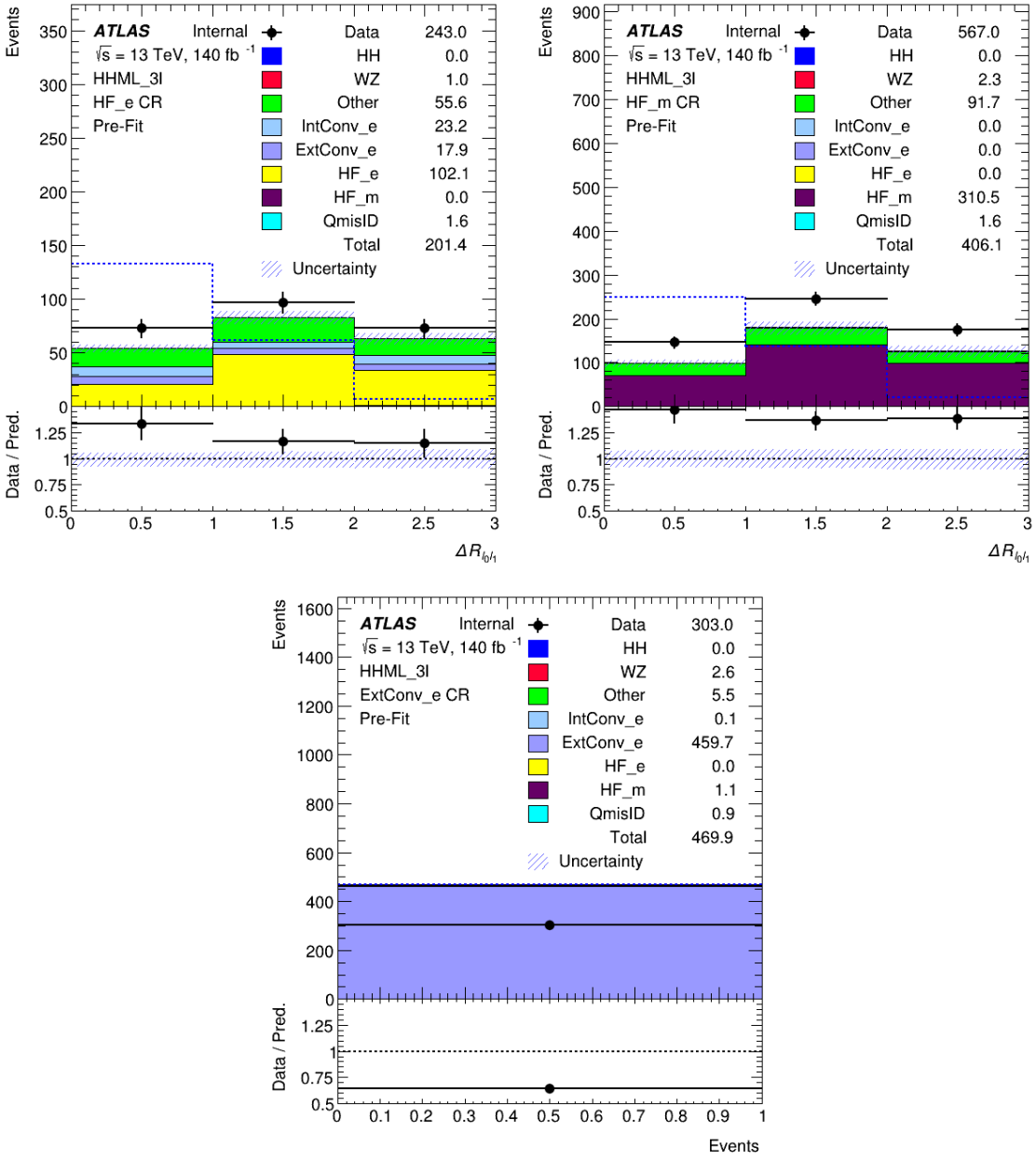


Figure 4.4: Top left /right shows pre-fit plots of the HF_e/ HF_m control regions. Bottom shows pre-fit plot of Material Conversion control region.

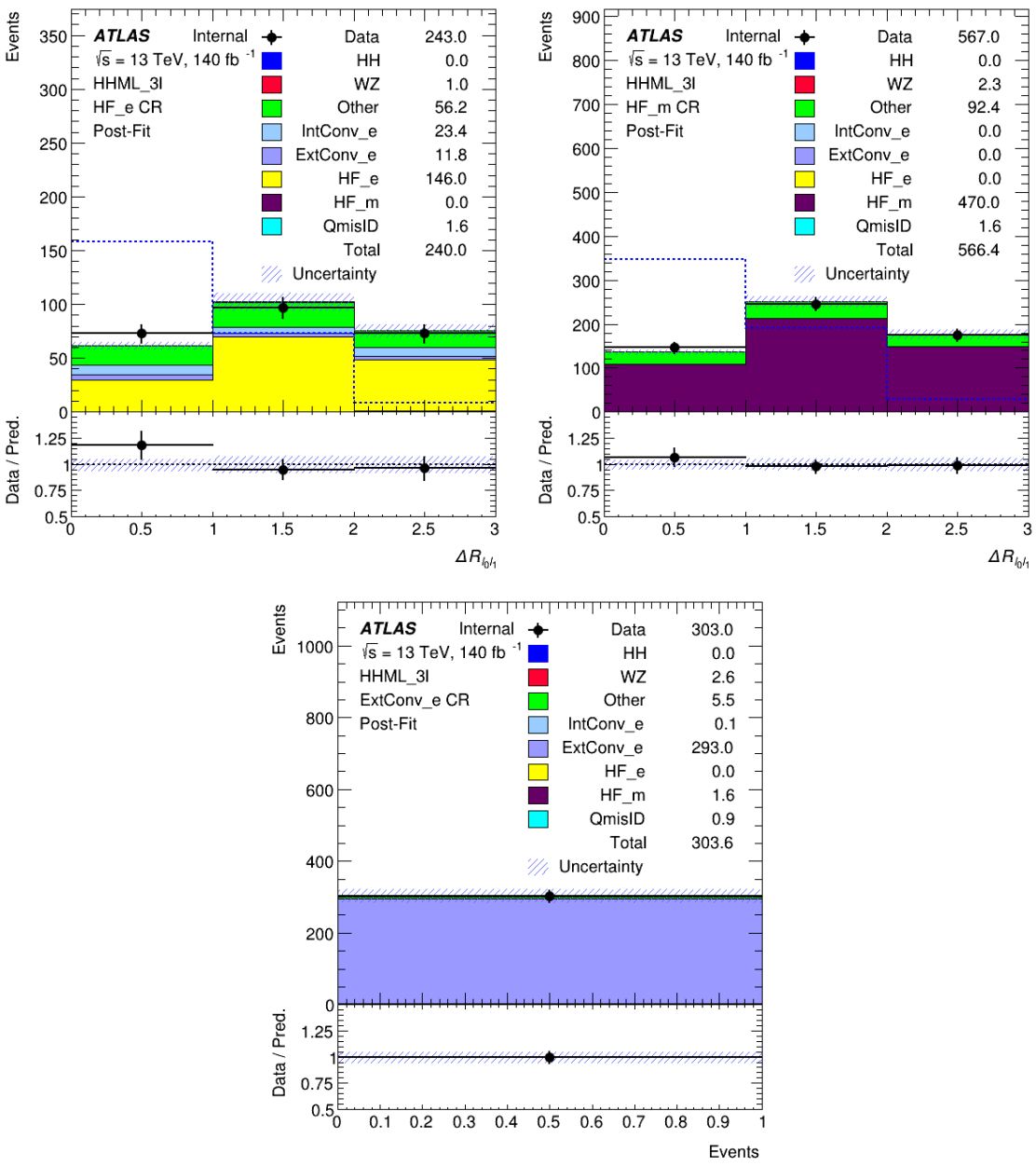


Figure 4.5: Top left /right shows post-fit plots of the HF_e/ HF_m control regions. Bottom shows post-fit plot of Material Conversion control region.

Blinding is a technique employed in this analysis, to prevent biases or unconscious influence i.e, observed data from the signal region is excluded. It helps ensure that the analysis is carried out objectively, without being influenced by preliminary observations or expectations. While the analysis is blinded, the templates are fitted to the data using control

regions only. At this stage, the NFs extracted from the blinded fit and inserted into the full fit model in order to obtain the expected analysis sensitivity from Asimov data set, which is a simulated dataset constructed based on the expected signal and background contributions. After unblinding the normalization factors are derived in one simultaneous fit including the signal region.

The following distributions are exploited to best discriminate among the NFs in the simultaneous template fit:

- $\Delta R_{l_0 l_1}$ in $lee$ channel, to estimate $NF_e^{\mathrm{HF}}$ (3 bins, $0 <= \Delta R_{l_0 l_1} <= 3$)
- $\Delta R_{l_0 l_1}$ in $l\mu\mu$ channel, to estimate $NF_\mu^{\mathrm{HF}}$ (3 bins, $0 <= \Delta R_{l_0 l_1} <= 3$)
- Number of events to estimate $NF_e^{\mathrm{ExtConv}}$ (1 bin)

The three control regions are shown on Figures 4.4 and 4.5 prior and after the fit to data while the measured NFs are shown on Figure 4.6. Figure 4.7 shows the pre-fit and post-fit summary in different control regions. There is a good Data/MC agreement in post-fit plots.

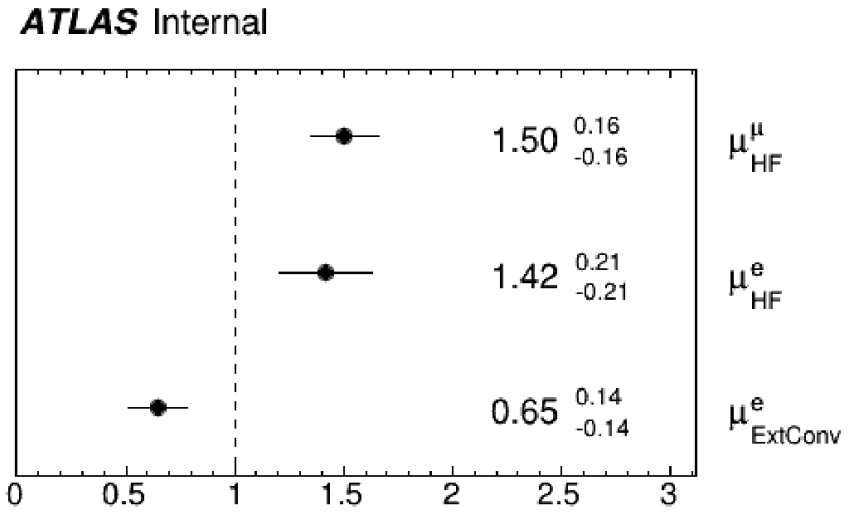


Figure 4.6: Normalization factors obtained after the fit to data using the CR.

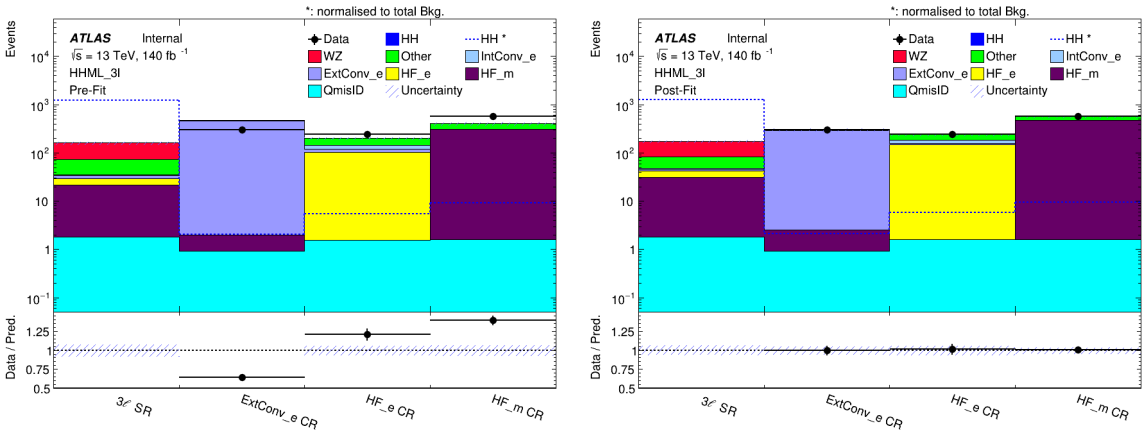


Figure 4.7: Pre-Fit and Post-Fit Summary in different control regions.

## 4.9. Multivariate Analysis Strategy

After filtering out events using the selections described in section 4.4, a multivariate discriminant has been developed using the TMVA framework (Root 6.18/00 [85]) with the Boosted Decision Tree (BDT) method to separate signal from backgrounds. It is based in Gradient Boosted Decision Trees (BDTG) [86]. BDTG use both ggF and VBF $HH$ signal samples and is trained against all background.

The purpose of the BDTG is to separate the signal events from the background events based on a set of selected variables. These variables, summarized in Table 4.5, are chosen to be the most discriminating variables in the BDTG training. They are carefully selected to provide the highest discriminating power between signal and background events. To understand the interdependencies between these variables, a correlation matrix is constructed and presented in Figure 4.8. The correlation matrix quantifies the linear correlation between pairs of variables.

| Variable | Description |
|---|---|
| $\Delta R_{l_0 l_1}$ | Distance in $\eta - \phi$ space between lepton 0 and lepton 1 |
| $m_{l_0 l_1}$ | Invariant mass of lepton 0 and lepton 1 |
| min. $m_{ll}^{\mathrm{OS}}$ | Minimum invariant mass of opposite-sign lepton pairs |
| $\Delta R_{l_2 j}$ | Distance in $\eta - \phi$ space between lepton 2 and nearest jet |
| $\Delta R_{l_1 l_2}$ | Distance in $\eta - \phi$ space between lepton 1 and lepton 2 |
| min. $m_{ll}^{\mathrm{OSSF}}$ | Minimum invariant mass of opposite-sign same-flavor lepton pairs |
| $m_{ll}^{Z-matched}$ | Invariant mass of lepton pair closest to $Z$ mass |
| $m_{lljj}$ | Invariant mass of all three leptons and two leading jets |
| $m_{lll}$ | Invariant mass of all three leptons |
| $m_{l_2 j}$ | Invariant mass of lepton 2 and nearest jet |
| $m_{l_0 l_2}$ | Invariant mass of lepton 0 and lepton 2 |
| MET | Missing transverse energy |
| $\Delta R_{l_0 j}$ | Distance in $\eta - \phi$ space between lepton 0 and nearest jet |
| FlavorCategory | Categorization of lepton flavors (eem, emm, ...) |
| $HT_{\mathrm{lep}}$ | Scalar sum of lepton $p_T$'s and missing transverse momentum |
| HT | Scalar sum of jet $p_T$'s |
| $\Delta R_{l_1 j}$ | Distance in $\eta - \phi$ space between lepton 1 and nearest jet |
| $\Delta R_{l_0 l_2}$ | Distance in $\eta - \phi$ space between lepton 0 and lepton 2 |
| $m_{l_1 j}$ | Invariant mass of lepton 1 and nearest jet |
| $HT_{\mathrm{jets}}$ | Scalar sum of jet $p_T$'s |
| $m_{l_0 j}$ | Invariant mass of lepton 0 and nearest jet |
| $m_{l_1 l_2}$ | Invariant mass of lepton 1 and lepton 2 |

Table 4.5: Variables used in BDTG training.

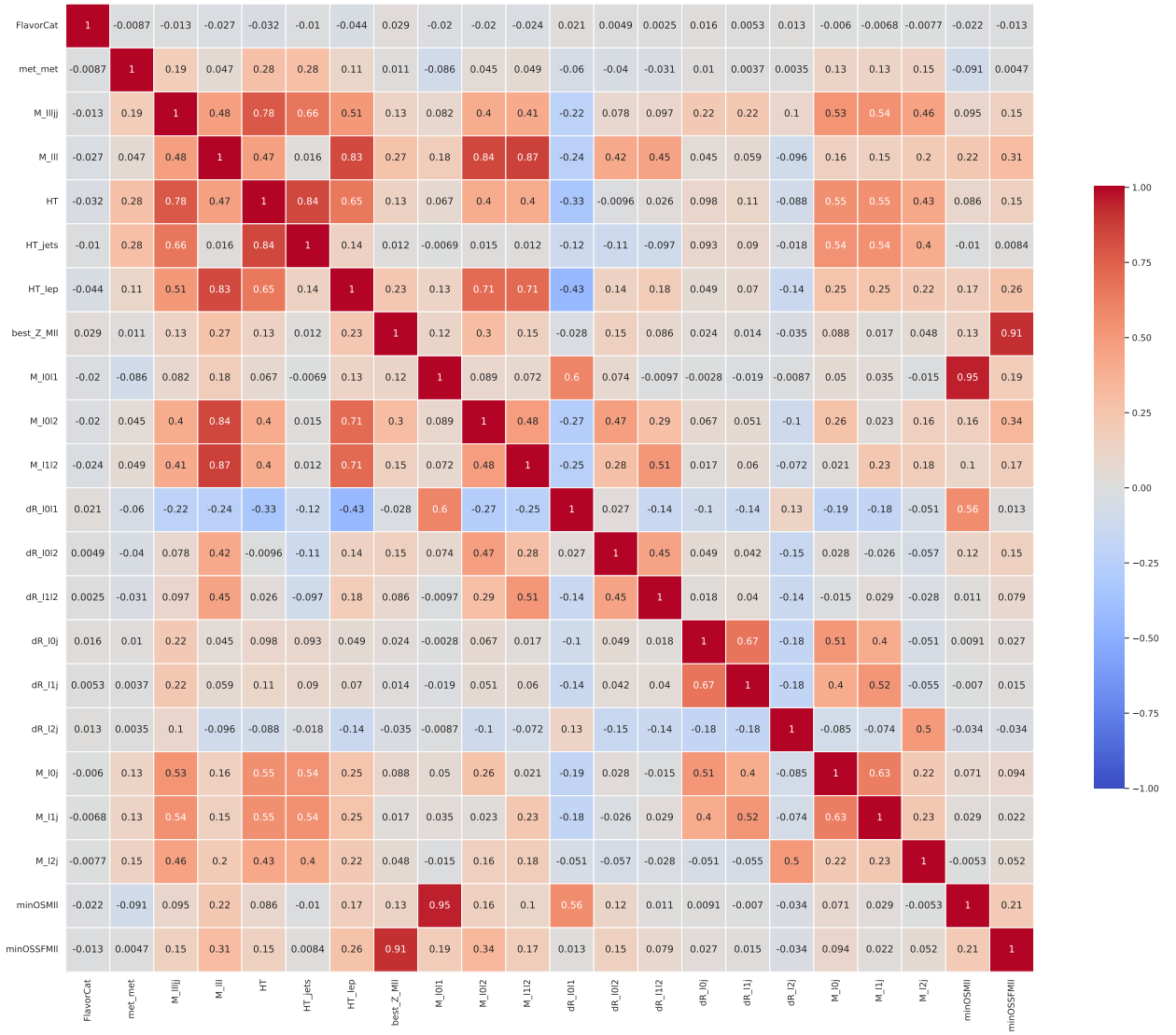


Figure 4.8: The correlation matrix of variables used in BDTG training for signal samples.

### 4.9.1. 3-fold Cross Validation

The statistics of MC training samples are limited. In the 3-fold cross-validation (3-CV) technique [87] used in this analysis, the limited statistics of the MC training samples are maximized by dividing the samples into three folds or subsets. This allows for the use of the full samples while ensuring the orthogonality of training and application. In each iteration of

the 3-CV, two folds (two-thirds of the samples) are used for training and testing the model, while the remaining fold (one-third of the samples) is kept for application. This ensures that the training and testing processes utilize different subsets of the data, preventing overfitting and providing a more reliable evaluation of the model's performance. The splitting of the folds is based on event numbers, ensuring a random and representative distribution of events across the folds. Each fold is treated as an independent training and testing set, and the training method remains the same for each fold.

For the BDTG, the training parameters are optimized using hyper-parameter optimization techniques. The optimization is performed by maximizing the area under the receiver operating characteristic (ROC) curve of the testing set. The ROC curve is a graphical representation of the trade-off between the true positive rate and the false positive rate of the classifier. The discriminant output represents the BDTG score assigned to each event, indicating the likelihood of being signal-like or background-like. The discriminant output for fold-1 and the ROC curve are shown in Figure 4.9.

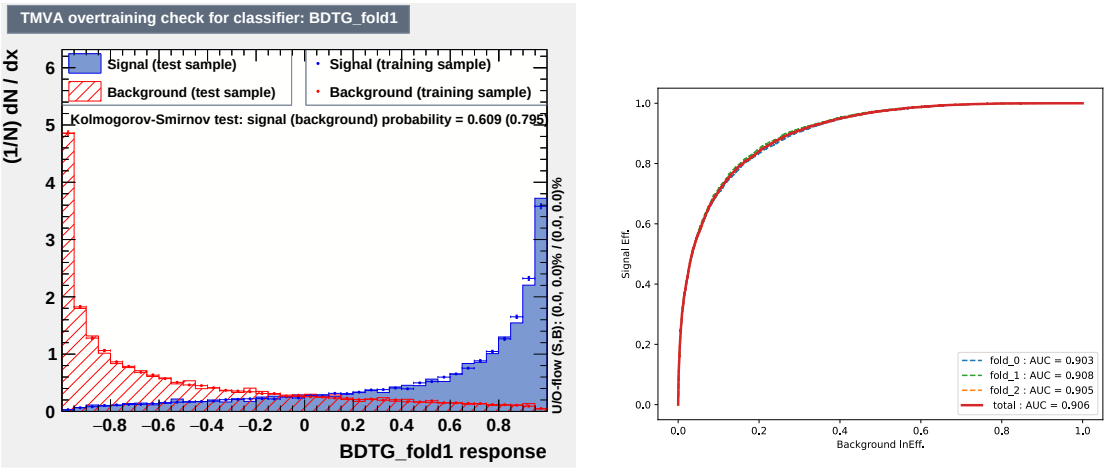


Figure 4.9: Discriminant output for fold-1 (left) and ROC curve (right) from the BDTG training.

## 4.10. Signal Region

The signal region is defined by requiring that the bdtg score $> 0.55$, in addition to the preselection described in Section 4.4. Figure 4.10 shows the bdtg output variable in the signal region.

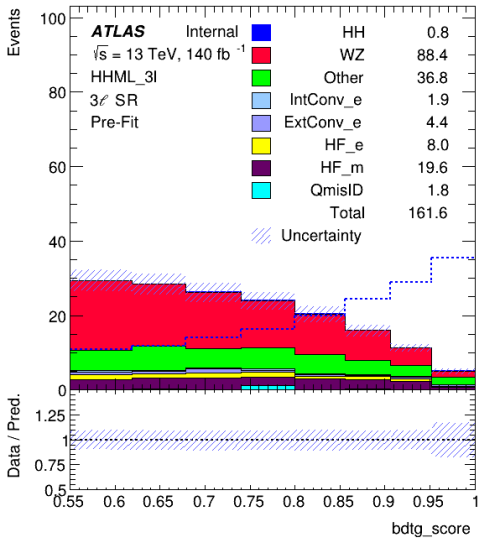


Figure 4.10: BDTG output in the signal region for bdtg $> 0.55$. The blue dotted line represents the HH signal, which is normalized to the total area of background.

## 4.11. Systematic Uncertainties

The uncertainties in this analysis can be broken down into statistical uncertainties, and systematic uncertainties.The statistical uncertainty is the uncertainty that arises from analyzing data from a limited pool. Also, MC statistical uncertainties account for the limited size of the MC samples used in the analysis and provide an estimation of the uncertainty associated with the simulation-based predictions. Due to computational constraints, it is not possible to simulate an infinite number of events. As a result, the simulated samples have a finite size, leading to statistical fluctuations in the simulated event yields. In high energy physics, histograms are commonly used to describe the distribution of a variable by dividing it into a set of finite-width bins and calculating the fraction of events falling into each bin.

As the total number of events is finite, the number of events in each bin follows a Poisson distribution. To determine the uncertainty of each bin, the square root of the number of events in the bin is calculated.

In contrast to statistical uncertainties, systematic uncertainties arise from limitations in the techniques used or in the model being used for analysis. To deal with systematic uncertainties, nuisance parameters are introduced, each with an upward and downward variation. These nuisance parameters can represent a single uncertainty, a component of an uncertainty, or a combination of related and partially correlated uncertainties.

#### 4.11.1. Experimental Uncertainties

- **Luminosity:** The uncertainty of the combined Run-2 dataset is 1.7%. It is derived, following a methodology similar to that detailed in [88], from a preliminary calibration of the luminosity scale using x-y beam-separation scans performed from 2015 to 2018.
- **Pileup:** The pileup reweighing procedure is based on the comparing the average number of interactions per $pp$ collision ($< \mu >$) in data to the corresponding simulated samples. The uncertainty on this method is obtained by varying the scaling factor in data.
- **Trigger:** Uncertainty on the efficiency of the electron and muon trigger selection are taken into account by using the related trigger scale factor as described in a general page [89]. SLT or DLT strategy is used and the corresponding scale factor is applied.
- **Muons:** As described by Muon Combined Performance group, the uncertainties on efficiency, energy scale, resolution, object reconstruction, identification and isolation are taken into account.

- **Electrons:** Similar to muons, the resolution, scale, efficiency uncertainties provided by Egamma Combination and Performance group is considered.

- **Jets:** Jets are reconstructed from energy deposits forming topological clusters of calorimeter cells, using the anti-kt algorithm with radius parameter R=0.4. The jet energy scale (JES) [54] calibration consists of several consecutive stages derived from a combination of MC-based methods. The Jet energy resolution (JER) uncertainties is also considered [90].

- **Flavour Tagging:** A b-jet veto is applied at 77% tagging efficiency to be orthogonal with other $HH$ analysis. The uncertainties arise from the efficiency of the tagger to select jets containing a true b-hadron, charmed hadron, light hadrons or coming from hadronically-decaying taus. The corresponding scale factors can be retrieved by the BtaggingEfficiencyTool and its getScaleFactor method.

- **Missing Transverse Momentum:** The systematic variation is respect to the scale, parallel resolution, and perpendicular resolution of the soft term $E_T^{\text{miss}}$.

#### 4.11.2. Theory Uncertainties

The sources of theory uncertainties are summarized in this sub-section, for both signal and background. The list of uncertainties can be found in Table 4.6.

**ggF HH:** Inclusive ggF cross sections for Higgs boson pair production are reported in [91] for $m_H = 125$ GeV with the central scale $\mu_0 = \mu_R = \mu_F = M_{HH}/2$. The uncertainties scheme to be considered are PDF, $\alpha_s$ (combined 'PDF + $\alpha_s$ unc'), scale and $m_{top}$ (combined 'Scale + mtop unc'), as recommended by LHC-HH group [92]. The value are listed in Table 4.6.

**VBF HH:** The value of cross section uncertainties is from LHCHXSWGHH recommendation [92].

**ttH:** Cross sections are calculated at NLO (Next-to-Leading Order) QCD (Quantum Chromodynamics) and NLO EW (Electroweak) accuracies, the corresponded uncertainties in QCD scale and PDF are taken from CERN Report4 [93].

**VV:** The uncertainties scheme to be considered are PDF, $\alpha_s$ (combined 'PDF + $\alpha_s$ unc').

**ttV:** The corresponded uncertainties in QCD scale and PDF are taken from [94].

**Other Rare Backgrounds:** For other rare processes(making less than 5% of total background events), overall 50% normalization uncertainty is assigned.

| Process | X-section [%] |
|---|---|
| HH signal | QCD Scale:$^{+2.1}_{-4.9}$, PDF(+$\alpha_S$): $^{+3}_{-3}$, $m_{top}$ :$^{+4}_{-18}$ |
| $t\bar{t}H$ | QCD Scale:$^{+5.8}_{-9.2}$, PDF(+$\alpha_S$): $^{+3.6}_{-3.6}$ |
| $t\bar{t}Z$ | QCD Scale:$^{+9.6}_{-11.3}$, PDF:$^{+4}_{-4}$ |
| $t\bar{t}W$ | QCD Scale:$^{+12.9}_{-11.5}$, PDF:$^{+3.4}_{-3.4}$ |

Table 4.6: Summary of theoretical uncertainties for the MC predictions of different processes.

### 4.11.3. Template Fit Systematics

Since the Template Fit (TF) is relying on MC, modeling uncertainties on heavy flavor and conversion fakes should be included. The systematic uncertainty on the fake (non-prompt) lepton background can be estimated as the shape difference between MC-based fake template and fakes in data, which can be defined as residual from selected data events minus all non-fake background events estimated from MC. The region definition to derive the uncertainties are provided by relaxing isolation criteria or electron/muon definition selections for $l_1$ and $l_2$ leptons passing selection. The ratio of data fakes (after subtracting all non-fake MC background) to TF fakes will be used to derive the fake template systematic uncertainties. There are two main types of systematics associated:

- $t\bar{t}$ modelling systematics
- fakes template systematics

The $t\bar{t}$ modelling systematics follows standard top group recipes and uses samples with varied amount of radiation and scale choices. The uncertainties scheme to be considered are PDF, $\alpha_s$ (combined 'PDF + $\alpha_s$ unc'), scale and $m_{top}$ (combined 'Scale + mtop unc'), as recommended by LHC-HH group [92]. This set of systematics have a very small impact on the final results.

The systematics on the fakes templates is derived as follows. The complex tight lepton definition is split into parts which are targeting different components of the fakes – the conversions (ambiguity bin) vs heavy flavors (relaxing the cut on the Tight ID Selection on $l_1$ and $l_2$). In this way, selections with dominating fake fractions are obtained and after subtraction of remaining backgrounds compared to data. Systematics for each of the heavy flavor template component (electron/muon) is derived as re-weighting in all bins of the final fit used as one nuisance parameter in a correlated way. These shape systematics are not ranked among the most important uncertainties.

The shapes in control regions with relaxed cuts (relaxed ID cut for heavy flavor and relaxed ambiguity cut for conversion) criteria for electron (muon) template are presented on Figures 4.11. The values from the ratio$((Data - NonFakeBG)/FakeBG)$ are added to the fit as an additional systematic uncertainty for the HF fakes and Conversion fakes in particular control or signal region. The template uncertainties for HF_m, HF_e was found to be 6.8% and 1.9% respectively. For ExtConv_e, it was found to be 37%.

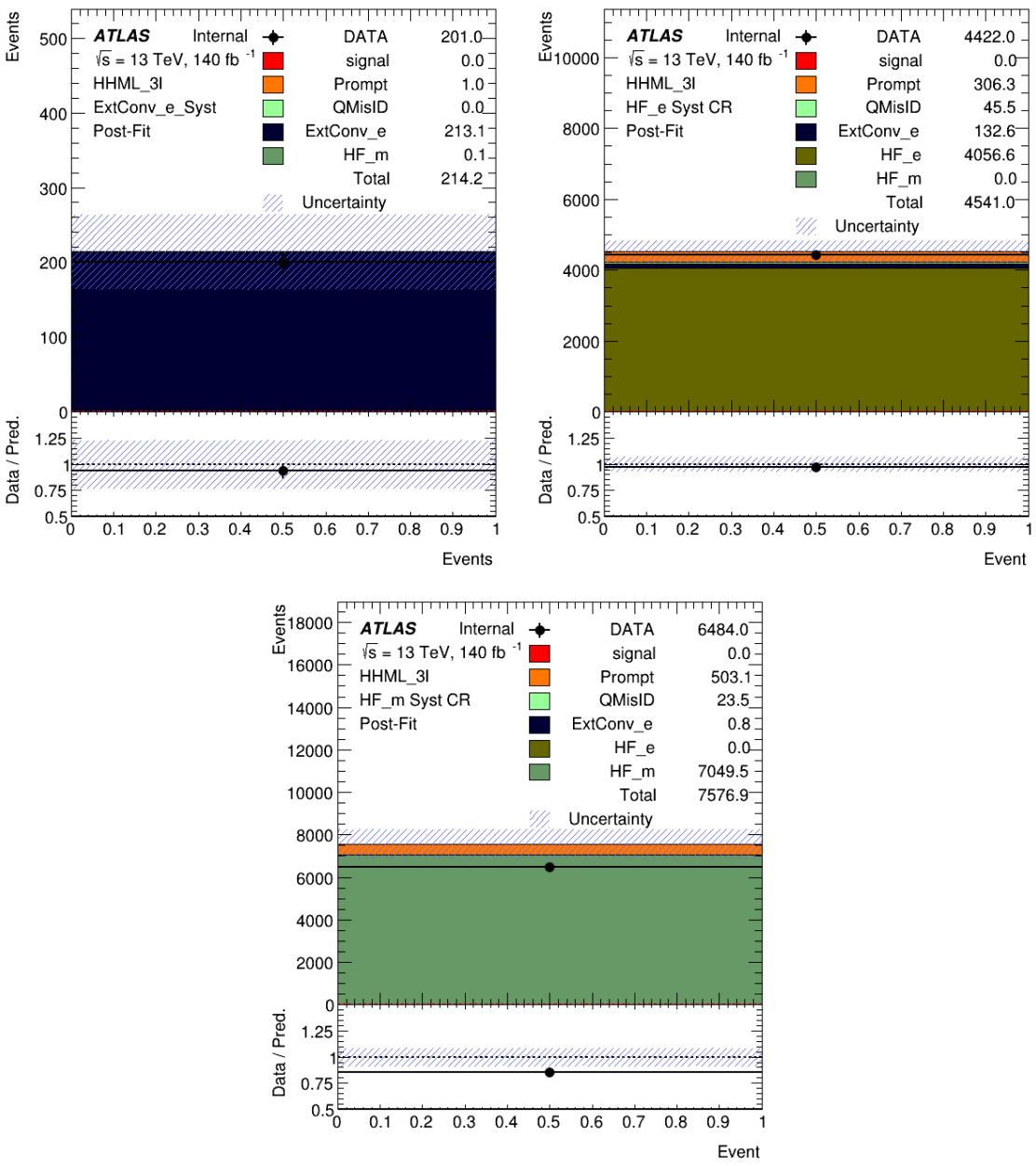


Figure 4.11: Material Conversion, HF_e and HF_m control regions with relaxed cut criteria for electron and muon templates.

## 4.12. Statistical Analysis

The statistical model is built up with a binned likelihood function. In order to obtain the cross section of $pp \to HH$ production, this likelihood fit is performed for the number

of events in the signal regions and the control regions. The fit is based on a constructed likelihood that models the expected distribution of signal and background in the data. The likelihood is parameterized by signal strength $\mu$ and nuisance parameters $\theta$, which are profiled to determine the best-fit values that maximize the likelihood. A log-likelihood ratio test statistic is then computed using the conditional likelihood, where $\mu$ is varied, and the maximum likelihood. This test statistic is used to interpret the data for hypothesis testing, such as determining the significance of observed results or setting upper limits on possible signal strengths. For a blinded analysis, the number of observed data events in the signal regions is taken from the sum of the expected MC for SM processes.

The likelihood function is constructed as the product of Poisson probability distributions in each category, c. The likelihood is constructed as follows:

$$\mathcal{L} = \prod_{c \in \text{channels}} \prod_{b \in \text{bins}} \text{Poisson}(n_{c,b}^{\text{obs}} | n_{c,b}^{S}, n_{c,b}^{B}) \times \prod_{s \in \mathbb{S}} \mathcal{G}(0|\theta_s, 1), \tag{4.2}$$

where $c$ stands for the channel index, $b$ is the bin index for each channel. The Poisson terms Poisson are given by

$$\text{Poisson}(n_{c,b}^{\text{obs}} | n_{c,b}^{S}, n_{c,b}^{B}) = \frac{1}{n_{c,b}^{\text{obs}}!} \left(\mu * n_{c,b}^{S} + n_{c,b}^{B}\right)^{n_{c,b}^{\text{obs}}} \exp^{-\left(\mu * n_{c,b}^{S} + n_{c,b}^{B}\right)} \tag{4.3}$$

where the number of events observed in each bin is marked as $n_{c,b}^{\text{obs}}$, and the expected numbers of signal and background is the corresponded bin is $n_{c,b}^{S}$ and $n_{c,b}^{B}$ respectively. The Parameter-of-interest (POI) $\mu$ is the signal strength, which is shared among different bins and channels. To represent the nuisance parameter (NP) constraint terms, a Gaussian function, $\mathcal{G}(0|\theta_s, 1)$ is considered, where $\theta_s$ is the NP term.

### 4.12.1. Profile Likelihood Ratio Test

The likelihood ratio test is a method that can be used to evaluate how well two statistical models fit the data by comparing the likelihood ratios. The main focus is to determine the most suitable value for the parameter of interest, which is the signal strength $\mu$. We will compare two models, namely the maximum likelihood estimate $L(\hat{\mu}, \hat{\boldsymbol{\theta}})$ and the conditional maximum likelihood estimate $L(\hat{\hat{\boldsymbol{\theta}}}(\mu))$. The maximum likelihood estimate involves profiling the signal strength and nuisance parameters to obtain values of $\mu$ and $\boldsymbol{\theta}$ that maximize the overall likelihood function. These values are referred to as $\hat{\mu}$ and $\hat{\hat{\boldsymbol{\theta}}}$. On the other hand, the conditional maximum likelihood estimate fixes the value of $\mu$ and profiles $\boldsymbol{\theta}$ to find the values that maximize the likelihood function at that specific value of $\mu$. The profile likelihood ratio can then be written as:

$$\lambda(\mu) = -2 \ln \frac{\mathcal{L}(\mu, \hat{\hat{\boldsymbol{\theta}}}(\mu))}{\mathcal{L}(\hat{\mu}, \hat{\boldsymbol{\theta}})} \tag{4.4}$$

We can evaluate this ratio for various values of $\mu$ to determine the most suitable signal strength and confidence intervals. A ratio of 1 suggests that the maximum likelihood estimate and the conditional maximum likelihood estimate match well for a given value of $\mu$.

### 4.12.2. Test Statistic

To perform hypothesis testing using the likelihood ratio test, we use the profile-likelihood-ratio-based test statistic $\tilde{q}_\mu$. We can use this test statistic to calculate the p-values for a specific hypothesis. However, it is essential to note that the $\tilde{q}_\mu$ test statistic assumes that the signal strength $\mu$ is greater than zero.

$$\tilde{q}_\mu = \begin{cases} -2\ln \frac{\mathcal{L}(\mu, \hat{\hat{\boldsymbol{\theta}}}(\mu))}{\mathcal{L}(0, \hat{\hat{\boldsymbol{\theta}}}(0))} & \hat{\mu} < 0, \\ -2\ln \frac{\mathcal{L}(\mu, \hat{\hat{\boldsymbol{\theta}}}(\mu))}{\mathcal{L}(\hat{\mu}, \hat{\hat{\boldsymbol{\theta}}})} & 0 \leq \hat{\mu} \leq \mu, \\ 0 & \hat{\mu} > \mu. \end{cases} \tag{4.5}$$

### 4.12.3. p-values

After defining the test statistic, we can move on to hypothesis testing. In particle physics, we use hypothesis testing to determine the significance of a result or to establish limits on the signal strength. The p-value is the key factor in achieving these goals and is defined as the probability of obtaining results that are as extreme as or more extreme than the observed results. A larger p-value indicates that the observed result is more consistent with the hypothesis, while a smaller p-value indicates the opposite. The p-value for the $q_\mu$ test statistic is:

$$p_\mu = \int_{q_{\text{obs}}}^{\infty} f(q_\mu \mid \mu)\, dq_\mu \tag{4.6}$$

Where f is the pdf of the test-statistic distribution.

### 4.12.4. CLs method

The p-values obtained from the likelihood ratio test can be used to set upper limits on the production of HH through the CLs method. This method aims to determine the maximum possible signal strength that can be excluded within a certain confidence interval. It involves comparing the ratios of p-values in the signal+background hypothesis to those in the background-only hypothesis. The 95% CLs test is used to set limits on the signal strength in searches where the signal is not yet observable, as in the HH searches. The 95%

CLs exclusion intervals are defined by:

$$\mathrm{CL}_s = \frac{p_{s+b}}{p_b} < 0.05 \tag{4.7}$$

The value $p_{s+b}$ represents the p-value of the signal plus background hypothesis, specifically for the occurrence of HH production at a signal strength of $\mu = 1$,

$$p_{s+b} = \int_{q_{\mathrm{obs}}}^{\infty} f(q_\mu \mid 1)\, dq_\mu \tag{4.8}$$

The value $p_b$ represents the p-value for the background only hypothesis, where here is no occurrence of HH production,

$$p_b = \int_{q_{\mathrm{obs}}}^{\infty} f(q_\mu \mid 0)\, dq_\mu \tag{4.9}$$

### 4.12.5. Significance

When the observed data significantly deviates from the background-only hypothesis, we can determine the level of significance of this result. The particle physics community uses benchmarks of $3\sigma$ and $5\sigma$ standard deviations to establish evidence or observation of a new process. The significance of a p-value, denoted as Z, is defined as:

$$Z = \phi^{-1}(1 - p) \tag{4.10}$$

Where $\phi$ is the standard normal distribution. For observation of a new particle Z=5(p-value $< 2.87 \times 10^{-7}$) and for evidence of a new particle Z=3(p-value $< 1.35 \times 10^{-3}$) while considering background only hypothesis.

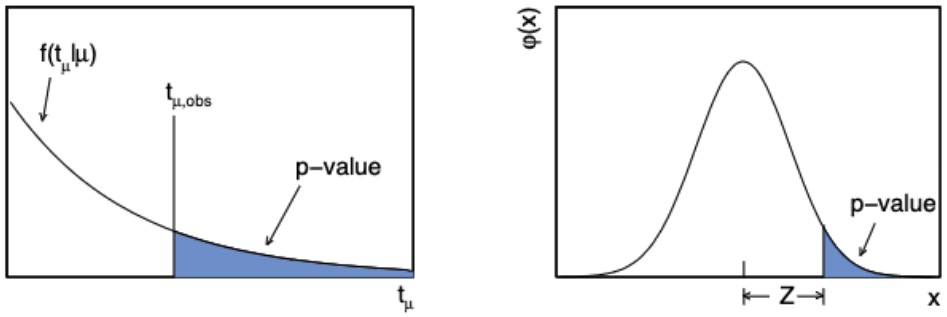


Figure 4.12: llustration of the relation between the $p$-value obtained from an observed value of the test statistic $t_\mu$ (left). The standard normal distribution $\phi(x) = \frac{1}{\sqrt{2\pi}} \exp(-\frac{x^2}{2})$ showing the relation between the significance Z and the p-value (right) [95].

## 4.13. Validation Region

The validation region refers to a subset of data used to validate the analysis procedure, assess the performance of the analysis, and ensure the reliability of the results. It serves as an independent dataset separate from control and signal regions and is used to evaluate how well the analysis methodology and selection criteria generalize to new, unseen data. In this analysis, the validation region is defined as the events are required to pass the extra selection of bdtg score $\leq$0.55 above the preselection described in section 4.4. This cut ensures that the validation region is orthogonal to signal region. Figure 4.13 shows the bdtg output variable in validation region.

The post fit plot of bdtg output and the variables used in the training of bdtg in the validation region are shown in the Figure 4.14 to 4.24. Both statistical and systematic uncertainties are included. The post-fit plots shows that the data and MC agrees within the given uncertainties in the validation region.

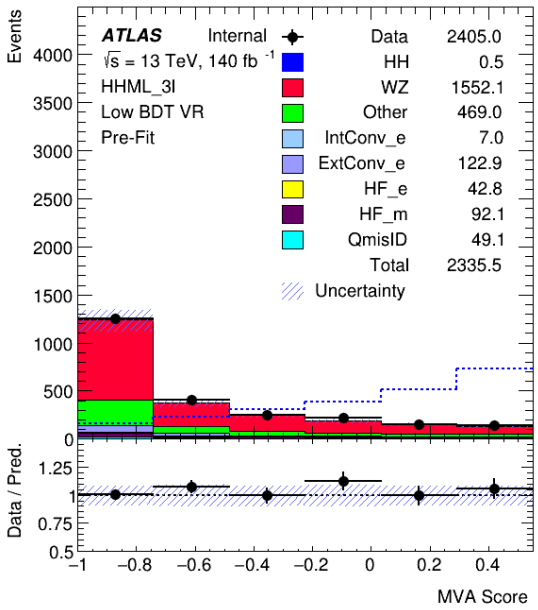


Figure 4.13: Pre-fit plot of bdtg output in validation region.

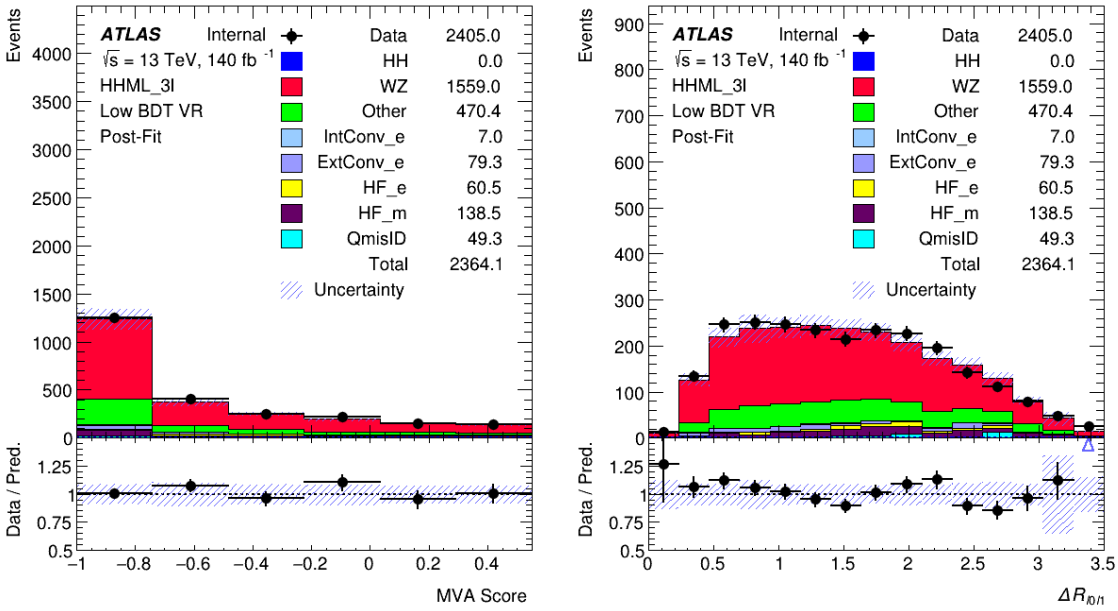


Figure 4.14: Pre-fit plot of bdtg output (left) and distance in $\eta - \phi$ space between lepton 0 and lepton 1 (right) in validation region.

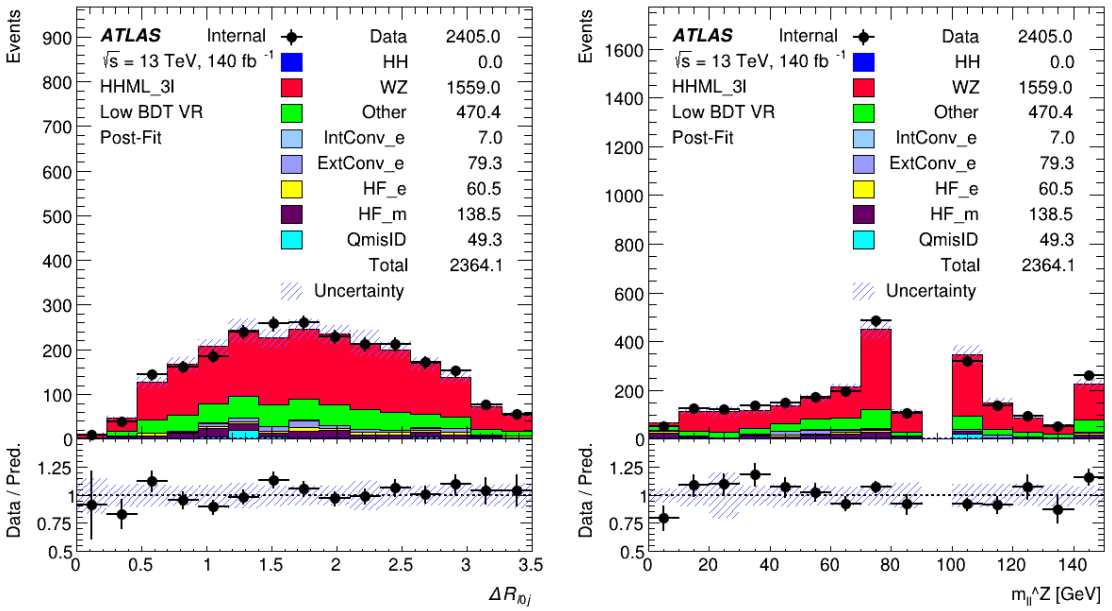


Figure 4.15: Post-fit plot of invariant mass of lepton 0 and nearest jet (left) and invariant mass of lepton pair closest to $Z$ mass (right) in validation region.

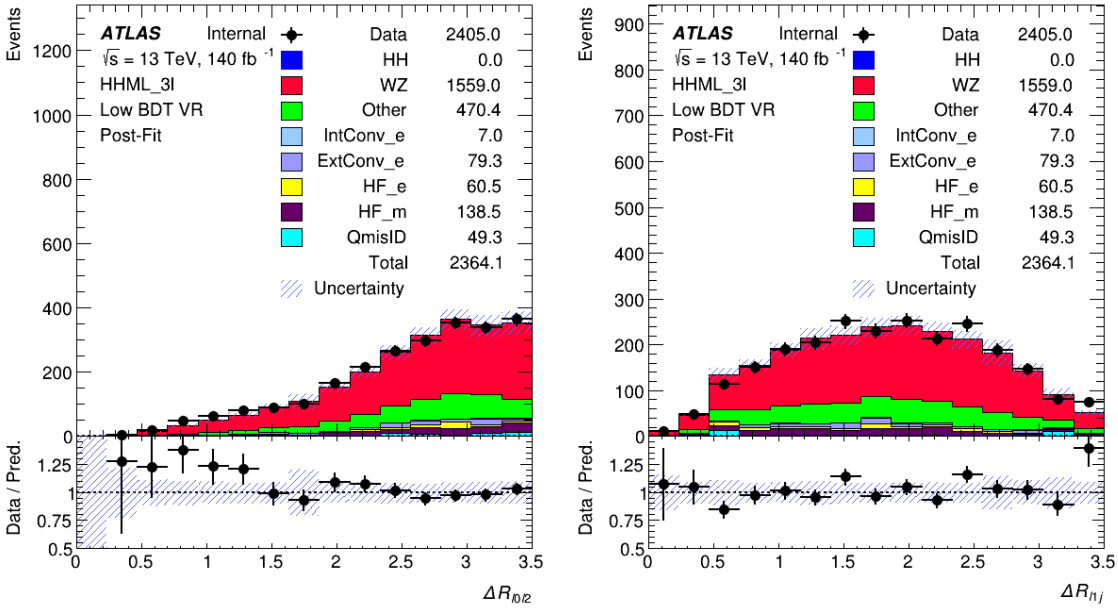


Figure 4.16: Post-fit plot of distance in $\eta - \phi$ space between lepton 0 and lepton 2 (left) and distance in $\eta - \phi$ space between lepton 1 and nearest jet (right) in validation region.

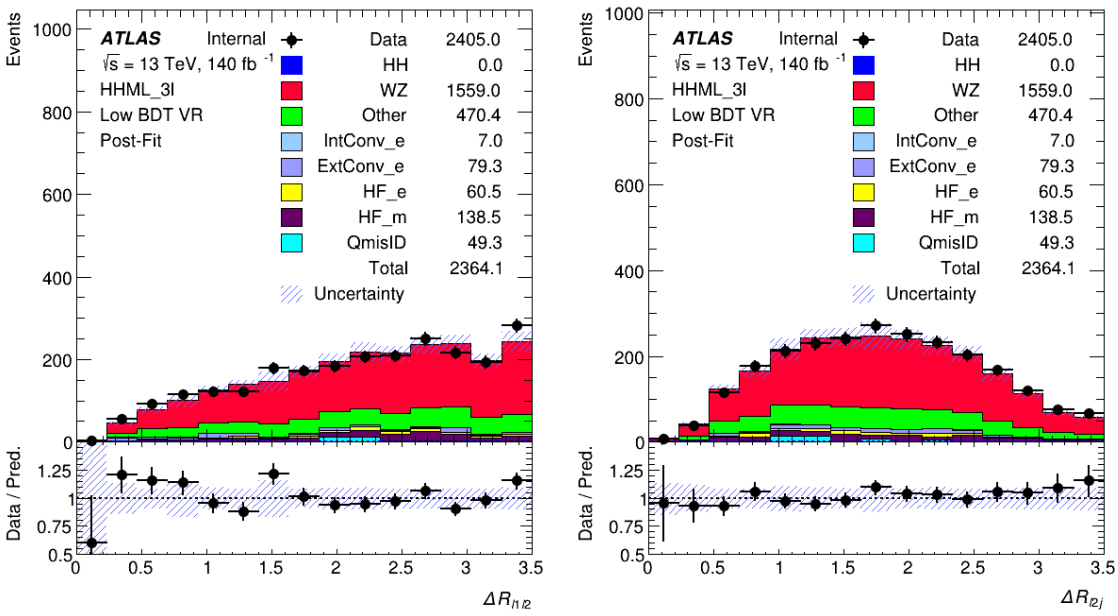


Figure 4.17: Post-fit plot of distance in $\eta - \phi$ space between lepton 1 and lepton 2 (left) and distance in $\eta - \phi$ space between lepton 2 and nearest jet (right) in validation region.

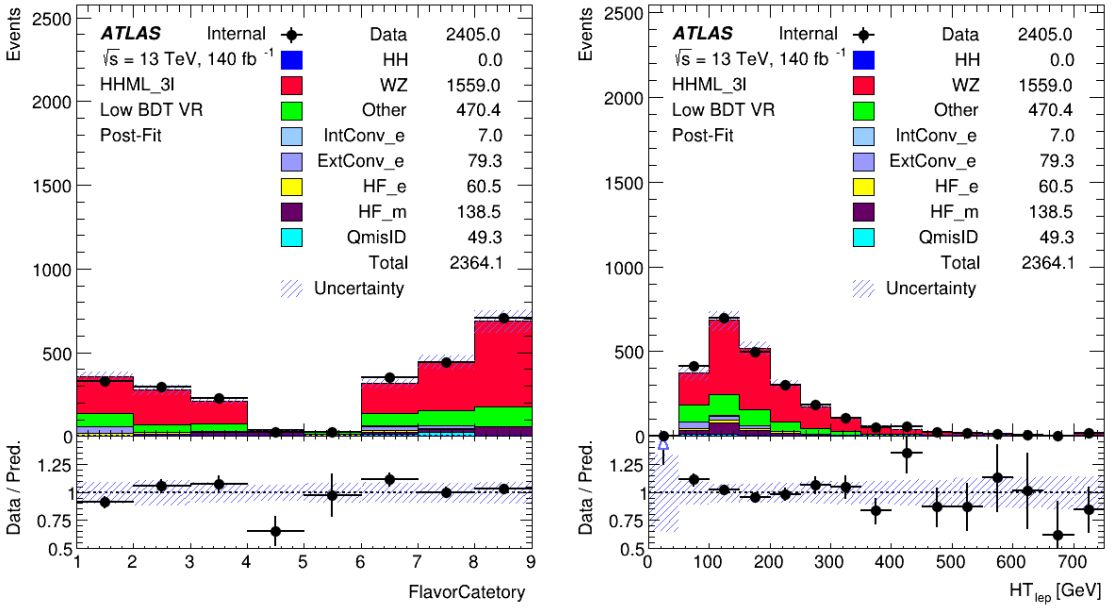


Figure 4.18: Post-fit plot of categorization of lepton flavors (left) and scalar sum of lepton $p_T$'s (right) in validation region.

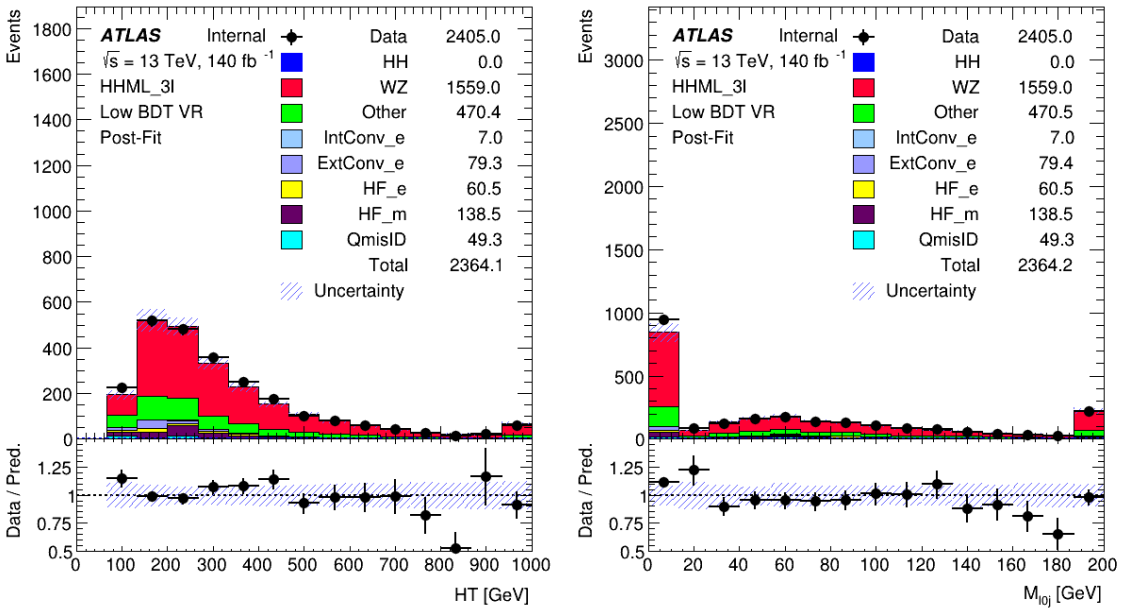


Figure 4.19: Post-fit plot of scalar sum of all particle's $p_T$'s (left) and invariant mass of lepton 0 and nearest jet (right) in validation region.

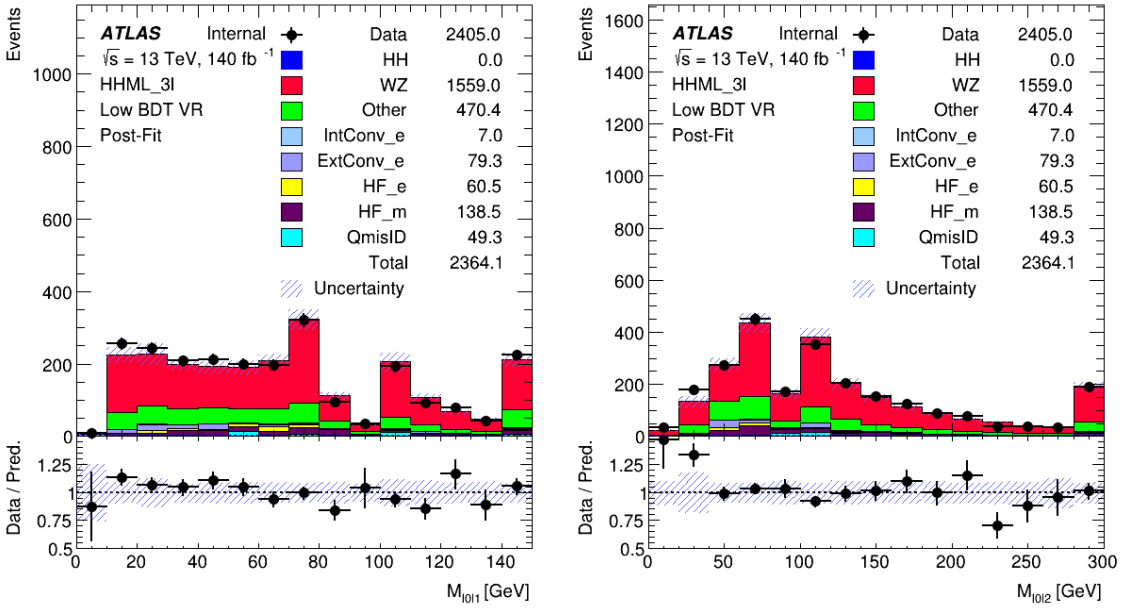


Figure 4.20: Post-fit plot of invariant mass of lepton 0 and lepton 1 (left) and invariant mass of lepton 0 and lepton 2 (right) in validation region.

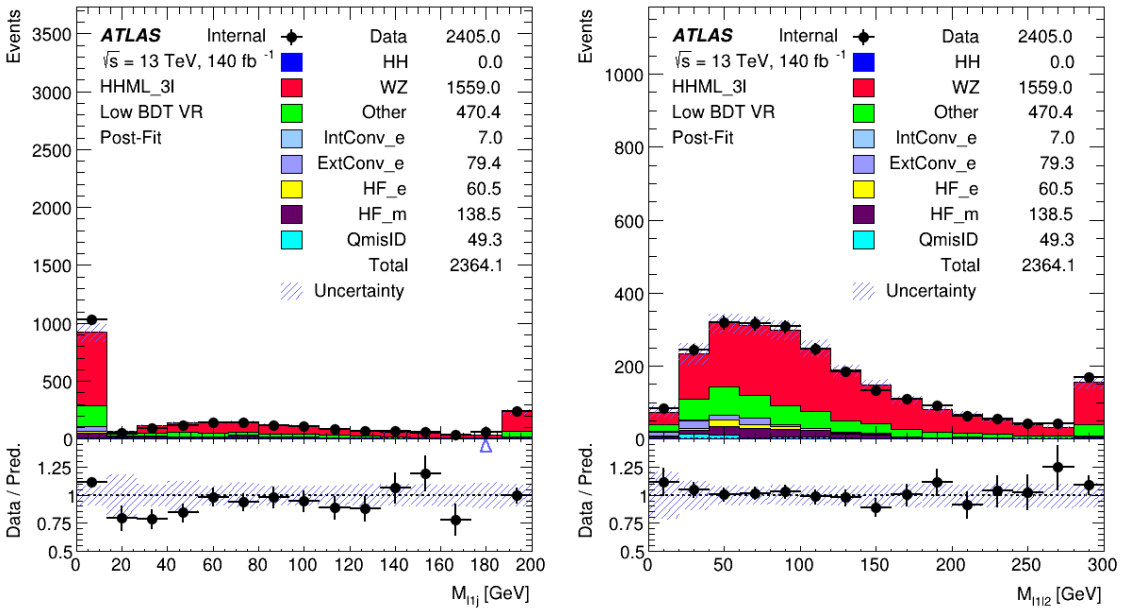


Figure 4.21: Post-fit plot of invariant mass of lepton 1 and nearest jet (left) and invariant mass of lepton 1 and lepton 2 (right) in validation region.

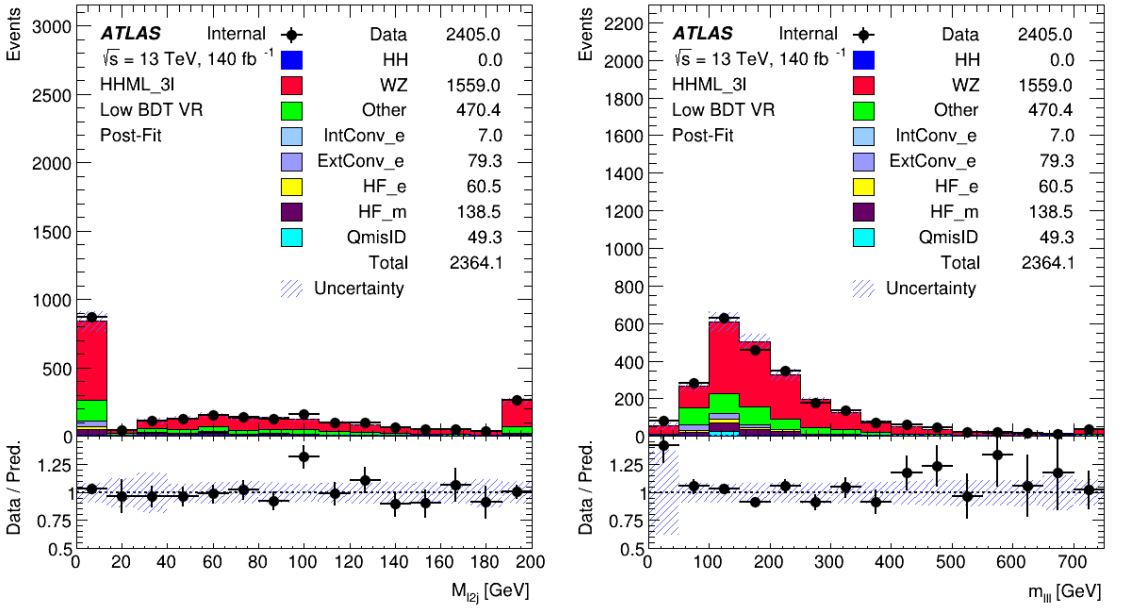


Figure 4.22: Post-fit plot of invariant mass of lepton 2 and nearest jet (left) and invariant mass of all three leptons (right) in validation region.

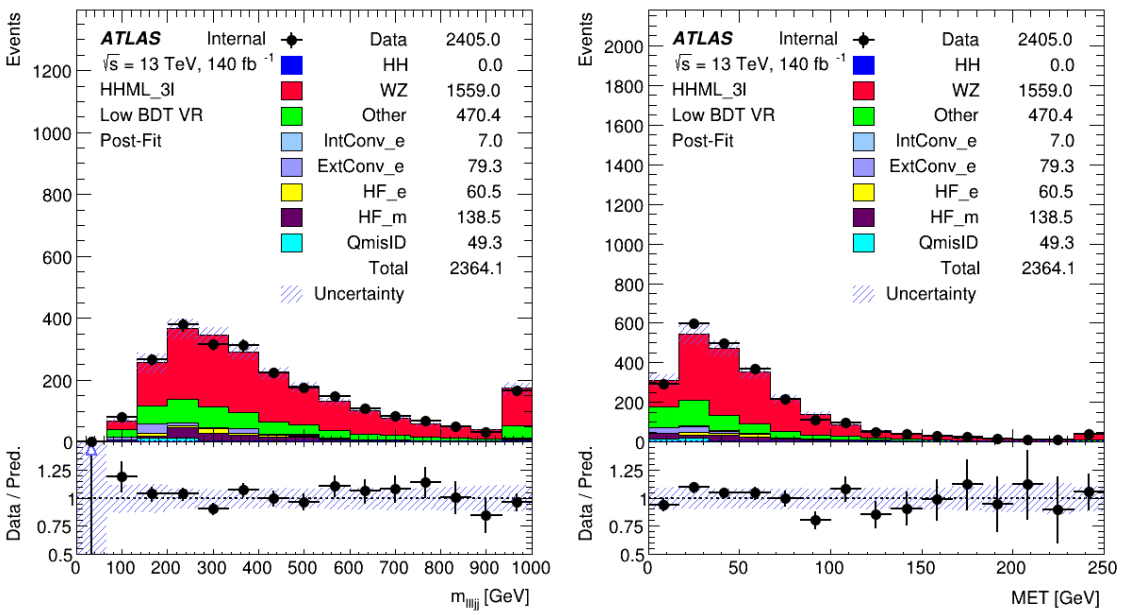


Figure 4.23: Post-fit plot of invariant mass of all three leptons and two leading jets (left) and missing transverse energy (right) in validation region.

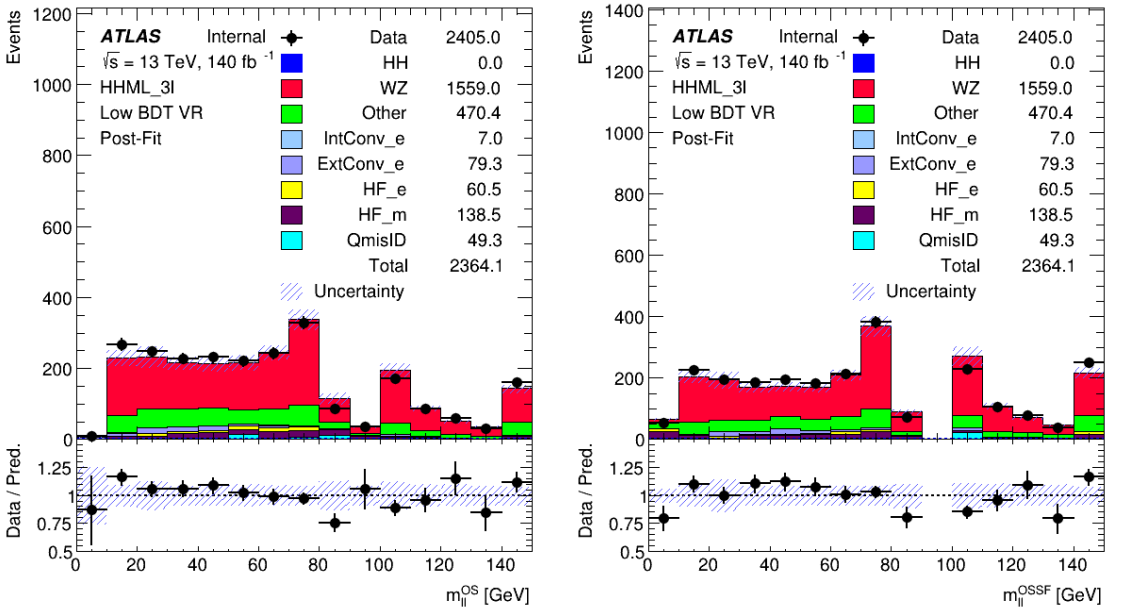


Figure 4.24: Post-fit plot of minimum invariant mass of opposite-sign lepton pairs( left) and minimum invariant mass of opposite-sign same-flavor lepton pairs (right) in validation region.

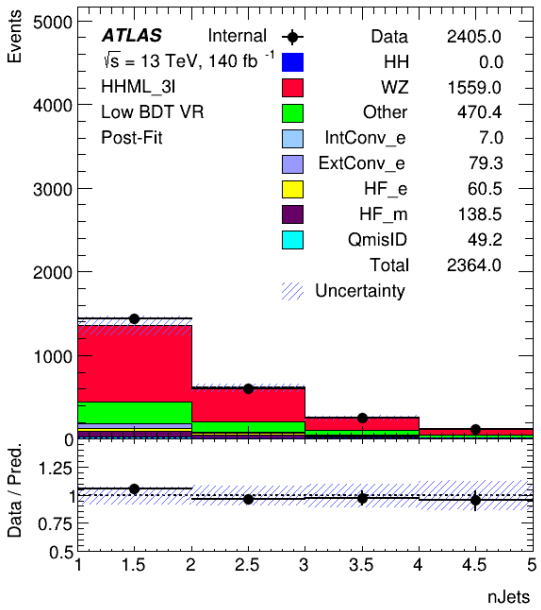


Figure 4.25: Post-fit plot of number of jets in the event in validation region.

## 4.14. Results

A fit is performed over signal region, using the dataset. The fit is based on the profile likelihood approach as described in section 4.12. The bdtg output distribution is used as a final discriminant in the fit. The unblinded post-fit bdtg plot is shown in 4.26. The binning of the BDT discriminant is optimized to reduce the statistical fluctuations. An automatic binning algorithm is employed, and bins are merged until a certain fraction of signal and background events is obtained. The merging is defined by the following function

$$Z = z_s \frac{n_s}{N_s} + z_b \frac{n_b}{N_b}, \tag{4.11}$$

where $n_s(n_b)$ is the number of signal (background) events in the merging bin, $N_s(N_b)$ is the total number of signal and background events. $z_s$ and $(z_b)$ are two free parameters to control the fraction of signal and background events in each bin. The merging of a bin stops if $Z > 1$.

The systematic uncertainties are treated as nuisance parameters (NP). The physics object related NPs follow the recommendation from each of the combined performance group as described in section 4.11. The NPs with small impact are neglected to improve the speed of the fit. A normalization or a shape uncertainty is not applied if the variation is below 1% in all bins. Figure 4.27 shows the pull of all the unpruned NPs. No large pulls are observed which suggests that there are not significant discrepancies between the fitted values of the NPs and their nominal values. The largest impact of the nuisance parameters on signal strength is assessed by performing the fit with the parameter fixed to its fitted value varied up or down by its fitted uncertainty whereas all the other parameters are allowed to vary. Figure 4.28 shows the nuisance parameters ranked in the decreasing order of their impact on the signal strength. The statistical bin of the BDT is identified as the dominant nuisance parameter. This means that the uncertainty associated with the event counts in the BDT bins, arising from statistical fluctuations, has the most significant impact on the determination of the signal strength.

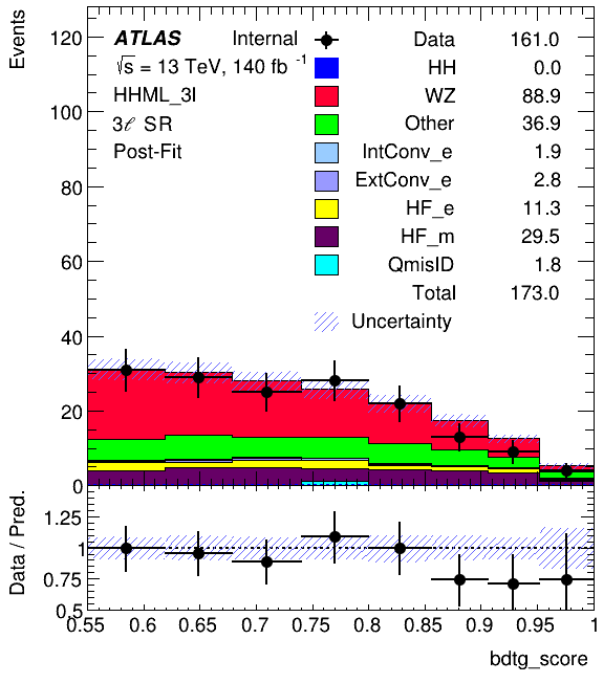


Figure 4.26: The post-fit bdtg distribution for bdtg $> 0.55$ in signal region.

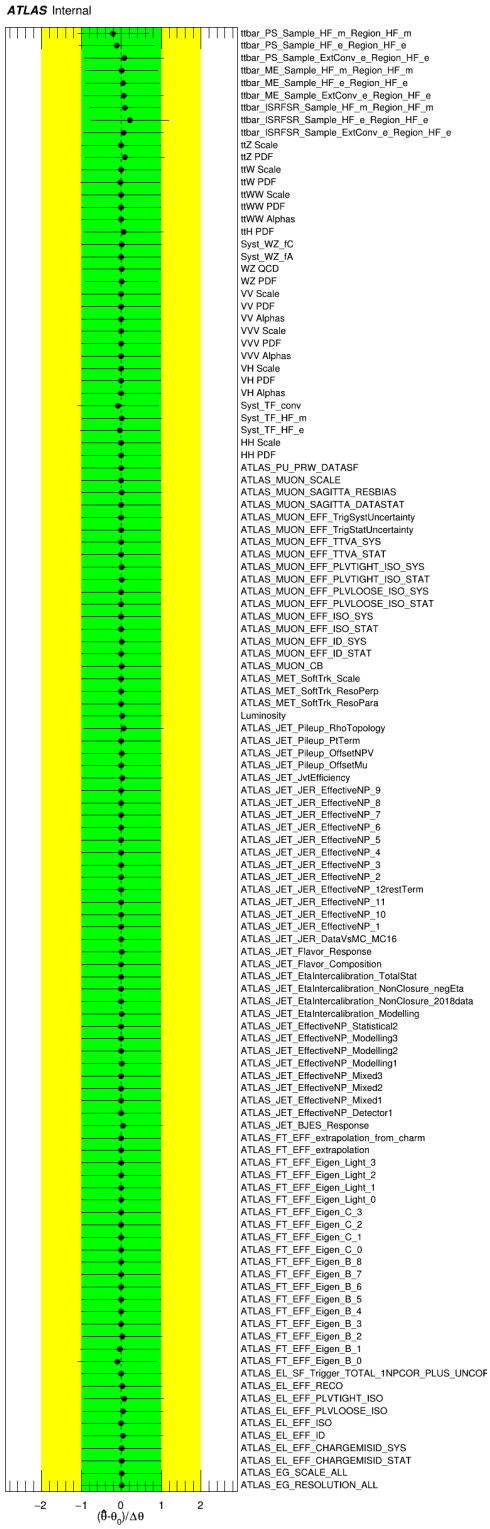


Figure 4.27: Pulls and constraints of nuisance parameters.

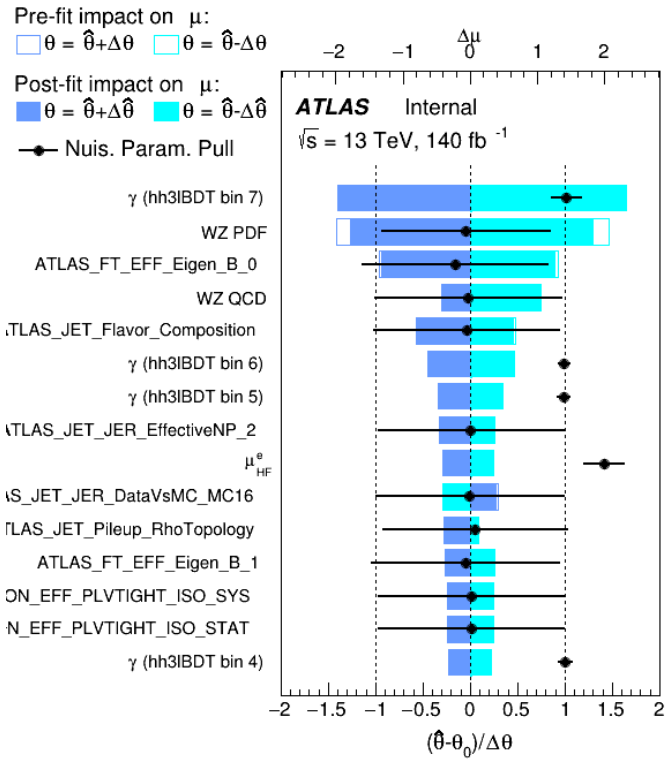


Figure 4.28: Impact of nuisance parameters on the signal strength in the signal region.

Using the CLs method, an observed (expected) upper limit at 95% CL on the signal strength of 20 (28) times the SM prediction is obtained as shown in Table 4.7. The expected limit is computed based on 'background-only hypothesis' where the parameter of interest is fixed to zero, which means no signal is injected. The observed limit of 20 times the SM prediction suggests that the data analyzed in the $3l0\tau_h$ channel is consistent with a signal strength up to 20 times the expected SM value. This means that any potential signal contribution should not exceed this value to be compatible with the observed data. The expected limits, ranging from 15.22 to 57.12 times the SM prediction, represent the upper bounds on the signal strength that would be expected if there is no actual signal present. The range of expected limits at different levels of significance gives an estimate of the sensitivity of the analysis to deviations from the background-only hypothesis.

| | $-2\sigma$ | $-1\sigma$ | Median | $+1\sigma$ | $+2\sigma$ |
|---|---|---|---|---|---|
| Expected | 15.22 | 20.43 | 28.36 | 40.69 | 57.12 |
| Observed | | | 20.01 | | |

Table 4.7: Expected and Observed 95% CL exclusion limit on the signal strength of $3l0\tau_h$ channel.

# Chapter 5

## Conclusion

In this thesis, a search is presented for Higgs boson pair production in three light leptons ($e/\mu$) final states. The analysis is performed using an integrated luminosity of 140 $fb^{-1}$ of $pp$ collision at $\sqrt{s} = 13\ TeV$ collected by ATLAS detector at the LHC. No significant excess above the Standard Model background expectation was observed. The search set limits on the HH signal strength, with an upper observed (expected) limit of 20 (28) time the SM cross section at 95% CL. The significance and impact of this result are further highlighted by the Figure 5.1, which shows the combined upper limits in the HH Multilepton Analysis. This figure demonstrates that the $3l0\tau_h$ channel is one of the most robust channels within the HH Multilepton analysis.

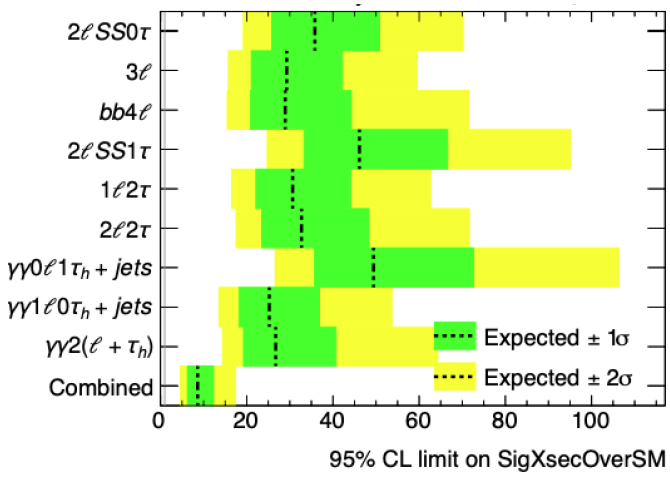


Figure 5.1: Combined upper limits in HH Multilepton Analysis.

The importance of this result lies in its contribution to the broader search for non-resonant HH production at ATLAS. By combining the results from various channels, including the

$3l0\tau_h$ channel, the sensitivity to the Higgs self-coupling and the search for HH production can be enhanced. This is particularly important as these analyses play a critical role during Run 3 and the High-Luminosity LHC phase.

Moreover, the implications of this research extend beyond the immediate scope of this analysis. The exploration of an uncharted channel sheds light on a novel avenue for investigation. By delving into the complexities of final states involving three light leptons ($e/\mu$), this study unlocks unprecedented levels of sensitivity. The tools developed through this study will prove invaluable as we strive to achieve the long-awaited milestone of attaining the cross section predicted by the Standard Model.

# BIBLIOGRAPHY


[1] H. B. Hartley, *John dalton, frs (1766-1844) and the atomic theory—a lecture to commemorate his bicentenary*, *Proceedings of the Royal Society of London. Series B. Biological Sciences* **168** (1967) 335–359. 1

[2] G. Zweig, *An su(3) model for strong interaction symmetry and its breaking*, tech. rep., CM-P00042884, 1964. 1

[3] P. Bagnaia, M. Banner, R. Battiston, P. Bloch, F. Bonaudi, K. Borer et al., *Evidence for z0→ e+ e- at the cern pp collider*, *Physics Letters B* **129** (1983) 130–140. 2

[4] F. Abe, H. Akimoto, A. Akopian, M. Albrow, S. Amendolia, D. Amidei et al., *Observation of top quark production in p p collisions with the collider detector at fermilab*, *Physical review letters* **74** (1995) 2626. 2

[5] ATLAS collaboration, *Observation of a new particle in the search for the standard model higgs boson with the atlas detector at the lhc*, *arXiv preprint arXiv:1207.7214* (2012) . 2, 4

[6] S. Chatrchyan, V. Khachatryan, A. M. Sirunyan, A. Tumasyan, W. Adam, E. Aguilo et al., *Observation of a new boson at a mass of 125 gev with the cms experiment at the lhc*, *Physics Letters B* **716** (2012) 30–61. 4

[7] C.-N. Yang and R. L. Mills, *Conservation of isotopic spin and isotopic gauge invariance*, *Physical review* **96** (1954) 191. 4

[8] E. Noether, *Invariant variation problems*, *Transport theory and statistical physics* **1** (1971) 186–207. 4

[9] F. Englert and R. Brout, *Broken symmetry and the mass of gauge vector mesons*, *Physical review letters* **13** (1964) 321. 5

[10] D. de Florian, D. Fontes, J. Quevillon, M. Schumacher, F. Llanes-Estrada, A. Gritsan et al., *arXiv: Handbook of LHC Higgs Cross Sections: 4. Deciphering the Nature of the Higgs Sector*. No. arXiv: 1610.07922. Cern, 2016. 9

[11] P. D. Group, P. Zyla, R. Barnett, J. Beringer, O. Dahl, D. Dwyer et al., *Review of particle physics*, *Progress of Theoretical and Experimental Physics* **2020** (2020) 083C01. xi, 10

[12] F. Maltoni, D. Pagani, A. Shivaji and X. Zhao, *Trilinear higgs coupling determination via single-higgs differential measurements at the lhc*, *The European Physical Journal C* **77** (2017) 1–24. 11

[13] ATLAS collaboration, *Constraint of the higgs boson self-coupling from higgs boson differential production and decay measurements*, tech. rep., ATL-PHYS-PUB-2019-009, 2019. xi, 11, 12, 13

[14] R. Frederix, S. Frixione, V. Hirschi, F. Maltoni, O. Mattelaer, P. Torrielli et al., *Higgs pair production at the lhc with nlo and parton-shower effects*, *Physics Letters B* **732** (2014) 142–149. xi, 12, 13

[15] D. de Florian and J. Mazzitelli, *Higgs pair production at next-to-next-to-leading logarithmic accuracy at the lhc*, *Journal of High Energy Physics* **2015** (2015) 1–14. 13, 14

[16] S. Dawson, S. Dittmaier and M. Spira, *Neutral higgs-boson pair production at hadron colliders: Qcd corrections*, *Physical Review D* **58** (1998) 115012. 14

[17] J. Alison et al., *Higgs boson pair production at colliders: status and perspectives*, *Double Higgs Production at Colliders Batavia, IL, USA, September* **4** (2019) 2018–9. xi, 15

[18] ATLAS collaboration, *Search for non-resonant pair production of higgs bosons in the bbbb final state in pp collisions at√ s= 13 tev with the atlas detector*, ATLAS-CONF-2022-035, 2022. 15

[19] ATLAS collaboration, M. Aaboud et al., *Search for resonant and non-resonant Higgs boson pair production in the $b\bar{b}\tau^+\tau^-$ decay channel in pp collisions at $\sqrt{s} = 13$ TeV with the ATLAS detector*, *Phys. Rev. Lett.* **121** (2018) 191801, [1808.00336]. 15

[20] G. Aad, B. Abbott, D. C. Abbott, A. A. Abud, K. Abeling, D. K. Abhayasinghe et al., *Search for higgs boson pair production in the two bottom quarks plus two photons final state in p p collisions at s= 13 tev with the atlas detector*, *Physical Review D* **106** (2022) 052001. 15

[21] S. Sultansoy, A. Collaboration et al., *Search for higgs boson pair production in the $ww\gamma\gamma$ channel using pp collision data recorded at sqrt (s)= 13 tev with the atlas detector*, *European Physical Journal C* (2018) . 15

[22] CMS collaboration, *Search for resonant and nonresonant higgs boson pair production in the bblnulnu final state in proton-proton collisions at sqrt (s)= 13 tev*, *arXiv preprint arXiv:1708.04188* (2017) . 15

[23] M. Aaboud, G. Aad, B. Abbott, B. Abeloos, D. Abhayasinghe, S. Abidi et al., *Search for higgs boson pair production in the wwww decay channel using atlas data recorded at sqrt (s)= 13 tev*, *Journal of High Energy Physics* **2019** (2019) 1–38. 15

[24] ATLAS collaboration, G. Aad et al., *Constraints on the Higgs boson self-coupling from single- and double-Higgs production with the ATLAS detector using pp collisions at s=13 TeV*, *Phys. Lett. B* **843** (2023) 137745, [2211.01216]. xi, 15, 16

[25] L. Evans and P. Bryant, *Lhc machine*, *Journal of instrumentation* **3** (2008) S08001. 17

[26] C. Lefèvre, *The cern accelerator complex. complexe des accélérateurs du cern*, *CERN, Geneva* (2008) . xi, 17, 18

[27] R. Scrivens, D. Küchler, M. O'Neil, M. Kronberger, C. Schmitzer, J. Lettry et al., *Overview of the status and developments on primary ion sources at cern*, *CERN-ATS-2011-172* (2011) . 17

[28] TL, A. A. Alves, L. A. Filho, A. Barbosa, I. Bediaga, G. Cernicchiaro et al., *The lhcb detector at the lhc*, *Journal of instrumentation* **3** (2008) S08005–S08005. 17

[29] S. Chatrchyan, G. Hmayakyan, V. Khachatryan, A. Sirunyan, W. Adam, T. Bauer et al., *The cms experiment at the cern lhc*, *Jinst* **3** (2008) S08004. 18

[30] G. Aad, J. Butterworth, J. Thion, U. Bratzler, P. Ratoff, R. Nickerson et al., *The atlas experiment at the cern large hadron collider*, *Jinst* **3** (2008) S08003. xii, 18, 25

[31] J. Pequenao, *Computer generated image of the whole atlas detector*, tech. rep., 2008. https://cds.cern.ch/record/1095924. xii, 19

[32] A. Yamamoto, Y. Makida, R. Ruber, Y. Doi, T. Haruyama, F. Haug et al., *The atlas central solenoid*, *Nuclear Instruments and Methods in Physics Research Section A: Accelerators, Spectrometers, Detectors and Associated Equipment* **584** (2008) 53–74. xii, 21, 22

[33] J. Badiou, J. Baze and J. Beltramelli, *Atlas barrel toroid: Technical design report*, tech. rep., ATLAS-TDR-007, 1997. 22

[34] ATLAS collaboration, *Atlas inner detector technical design report*, *Technical Design Report ATLAS. CERN, Geneva* **216** (1997) . xii, 22, 24

[35] M. Capeans, G. Darbo, K. Einsweiller, M. Elsing, T. Flick, M. Garcia-Sciveres et al., *Atlas insertable b-layer technical design report tech. rep*, tech. rep., CERN-LHCC-2010-013. ATLAS-TDR-19, 2010. 23

[36] K. Kleinknecht, *Detectors for particle radiation*. Cambridge University Press, 1998. 25

[37] ATLAS collaboration, *ATLAS liquid-argon calorimeter: Technical Design Report*. Technical design report. ATLAS. CERN, Geneva, 1996, 10.17181/CERN.FWRW.FOOQ. xii, 26

[38] ATLAS collaboration, *ATLAS tile calorimeter: Technical Design Report*. Technical design report. ATLAS. CERN, Geneva, 1996, 10.17181/CERN.JRBJ.7O28. xii, 27

[39] ATLAS collaboration, *ATLAS muon spectrometer: Technical Design Report*. Technical design report. ATLAS. CERN, Geneva, 1997. xii, 28, 29

[40] M. Nessi, M. Nordberg, P. Jenni and K. Smith, *Atlas high-level trigger, data-acquisition and controls: Technical design report*, tech. rep., ATLAS-TDR-016, 2003. 29

[41] ATLAS collaboration, *Operation of the atlas trigger system in run 2*, *Journal of Instrumentation 15, P10004* (2020) . xii, 30

[42] J. Alwall, R. Frederix, S. Frixione, V. Hirschi, F. Maltoni, O. Mattelaer et al., *The automated computation of tree-level and next-to-leading order differential cross sections, and their matching to parton shower simulations*, *JHEP* **07** (2014) 079, [1405.0301]. 32, 41, 42, 44

[43] E. Bothmann, G. S. Chahal, S. Höche, J. Krause, F. Krauss, S. Kuttimalai et al., *Event generation with sherpa 2.2*, *SciPost Physics* **7** (sep, 2019) . 32

[44] S. Alioli, P. Nason, C. Oleari and E. Re, *A general framework for implementing NLO calculations in shower monte carlo programs: the POWHEG BOX*, *Journal of High Energy Physics* **2010** (jun, 2010) . 32, 40

[45] T. Sjöstrand, S. Ask, J. R. Christiansen, R. Corke, N. Desai, P. Ilten et al., *An introduction to PYTHIA 8.2*, *Computer Physics Communications* **191** (jun, 2015) 159–177. 32

[46] M. Bahr et al., *Herwig++ Physics and Manual*, *Eur. Phys. J. C* **58** (2008) 639–707, [0803.0883]. 32, 44

[47] S. Agostinelli et al., *Geant4–a simulation toolkit*, *Nucl. Instrum. Meth. A* **506** (2003) 0. 32

[48] T. Cornelissen, M. Elsing, S. Fleischmann, W. Liebig, E. Moyse and A. Salzburger, *Concepts, Design and Implementation of the ATLAS New Tracking (NEWT)*, tech. rep., CERN, Geneva, 2007. xii, 34

[49] M. Aaboud, G. Aad, B. Abbott, J. Abdallah, O. Abdinov, B. Abeloos et al., *Performance of the atlas track reconstruction algorithms in dense environments in lhc run 2*, *The European Physical Journal C* **77** (2017) 1–30. 34

[50] M. Aaboud, G. Aad, B. Abbott, J. Abdallah, O. Abdinov, B. Abeloos et al., *Jet reconstruction and performance using particle flow with the atlas detector*, *The European Physical Journal C* **77** (2017) 1–47. 35, 37

[51] ATLAS collaboration, *Electron efficiency measurements with the ATLAS detector using the 2015 LHC proton-proton collision data, ATLAS-CONF-2016-024*, . 35

[52] G. Aad, B. Abbott, D. C. Abbott, A. A. Abud, K. Abeling, D. K. Abhayasinghe et al., *Muon reconstruction and identification efficiency in atlas using the full run 2 pp collision data set at s= 13 tev*, *The European Physical Journal C* **81** (2021) 578. 36

[53] M. Cacciari, G. P. Salam and G. Soyez, *The anti-kt jet clustering algorithm*, *Journal of High Energy Physics* **2008** (2008) 063. 37

[54] ATLAS collaboration, *Jet energy scale and resolution measured in proton–proton collisions at s= 13 tev with the atlas detector*, *The European Physical Journal C* **81** (2021) 689. 37, 69

[55] S. Parajuli, *Impact Parameter resolutions in di-jet events*, tech. rep., CERN, Geneva, 2018. xii, 37, 38

[56] M. Cacciari, G. P. Salam and G. Soyez, *The catchment area of jets*, *Journal of High Energy Physics* **2008** (apr, 2008) 005. 38

[57] ATLAS collaboration, *Calibration of light-flavour b-jet mistagging rates using ATLAS proton-proton collision data at* $\sqrt{s} = 13$ *TeV*, tech. rep., CERN, Geneva, 2018. 38

[58] ATLAS collaboration, "ATLAS Pythia 8 tunes to 7 TeV data." ATL-PHYS-PUB-2014-021, 2014. 41

[59] NNPDF collaboration, R. D. Ball et al., *Parton distributions for the LHC Run II*, *JHEP* **04** (2015) 040, [1410.8849]. 41, 43

[60] ATLAS collaboration, "The simulation principle and performance of the ATLAS fast calorimeter simulation FastCaloSim." ATL-PHYS-PUB-2010-013, 2010. 41

[61] T. Sjöstrand, S. Mrenna and P. Z. Skands, *A brief introduction to PYTHIA 8.1*, *Comput. Phys. Commun.* **178** (2008) 852–867, [0710.3820]. 42

[62] ATLAS collaboration, "The Pythia 8 A3 tune description of ATLAS minimum bias and inelastic measurements incorporating the Donnachie–Landshoff diffractive model." ATL-PHYS-PUB-2016-017, 2016. 42

[63] ATLAS collaboration, *The ATLAS Simulation Infrastructure*, *Eur. Phys. J. C* **70** (2010) 823, [1005.4568]. 42

[64] S. Agostinelli et al., *GEANT4 – a simulation toolkit*, *Nucl. Instrum. Meth. A* **506** (2003) 250. 42

[65] S. Frixione, G. Ridolfi and P. Nason, *A positive-weight next-to-leading-order monte carlo for heavy flavour hadroproduction*, *JHEP* **09** (2007) 126, [0707.3088]. 43

[66] E. Re, *Single-top wt-channel production matched with parton showers using the powheg method*, *Eur. Phys. J. C* **71** (2011) 1547, [1009.2450]. 43

[67] T. Sjöstrand et al., *High-energy-physics event generation with pythia 6.1*, *Comput. Phys. Commun.* **135** (2001) 238, [hep-ph/0010017]. 44

[68] T. Sjöstrand, S. Mrenna and P. Skands, *A brief introduction to pythia 8.1*, *Comput. Phys. Commun.* **178** (2008) 852, [0710.3820]. 44

[69] J. Bellm et al., *Herwig 7.0/Herwig++ 3.0 release note*, *Eur. Phys. J. C* **76** (2016) 196, [1512.01178]. 44

[70] F. Cascioli, P. Maierhofer and S. Pozzorini, *Scattering Amplitudes with Open Loops*, *Phys. Rev. Lett.* **108** (2012) 111601, [1111.5206]. 44

[71] T. Gleisberg and S. Höche, *Comix, a new matrix element generator*, *JHEP* **12** (2008) 039, [0808.3674]. 44

[72] S. Schumann and F. Krauss, *A parton shower algorithm based on Catani–Seymour dipole factorisation*, *JHEP* **03** (2008) 038, [0709.1027]. 44

[73] S. Höche, F. Krauss, M. Schönherr and F. Siegert, *QCD matrix elements + parton showers: The NLO case*, *JHEP* **04** (2013) 027, [1207.5030]. 44

[74] D. J. Lange, *The EvtGen particle decay simulation package*, *Nucl. Instrum. Meth. A* **462** (2001) 152. 44

[75] P. Golonka and Z. Was, *PHOTOS Monte Carlo: A Precision tool for QED corrections in Z and W decays*, *Eur. Phys. J.* **C45** (2006) 97–107, [hep-ph/0506026]. 45

[76] ATLAS collaboration, "Vertex Reconstruction Performance of the ATLAS Detector at $\sqrt{s} = 13$ TeV." ATL-PHYS-PUB-2015-026, 2015. 45

[77] T. Vazquez Schroeder, R. Polifka, X. Poveda Torres, M. N. Agaras, B. Ali, S. Angelidakis et al., *Search for the Associated Production of a Higgs Boson and a Top Quark Pair in multilepton final states in 80 fb$^{-1}$ pp Collisions at $\sqrt{s}$ = 13 TeV with the ATLAS Detector*, tech. rep., CERN, Geneva, 2018. 45, 48

[78] "TriggerEfficiency." https://twiki.cern.ch/twiki/bin/view/Atlas/TrigGlobalEfficiencyCorrectionTool. 45, 52, 55

[79] R. Ospanov, R. T. Roberts and T. R. Wyatt, *Tagging non-prompt electrons and muons*, tech. rep., CERN, Geneva, Oct, 2016. 48

[80] ATLAS collaboration, *Jet reconstruction and performance using particle flow with the ATLAS Detector*, *Eur. Phys. J. C* **77** (2017) 466, [1703.10485]. 49

[81] ATLAS collaboration, *Atlas flavor-tagging calibration results with 139 ifb*, 06, 2019. http://atlas.web.cern.ch/Atlas/GROUPS/PHYSICS/PLOTS/FTAG-2019-004/. 50

[82] ATLAS collaboration, *Expected performance of the 2019 atlas b-taggers*, 09, 2019. http://atlas.web.cern.ch/Atlas/GROUPS/PHYSICS/PLOTS/FTAG-2019-005/. 50

[83] I. Nomidis, *Event selection, performance and background estimation in the $H \to \gamma\gamma$ channel with Run-2 data*, Tech. Rep. ATL-COM-PHYS-2020-378, CERN, Geneva, May, 2020. 51

[84] M. N. Agaras, *Search for vector-like leptons coupling to first and second generation Standard Model leptons in multilepton final states*, tech. rep., CERN, Geneva, 2022. 57

[85] R. Brun and F. Rademakers, *ROOT: An object oriented data analysis framework*, *Nucl. Instrum. Meth. A* **389** (1997) 81–86. 63

[86] J. Ye, J.-H. Chow, J. Chen and Z. Zheng, *Stochastic gradient boosted distributed decision trees*, in *Proceedings of the 18th ACM conference on Information and knowledge management*, pp. 2061–2064, 2009. 63

[87] J. D. Rodriguez, A. Perez and J. A. Lozano, *Sensitivity analysis of k-fold cross validation in prediction error estimation*, *IEEE transactions on pattern analysis and machine intelligence* **32** (2009) 569–575. 65

[88] ATLAS collaboration, "Luminosity determination in $pp$ collisions at $\sqrt{s} = 13$ TeV using the ATLAS detector at the LHC." ATLAS-CONF-2019-021, 2019. 68

[89] "trigger recommendations." https://twiki.cern.ch/twiki/bin/view/Atlas/TriggerRecommendationsForAnalysisGroupsFullRun2. 68

[90] ATLAS collaboration, *Jet energy scale measurements and their systematic uncertainties in proton–proton collisions at $\sqrt{s} = 13$ TeV with the ATLAS detector*, *Phys. Rev. D* **96** (2017) 072002, [1703.09665]. 69

[91] M. Grazzini, G. Heinrich, S. Jones, S. Kallweit, M. Kerner, J. M. Lindert et al., *Higgs boson pair production at NNLO with top quark mass effects*, *Journal of High Energy Physics* **2018** (may, 2018) . 69

[92] "LHCHXSWGHH." https://twiki.cern.ch/twiki/bin/view/LHCPhysics/LHCHWGHH?redirectedfrom=LHCPhysics.LHCHXSWGHH. 69, 71

[93] "ttH cross section." https://twiki.cern.ch/twiki/bin/view/LHCPhysics/CERNYellowReportPageAt13TeV. 70

[94] "CrossSectionYR4." https://twiki.cern.ch/twiki/bin/view/LHCPhysics/CrossSectionYR4. 70

[95] G. Cowan, K. Cranmer, E. Gross and O. Vitells, *Asymptotic formulae for likelihood-based tests of new physics*, *The European Physical Journal C* **71** (2011) 1–19. xiii, 77

[96] G. D. Kribs, A. Maier, H. Rzehak, M. Spannowsky and P. Waite, *Electroweak oblique parameters as a probe of the trilinear higgs boson self-interaction*, *Physical Review D* **95** (2017) 093004.

[97] W. P. Vazquez, A. Collaboration et al., *The atlas data acquisition system in lhc run 2*, in *Journal of Physics: Conference Series*, vol. 898, p. 032017, IOP Publishing, 2017.

[98] F. A. Dreyer and A. Karlberg, *Vector-boson fusion higgs pair production at* $n^3LO$, *Phys. Rev. D* **98** (Dec, 2018) 114016.